EXPERIMENTAL DETERMINATION OF THE THERMOELECTRIC PROPERTIES OF POROUS SILICON NANOWIRES

BY

HONGXIANG TIAN

DISSERTATION

Submitted in partial fulfillment of the requirements
for the degree of Doctor of Philosophy in Mechanical Engineering
in the Graduate College of the
University of Illinois at Urbana-Champaign, 2014

Urbana, Illinois

Doctoral Committee:

Professor Sanjiv Sinha, Chair
Professor Xiuling Li
Professor Elif Ertekin
Professor Kimani Toussaint

ABSTRACT

The thermoelectric properties of nanostructured silicon have attracted significant attention in recent work. The objective is to reduce thermal conductivity through the introduction of phonon scattering mechanisms while preserving charge transport. Initial reports on electrolessly etched silicon nanowires and periodic "holey" silicon membranes contained several puzzling aspects that remain unresolved. Here, we present measurements on mesoporous silicon nanowires fabricated through electroless etching of degenerately doped silicon. While thermal conductivity in this material at room temperature is attractive for thermoelectric applications at $\sim$2 W/(m·K), charge transport is severely degraded due to the disordered yet nanocrystalline structure. We investigate post doping conditions to improve the electrical conductivity by $\sim$3 orders of magnitude. TEM characterization confirmed that porosity and crystalline structure are retained after doping. We characterized the boron concentration before and after doping by secondary ion mass spectroscopy (SIMS). Raman spectroscopy was also employed to extract the free carrier concentrations as well as nanocrystalline size. We measured the Seebeck coefficient and thermal conductivity from 30 K to 400 K by a frequency domain technique. Analysis of Seebeck coefficient reveals the electron scattering mechanism in porous silicon nanowire before and after post-doping. The carrier concentrations extracted from Seebeck coefficient are in good agreement with the Raman spectrum analysis. In order to interpret the thermal conductivity data, we propose a frequency dependent multiple scattering of phonons across the porous wire. This work provides detailed insight into charge and heat transport in disordered yet nanocrystalline materials and advances their engineering for thermoelectric waste heat harvesting amongst other applications.

To my parents and sister, for their love and support.
In memory of my grandfather.

ACKNOWLEDGMENTS

First I would like to thank my advisor Professor Sanjiv Sinha for his support and guidance during my whole graduate study. His wisdom and insight helped me overcome all the obstacles I confronted in my research. I appreciate his patience and encouragement when I got stuck in numerous failures during the sample fabrication. I have benefited a lot from his advice that always think critically and think steps further. I would also like to thank my PhD dissertation committee members: Professor Elif Ertekin, Professor Xiuling Li and Professor Kimani Toussaint for their valuable suggestion and interest in my work.

I was happy to work with many intelligent individuals in my group; my thesis work could not be completed without them. Special thanks to Dr. Jyothi Sadhu. His excellent work inspired my research. Although he always complained that we did not show enough respect to a senior guy, I could not thank him more for his help on finalizing the fabrication and measurement technique as well as theoretical interpretation. I also acknowledge Deepak Ganta for providing me the initial samples. I am very grateful that Jun helped me in the tedious and challenging work of wire bonding and Krishna helped me with sample characterization using TEM. I would also like to thank and show my respect to Marc. He not only helped me with my experiment, for example cutting a nanowire with FIB but also inspired me with his pursuing of perfection in research. I also learnt from Dhruv's enthusiasm and optimistic attitude toward life and research. I would also acknowledge other graduate students, Chen Zhang, Bruno Azeredo, Karthik Balasundaram and Xu Xie for their help and valuable discussion. Acknowledgment should also be given to the MNTL and MRL staffs, especially Tao Shang, Julio Soares, Lon Westfall and Tim Spila, your help made my research easier.

I was fortunate to have three of the best roommates in the past five years: Yinbin Miao, Tao Yang and Changqian Yu; I will always cherish the time we spent together, dinner, trips, and especially the long time chat late into the night. I also want to acknowledge my other good friends, to name a few , Xuan Zhang, Hefei Dong, Zhenduo Zhu and other friends from the lunch group. Without your company, my graduate life would be monotonous.

Finally, I want to thank my family. They have always supported all the decisions I have made. Confucius said, "If you have to make a long journey, you must reach a certain destination and let your parents know". PhD degree is just a checkpoint and I am still on the journey. No matter where I reach, home would always be my base camp.

TABLE OF CONTENTS

LIST OF TABLES

LIST OF FIGURES

LIST OF SYMBOLS AND ABBREVIATIONS

R	electrical resistance (Ω)
T	temperature (K)
k	thermal conductivity (W/(m· K))
S	Seebeck coefficient (μV/K)
V	voltage
C_V	heat capacity at constant volume (J/K)
k_B	Boltzmann constant (J/K)
f	frequency (Hz)
n	carrier/doping concentration (cm^{-3})
q	wave vector (m^{-1})
q''	power density (W/m^2)
σ	electrical conductivity ($\Omega \cdot cm^{-1}$)
ρ	density (Kg/m^3)
μ	mobility ($cm^2/(V \cdot s)$)
η	reduced Fermi energy
θ_D	Debye temperature (K)
τ	scattering time (s)
$\ddot{\gamma}$	Grüneisen parameter
ω	frequency shift in Raman spectrum (cm^{-1}) or angular frequency (rad/s)
Γ	spectrum width (cm^{-1})

CHAPTER 1

INTRODUCTION

1.1 Motivation and background

Cost-effective waste heat recovering technologies is important for improving energy efficiency. According to US Department of Energy, each year nearly 60% of the total energy generated is rejected in the form of waste heat, 2 TW of which is low quality waste heat (40 °C∼250 °C)[1]. Thermoelectric materials utilize the Seebeck effect to directly convert heat to electricity. Although thermoelectric devices may not be sufficient enough to play a role in large scale heat engines [2], they still have unique advantages [3]: for example, scalability which means it can be used in places where size and weight matter; better reliability due to no moving parts. A typical thermoelectric device involves a Π-leg module where heat flows from a p-type and an n-type semiconductor in parallel that generate a Seebeck voltage. Meanwhile free holes and electrons are driven from hot side to cold side thus forming electrical current flows in series across the p-type and n-type semiconductors. This is illustrated in Fig.1.1.

The conversion efficiency is quantified by the thermoelectric figure of merit $ZT = (S^2\sigma)/k$, where S is the Seebeck coefficient (with unit V/K), σ is the electrical conductivity, k is the thermal conductivity and T is the average operating temperature. Snyder et al. provided a rigorous analysis of thermoelectric efficiency [4]. If we assume constant properties with temperature, the maximum conversion efficiency for a thermoelectric generator working between high temperature T_H and cold side temperature T_C is calculated by Eq. 1.1 [5]

$$\eta_{max} = \frac{(T_H - T_C)\left(\sqrt{1+ZT_M}-1\right)}{T_H\left(\sqrt{1+ZT_M}+T_C/T_H\right)} \tag{1.1}$$

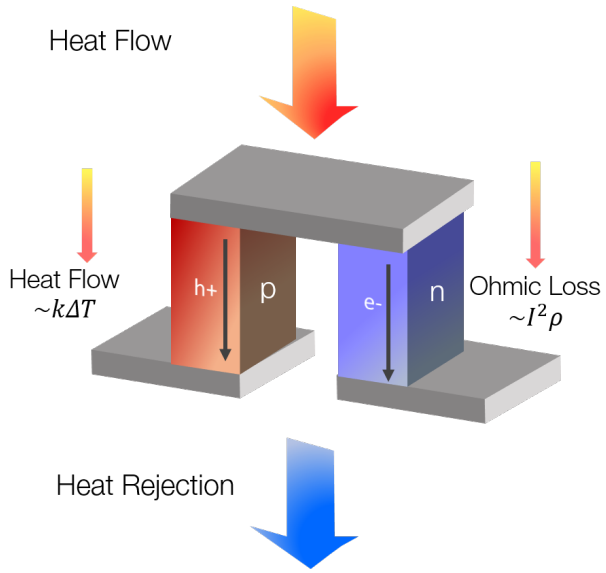

Figure 1.1: Illustration of a thermoelectric generator module with p-type and n-type semiconductors.

where $T_M = (T_H + T_C)/2$ is the average temperature. We see that when ZT approaches infinity, the thermoelectric conversion efficiency reaches Carnot efficiency. The difficulty to increase ZT arises from the fact that S, σ and k are mutually contra-indicated in a material. We require a good thermoelectric material to have low thermal conductivity, high electrical conductivity and Seebeck coefficient. When we try to increase the electrical conductivity by increasing charge carrier concentrations, Seebeck coefficient will be reduced; when we suppress the thermal conductivity by introducing more scattering, charge carrier mobility will be reduced at the same time. The most widely used bulk thermoelectric materials at relative low temperature (below 200 °C) are alloys of Bi_2Te_3 and Sb_2Te_3 [6] with ZT peaks around 1.

From 1990s, researchers started to investigate the possibility of using nanostructures to increase ZT by independently engineering one property without affecting the others. As an example Hicks and Dresselhaus [7, 8] theoretically pointed out that with quantum well superlattice structure or 1D quantum wire, $S^2\sigma$ was enhanced while k was lowered by phonon surface scattering. Attempt on Bi nanowires embedded in porous alumina and silica showed enhanced thermoelectric power [9] and was consistent with theoretical prediction. Experimental realization of enhancement in power factor was demon-

strated in other nanostructured systems, such as Bi_2Te_3/Sb_2Te_3 supperlattice [10], PbSeTe/PbTe quantum dot superlattices [11]. However the most understood benefit of using nanostructure in thermoelectric is the reduced lattice thermal conductivity due to increased phonon scattering. Several papers reviewed the recent progress in nanostructured thermoelectric material [12, 13, 14, 15, 16, 3].

1.2 Thermoelectric study on silicon nanowire

The possibility of using silicon as a thermoelectric material for waste heat recovery is technologically significant due to silicons economy of scale and vast processing knowhow. However, the major draw back was its high thermal conductivity (at room temperature, 148 W/(m·K) for intrinsic silicon and about 90 W/(m·K) for degenerately doped silcon). Thermal conductivity of Si consists of lattice contribution k_L and electronic contribution k_e. k_e can be estimated by Wiedeman-Franz law $k_e = LT$ where $L = 2.44 \times 10^{-8}$ W Ω K^{-2} is Lorentz number. For 1×10^{19} cm^{-3} carrier concentration, $k_e \sim 0.7$ W/(m·K) at 300 K. Hence the lattice contribution to thermal conductivity dominates. Electronic mean free path (MFP) in doped Si is less than 10 nm whereas the phonon MFPs contributing to heat conduction are above 100 nm up to several μm shown by most recent first-principle calculations [17] and experimental work [18, 19]. The cumulative thermal conductivity and electrical conductivity as a function of carriers MFP is shown in Fig. 1.2 (adopted from Ref. [20]), where the electron conductivity is calculated from scattering rates [21]. As a result, by engineering silicon nanostructure to have critical dimension above 10 nm, we may bring down lattice thermal conductivity by increased phonon scattering but meanwhile keep electrical conductivity non-disturbed.

Boundary scattering reduces the thermal conductivity of Si and has been well studied and understood in thin film Si. The Casimir limit refers to the thermal conductivity under diffuse scattering of phonons at the boundaries [22]. In 2008, Boukai et al. [23] and Hochbaum [24] et al. showed that

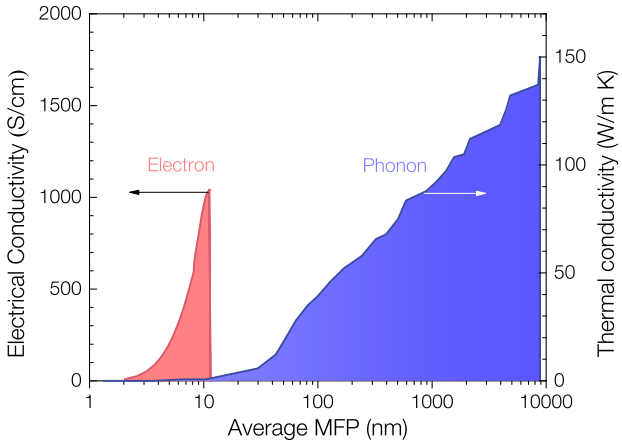

Figure 1.2: Theoretical cumulative contributions of electron and phonon mean free path (MFP) to silicon electrical and thermal conductivity at 300 K. The result of phonon MFP is from first principle calculation [17] and figure adopted from Ref. [20].

$ZT > 0.6$ under room temperature can be achieved by silicon nanowire. After that solid crystalline NW especially with surface roughening has been investigated in great detail though are not fully conclusive. We summarize some representative thermal conductivity data of silicon nonowires in Fig. 1.3 [25, 26, 27, 20] and as a comparison, nanomesh data [28] is also shown. We can see from the figure that Si nanowires with diameters less than 100 nm, progressively deviate from the Casimir limit, these results are still debated in the literature. The low thermal conductivity of porous silicon nanowire (about 2 W/(m·K) at room temperature) is convincing, because porous silicon itself is known to have very low thermal conductivity and we will discuss this in detail in Chapter 2. In our previous study, we also found that the phonon drag effect was quenched in nanowire [20]. However we discovered that Seebeck coefficient porous silicon nanowire was close to bulk value while maintaining an ultra low thermal conductivity, which indicated that porous silicon nanowire may have the potential of being good thermoelectric material. The issue remains with poor charge transport (electrical resistivity is of the order 10^4 Ω·cm and is 7 orders of magnitude larger than bulk value at same doping) and that is the focus of the thesis.

We've previously demonstrated enhancement of electrical conductivity of smooth nanowire [29], recently Boor et al. [30] showed that by post doping,

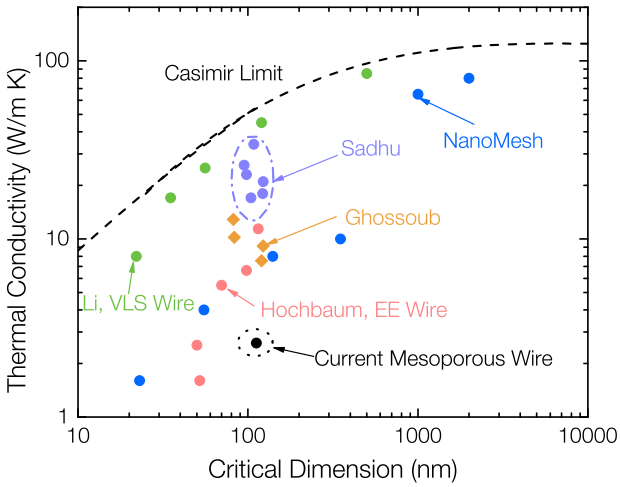

Figure 1.3: Representative thermal conductivity data of nanowire or nano structure silicon at room temperature.

electrical conductance of lightly doped porous silicon (6×10^{17} cm^{-3}) was improved. Here in the thesis we investigated the feasibility of enhancing the electrical conductivity of degenerately doped porous silicon wire by post doping and its thermoelectric properties afterwards.

1.3 Thesis structure

In Chapter 2, we first reviewed the up-to-date progress on the porous similar structured silicon as thermoelectric material. In Section 2.2 we provide a detailed review with emphasis on experimental work on study of thermal transport phenomena in porous nano structures including both 2D and 3D cases, such as holey silicon, inverse opal, porous silicon and etc. In Section 2.3 we discuss about the carrier transport properties in porous silicon.

In Chapter 3, we first discuss the porous nanowire fabrication including the pore formation mechanism in Section 3.1. We introduce the technique that simultaneously measures Seebeck coefficient and thermal conductivity of porous silicon nanowires at frequency domain in Section 3.2. We also discuss electrical conductivity measurement by two-point probe at array scale or four-point probe measurement of single nanowire in Section 3.3. By employing Raman spectroscopy we can extract information of nanowire such as

crystalline size and carrier concentration and this is discussed in detail in Section 3.4.

In Chapter 4 we report the Seebeck coefficient of porous nanowire under different doping conditions and temperature range from 30 K to 400 K. The Seebeck data show clear characteristic of carrier diffusion contribution. For those degenerately doped nanowire, we could extract the effective carrier concentration from a simple Mott formula interpretation, we further interpret the data using more strict approach.

In Chapter 5 we report the thermal conductivity of porous nanowire with different doping condition from 30 K to 400 K. We discuss different aspects that may contribute to the reduction from both scattering and coherent transport approach. The major challenge is to correctly model the scattering introduced by the randomly distributed pores. Effect of porosity is also discussed by effective medium theory.

Chapter 6 summarizes our conclusion and future direction in developing practical porous silicon nanowire based efficient thermoelectric generators.

CHAPTER 2

REVIEW OF LITERATURE

2.1 Porous silicon as thermoelectric material

Porous silicon has long been a material of interest for silicon based optoelectronics mainly because of its photoluminescence property [31, 32, 33]. Its potential for thermoelectric application arises from its low thermal conductivity which will be discussed in detail in following section. Thermoelectric power i.e. Seebeck coefficient and DC electrical conductivity measurements were first conducted on macro-porous silicon (pore size > 50 nm) by Mathur et al. in 1998 [34] to investigate the transport properties in porous silicon. Yamamoto et al. [35] evaluated the potential of porous silicon as a thermoelectric material by performing in-plane measurements of a self-supporting porous silicon film fabricated from degenerately doped substrate. The measured thermal conductivity was two orders of magnitude lower than the bulk substrate while the electrical conductivity was $3\sim 5$ orders lower. For sample with 69% porosity they observed an increase in Seebeck coefficient and as a result the overall figure of merit Z exceeded 10^{-4} K^{-1} which was higher than the bulk value. However we have to point out that the Seebeck coefficient depended on the measurement condition in Yamamotos experiment [35], in another words the measured values were different at ambient and vacuum condition.

The largest drawback in porous silicon as a thermoelectric material is the ultralow electrical conductivity. Recent theory [36] and experiments [37, 28] have focused on silicon with ordered pores such as holey Si [37] and nanomesh [28] where the ordering can help electron charge transport while reducing heat transport. From those results, thermal conductivity was reduced

with decreasing critical dimension which was pitch of the pores and lowest value experimentally achieved was lower than 2 W/(m·K) at room temperature [37, 28] ; they also reported that the electrical properties were either preserved [37, 28] or lowered by 2∼4X [36] while S remained close to bulk value [36]. Overall, ZT up to 0.4 at room temperature was achieved [37]. Boor et al. did a detailed study on thermoelectric properties of porous silicon membrane (70 ∼90 µm thick and size of about 0.25 cm^2) fabricated from low doped silicon ($\sim 6 \times 10^{17}$ cm^{-3}). By post-doping process they were able to improve the electrical conductance compared with the as-etched porous silicon. The effective thermal conductivity of sample with 0.6 porosity was about 7.6 W/(m·K) at room temperature. Through a direct transient Harman technique they showed a $ZT > 0.02$ for p-type porous silicon which exceeded that of bulk silicon at optimal doping concentration ($\sim 1.9 \times 10^{19}$ cm^{-3}).

2.2 Thermal transport in porous silicon

2.2.1 Thermal transport study in ordered porous Si

Porous silicon has been investigated as a potential thermoelectric material due to its low thermal conductivity. However its electrical conductivity was also drastically reduced. Previous theory and experiments have focused on ordered pores or so-called holey Si where the ordering can help electron charge transport while reducing heat transport.

Song and Chen [38] did the first experimental work on in plane thermal conductivity measurement of a free-standing single crystal silicon film with periodically arranged through holes. The freestanding membranes were fabricated from silicon-on-insulator (SOI) wafer with ∼4.5 µm thick low-doped n-type device layer, then round through pores with nominal diameter of 2 µm or 10 µm which were arranged aligned or staggered rows were etched by DRIE. Song et al. applied steady-state Volklein technique to measure the in plane thermal conductivity [38]. Heater and thermometer were placed at

each end of the free-standing membrane, the film thermal conductivity was extracted based on the temperature difference measured and estimation of heat flux which required knowledge of thermal conductivities of other materials in the heat flow path. They discovered strong size effect that all the porous films had thermal conductivity lower than predicted by porosity and bulk silicon mean free path, and film with smaller pore spacing had smaller effective thermal conductivity. The reduction of thermal conductivity was insensitive to pore arrangement. For porous film of 0.26 porosity with pore diameter 2.3 µm and spacing 4 µm (center to center), the effective thermal conductivity was about 44 W/(m·K) at room temperature.

Later in 2010, Yu et al. [28] reported in-plane thermal conductivity of nanomesh fabricated by superlattice nanowire pattern transfer (SNAP) technique from SOI wafer. Nanomesh had thickness about 20 nm and pore diameter 11 or 16 nm, in both cases the center to center pitch was 34 nm. Yu et al. employed a suspended heating and sensing platform developed by Shi et al. [39]. The measured thermal conductivity at room temperature went down to 1.9 W/(m·K). They also observed that the bulk like electrical conductivity was preserved in the high doping range. In the same year, Tang et al. [37] measured thermal conductivity of holey silicon using the same technique. Holey silicon with hole pitches 350, 140 and 55 nm was prepared by either nanosphere lithography or block copolymer lithography [37], porosity of those samples was about 35%. For 55 nm pitch holey silicon, room temperature thermal conductivity down to 1.14∼2.03 W/(m·K) was reported. Hopkins et al. [40] fabricated another type of ordered porous silicon structure namely phonoic crystal which had thickness 500 nm and pore spacing of several hundreds of nanometers. The phononic crystals measured in the paper had porosity 0.19, 0.25 and 0.28.They measured the room temperature thermal conductivity of phononic crystals by time-domain thermalreflectance (TDTR) technique, a minimum value 4.81 ± 1.0 W/(m·K) was obtained for sample with 400 nm hole diameter, 700 nm center to center spacing and 0.25 porosity. Marconnet et al. [41] fabricated a similar periodically porous silicon beam which was named nano-bridge or nano-ladder. Those nano-bridges with dimensions 570 nm width and 18.8 µm length had 24 pores spaced by 385 nm, diameters of which were 110 nm, 210 nm and 280 nm. They mea-

sured thermal conductivity of those ladders to be 54, 3.7 and 3.4 W/(m·K) with 1D heat transfer assumption. The limiting dimension here was the distance between pore edge and hence the the structure with largest pore had smallest limiting dimension.

Besides those in-plane measurement on two-dimensional or two-dimensional like material discussed above, researchers have also studied cross-plane thermal conductivity of three-dimensional ordered porous structures. Fang et al. measured the cross-plane thermal conductivity of ordered mesoporous nanocrysalline silicon thin film between 25 K and 315 K using 3ω method [42]. The thin silicon films were fabricated by evaporation-induced self-assembly of mesoporous silicon followed by magnesium reduction [42] . They had quite unform periodic ordering of pores with average crystalline size $\sim$13 nm and $25 \sim 35\%$ porosity characterized by X-ray diffraction (XRD). Film thickness ranged from 140$\sim$340 nm. The effective thermal conductivities at room temperature were between 0.23 ± 0.02 W/(m·K) and 0.37 ± 0.03 W/(m·K). Another 3D periodic silicon structure was fabricated and characterized in the form of inverse opals by Ma et al. [43]. Amorphous silicon was deposited by CVD into the opal template comprised of silica spheres and recrystallized to produce polysilicon. Then BOE etched away the silica template and left with inverse opal structure. The result periodicities and shell thicknesses were $420 \sim 900$ nm and $18 \sim 38$ nm by SEM and XRD. They also measured the cross-plane thermal conductivity by 3ω method from 30$\sim$400 K and observed effective thermal conductivity as low as about $0.6 \sim 1.4$ W/(m·K).

Apart from experimental work, people also modeled thermal transport process in ordered porous structures. For example, molecular dynamic simulation [44, 36, 45], Monte-Carlo simulation [46, 47]. Atomistic simulations provided more insight into the role of various phonon scattering mechanisms, particularly surface scattering while the Monte-Carlo simulation revisited the Boltzmann transport simulations while considering frequency dependent scattering rates. We will discuss some of the theoretical approach in detail in Chapter 5 when explaining our thermal conductivity data.

2.2.2 Thermal transport in nano/mesoporous Si

Porous silicon is one of the most studied meso-porous nanoporous structure. It is usually fabricated by electrochemical etching in aqueous or ethanoic HF solution [48, 49]. According to IUPAC's guideline [50], the morphology of porous silicon is generally classified by pore size and meso-porous is defined for pore dimension ranging from 2 to 50 nm [32]. Lysenko et al. [51] proposed a categorization that is based on the crystalline size: nanoporous (1∼5 nm crystallites), meso-porous (5∼100 nm crystallites) and macro-porous (100∼1000 nm) . In this section, we present an overview of thermal conductivity in porous silicon to serve as a limiting case for periodically holey structures that are essentially porous structures with ordered pores.

Table 2.1: Selected literature values of room temperature thermal conductivity data of nano/meso-porous silicon.

Reference	k **W/(m·K) @300K**	**Porosity**	**Nano-crystalline size**	**Measurement technique**
Lang 1994 [52]	1.2∼1.8, 2.7 (meso-porous)	0.4, 0.53 0.45	3 nm or 10 nm	heater sensor phase difference
Gesele 1997 [53]	down to 0.03	0.64∼0.89	1.7∼ 9.0 nm	3ω
Benedetto 1997 [54]	2.5, 3.9, 31.2	0.6, 0.5, 0.4	n.a.	photo-acoustic
Bernini 1999 [55]	1.2, 3.5	0.57, 0.42	n.a.	thermal wave interferometry
Lysenko 1999 [56]	0.3 ∼ 4.6	0.73, 0.62, 0.38	4.0, 7.2 and 8.3 nm	micro-Raman
Yamamoto 1999 [35]	< 1	0.69 ∼ 0.85	n.a.	AC calorimetry

Continued on next page

Table 2.1 – *Continued from previous page*

Reference	k **W/(m·K) @300K**	**Porosity**	**Nano-crystalline size**	**Measurement technique**
Lysenko 2000 [57]	0.5, 1.9	n.a	nanoporous mesoporous	scanning probe microscopy
Périchon 2000 [58]	0.3, 0.7	0.7, 0.5	n.a.	micro-Raman
Bernini 2001 [59]	0.15	0.61	n.a.	optical pump-probe
Shen 2003 [60]	0.2	$0.2 \sim 0.6$	0.6	photo-acoustic
Lettieri 2005 [61]	0.29, 1.03, 2.93	0.72, 0.57, 0.40	n.a.	photo-acoustic
Wolf 2006 [62]	2.3	0.662	n.a.	lock-in thermography
Gomès [63]	1.7, 2.8, 3.8	0.8, 0.54, 0.3	$10 \sim 20$ nm	scanning thermal microscopy
Srinivasan 2007 [64]	$2.93 \sim 8.31$	$0.45 \sim 0.64$	∼6 nm	photo-acoustic
Boor 2011 [30]	$3.3 \sim 24$	$0.17 \sim 0.66$	7.2 nm∼ 114 nm	3ω
Weisse 2012 [65]	~ 1	n.a.	n.a.	nanosecond TTR
Valalaki 2013 [66]	∼0.2	0.6	n.a.	DC method

The first reported value of thermal conductivity for porous silicon at room temperature is 1.2 W/(m·K) [52] for nano-porous silicon (40% porosity). In the same work, the thermal conductivity of as-prepared meso-porous silicon (45% porosity) was measured to be 80 W/(m·K) which dropped to 2.7 W/(m·K) upon oxidation at 300 °C. Temperature dependent measurements in the range of 35∼320 K using the 3ω method were first reported by Gesele et al. [53] The thermal conductivities of all the investigated samples increased with increasing temperature, and were less than 1 W/(m·K) at room temperature. A minimum value of 0.03 W/(m·K) was reported for p-type porous silicon with 89% porosity and 4.5 ± 0.6 nm crystallite size. Besides the techniques mentioned above, researchers have adopted a variety of methods, such as photo-acoustic measurements [54], thermal wave interferometry [55], micro-Raman scattering [56], optical pump-probe method [59], and scanning probe microscopy [57]. A detailed list of porous silicon thermal conductivity data till date is summarized in Table 2.1.

The ultra-low thermal conductivity in nano/meso-porous silicon is mainly attributed to strong phonon confinement and scattering at the crystallite boundary. Further, porosity also plays an important role in reducing the effective thermal conductivity, which can be explained by various effective medium theories. Theoretical approaches to model phonon transport in porous silicon include, for example, solution of the BTE by the discrete ordinate method [67], 3D Monte-Carlo simulations [68], molecular dynamic simulation [36, 44] and a combination of analytical and phonon-tracking methods [69]. It remains a challenge to clearly understand thermal transport in a non-periodic porous structure and this is our major work in Chapter 5.

2.3 Electrical transport in porous silicon

Electrical conductivity os porous silicon is very low and this was simply attributed to the substantially deteriorated electronic structure [36]. Electron transport in such a s disordered system with possible quantum confinement is a complicated and yet not fully understood process. The basic electron

transport path is usually considered to be through the solid crystal network, other than that there are many other suggested transport paths and mechanisms, to name a few, diffusion or tunneling between the Si crystal or on its surface; transport from surrounding the nanocrystals and varieties of hopping transport [33]. It was also reported that due to the large surface area, the electrical properties are sensitive to environment [33, 49].

The nominal division between macro-porous mesoporous and micro-porous cannot distinguish the electrical property variation [49]. The critical size should be the dimension of nano-crystalline, which is not directly related to the pore size or average porosity. It was suggested that the porous silicon can be separated into two groups by the existence of quantum confinement effect [49].

For porous silicon which does not show quantum confinement , the sample with 40∼50 % porosity had room temperature resistivity similar to that of intrinsic silicon although those samples were fabricated from highly doped substrate. On the other hand, porous silicon which has nano-crystalline shows quantum confinement and the resistivity of those nanocrystalline porous silicon ranges from 10^{10} to 10^{12} Ω·cm. The loss the free carriers was mainly attributed to compensation by surface states whose trap density was in the range of 10^{19} cm^{-3} [49]. Trapping may also due to the binding energy of dopant impurities are increased [33]. Through a study of acceptor depletion [70], the dopant was preserved after preparation process however they were in a neutral state, which agrees with our SIMS measurement of nanowire. The widening of bandgap induced by quantum confinement also reduces the thermal generation of free carriers [33].

Electrical measurement shows that porous silicon has distinct DC and AC conductivity. Many previous studies reported that the DC conductivity had an activation behaviour [33, 49] as described below

$$\sigma(T) = \sigma_0 \exp(\frac{-E_A}{k_B T}) \tag{2.1}$$

where $E_A \simeq 0.5$ eV is the activation energy which is about half of the bandgap extracted from luminescence measurement and comparable to that of intrinsic silicon [33, 49]; pre-factor σ_0 is a constant and varies for different samples. In porous silicon with quantum confinement, below 200 K the electrical conductivity is almost temperature independent [71]. The activation behaviour indicates that there are other mechanisms besides quantum confinement: disordered crystalline skeleton not only imposes geometrical effects on the electron transport but also localize the free carriers [33]. As a result the measured activation energy can be related to either the activation of carriers over mobility edge or carrier hopping energy barrier [33]. Lubianiker et al. [72] found that the activation energy E_A and pre-factor σ_0 followed Meyer-Neldel rule (MN) $\ln(\sigma_0) = \sigma_{MN} + E_A/E_{MN}$ where constants σ_{MN} and E_{MN} are signature of a specific transport mechanism. They observed two Meyer-Neldel rules for the porous silicon DC conductivity, which may correspond to two possible transport mechanisms: extended state transport and thermally activated band-tail hopping [72].

Though not attempted in our measurement, it would be useful to discuss the AC conductivity of porous silicon. Bisi et al. [33] pointed out that the AC conductivity probed the local conductivity of porous silicon and can possibly reveal the electron transport mechanism in porous silicon. Several groups carried detailed study on investigation of AC conductivity of porous silicon [71, 73] which was a function of frequency as well as temperature. For frequency response, the real part of AC conductivity has a frequency dependent signature of $\sigma(f) \propto f^n$, where n varies at different frequency range and the cross-over frequency also depends on temperature. For frequency below the low temperature cross over point f_0 (<1 Hz), $n = 0$ i.e. AC conductivity equals DC electrical conductivity; At high frequencies, $n \sim 0.95 \pm 0.05$ and is almost temperature independent which may suggest a finite density of states at the Fermi level [49]. The crossover frequency f_1 increases with increasing temperature, at around room temperature $f_0 \sim 10000$ Hz; For frequency in between f_0 and f_1, $n \simeq 0.3 \sim 0.5$ [49].

AC electrical conductivity of porous silicon also has an activation behaviour. We adopted the figure from Ref. [71, 33] as shown in Fig. 2.1. At above 200 K, DC conductivity is activated while AC conductivity is acti-

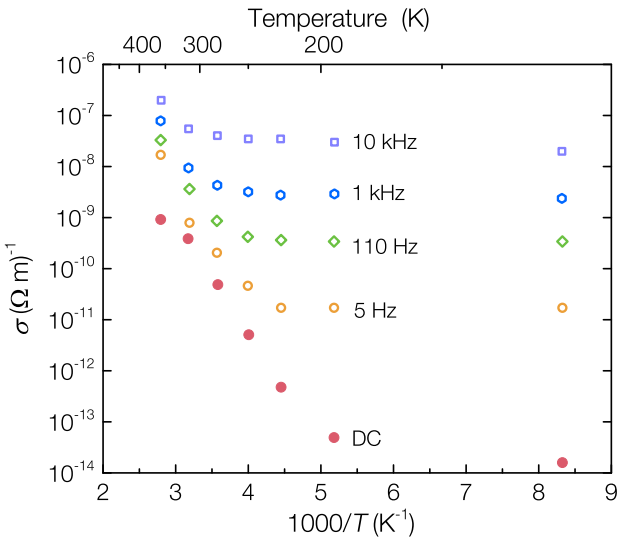

Figure 2.1: Electrical conductivities of porous silicon as a function of inverse temperatures at different frequencies. Figure adopted from [71]

vated at higher temperature and at high frequency (>> 10000 Hz) activation disappears. At low temperature, AC conductivity is saturated. The temperature independent high frequency electrical conductivity was regarded in Ref. [71] as a typical behaviour of hopping transport in the vicinity of Fermi level. However Francia et al. suggested that surface states transport also exists in addition to hopping and the transport was a double-channel process [74].

Three types of mobility which are conductivity mobility, drift mobility and Hall mobility have been measured [49]. Here we mainly focus the drift mobility. The drift mobility was investigated by steady-state photocarrier grating (SSPG) technique [75] or time-of flight (TOF) technique [76, 77]. Transient current [75, 76, 77] or transient voltage drop [76] was measured to estimate the transport parameters. Although samples tested in Ref. [76, 77] were made from boron doped p-type silicon, both holes and electrons are carriers. The transport of carriers are dispersive which means mobilities have a power law decay with time or length-scale [76, 77]. A spread of drift mobility values have been reported, usually on the order of 10^{-3} cm^2/V s [49, 76] or $< 10^{-4}$ cm^2/V s [49, 77]. There are not clear difference between quantum confined or not confined samples [49]. The reason for the reduction in mobility is debating. In porous silicon, thermally activated electrons/holes move in extended states are disturbed greatly by multiple trapping with the surface states and

causing a reduction in mobility. Others suggested that the disordered structure geometry i.e. transport path may be the main reason that limiting the mobility [76, 77].

The drift mobility increase with increasing temperature which is a characteristic of ionized impurity scattering. Rao et al. demonstrated this phenomenon in their measurement [77]. We conducted two-point probe measurement on as-etched porous silicon nanowire arrays from 220 K to 400K and extracted the mobility by assuming carrier concentration same as the substrate value. The mobility temperature trend agrees with that in Ref. [77] and will be discussed in detail in Chapter 4.

CHAPTER 3

SAMPLE FABRICATION AND CHARACTERIZATION TECHNIQUE

3.1 Porous nanowire fabrication and post-doping

3.1.1 Porous silicon nanowire fabrication

Metal assisted chemical etching (MACE) [48, 78] is a cost-effective electroless method to fabricate silicon nanowire on large scale silicon wafer. A typical etchant is combination of acid (normally HF) and oxidative agent (usually H_2O_2). Huang et al. summarized this etching process as a five-step picture [78]. When silicon wafers covered with noble metal (in our case, Au) of specific pattern is subjected to the etchant, because of the catalytic effect of the noble metal, the oxidant is preferably reduced at the silicon/noble metal interface and generates large amount of holes, and silicon is oxidized by the holes and then etched away by HF. The silicon underneath the noble metal etches much faster than the area without metal coverage due to the high hole concentration. Studies have shown that MACE on degenerately doped silicon (doping concentration larger than 10^{18} cm^{-3}) normally produces porous nanostructures for both p-type [79] and n-type silicon [80]. Possible reasons of pore formation may originate from the diffusion of holes to the off-metal area [79] and Hochbaum et al. [81] suggested that the hole injection may be favored in highly doped silicon due to the less band bending at the Si/etchant interface and therefore more holes are available for diffusion to the off-metal region.

This MACE process is highly anisotropic and thus we need a gold mesh template to form nanowire structure with certain diameter. This template

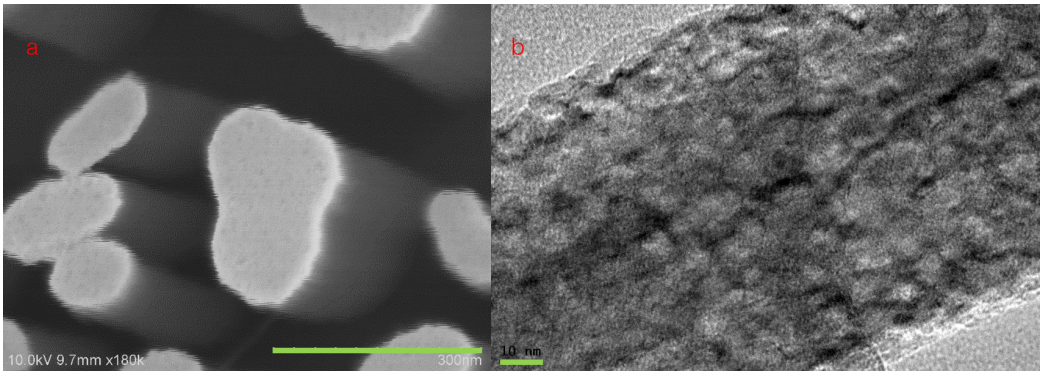

Figure 3.1: (a) Tilted view of silicon nanowire array by SEM, from the image we can clearly see the pores (scale bar 300 nm). (b) TEM image of a porous wire (scale bar 10 nm).

fabrication can be done in many ways [78], like photolithography, nanosphere lithography [82, 83] and etc. Here we utilized a thermal annealing dewetting method [84] to generate the Au pattern. First we deposited a thin Ag film on a clean silicon wafer and annealed the silver film subsequently at 350 °C for 5∼6 hours under 3×10^{-7} Torr pressure. This annealing process dewetted the Ag film to form particles whose size is determined by Ag film thickness, deposition rate, annealing temperature and time. In our silicon nanowire fabrication, with 22∼23 nm Ag film deposited at 1 Å/s and the anneal condition mentioned above, we obtained Ag particles with diameter 80∼150 nm and area coverage 32% ∼ 42%. Then we deposited 10∼11 nm Au at 0.5 Å/s rate and did silver lift-off to obtain an Au mesh. To fabricate silicon nanowires with controlled pore size distribution, we varied the volumetric ratio of HF:H_2O_2 etching time and temperature [85]. For porous nanowires studied in this paper, we started with p+ silicon wafer (0.001 ∼0.005 Ω·cm) and used HF: H_2O_2 =30:1 as etchant under room temperature. The etching rate was roughly 1 µm/min. Figure 3.1 shows the SEM and TEM image of the porous wire.

3.1.2 Post-doping process

We used solid source diffusion of dopants in an *ex situ* manner to make nanowires more conductive [86, 87] and we have successfully demonstrated enhanced electrical conductivity in the silicon nanowire initially etched from

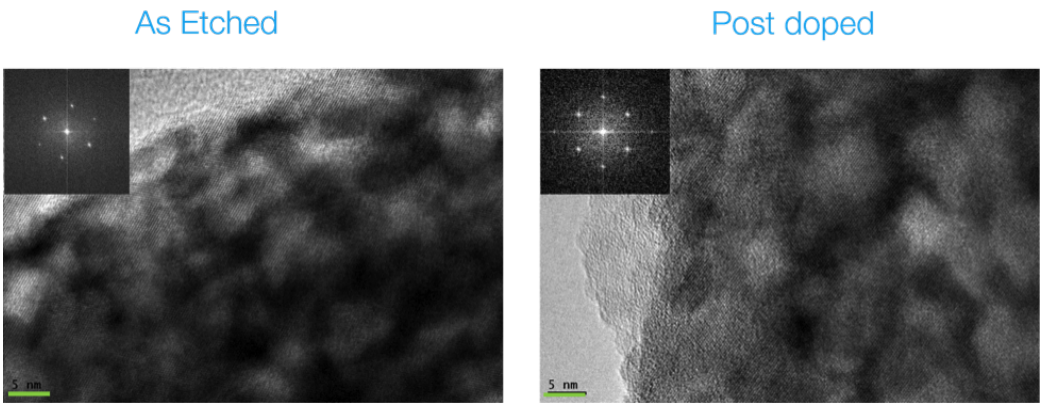

Figure 3.2: TEM images of as-etched nanowire and post-doped nanowire. We can tell that the porous nanowire remained crystalline after being post-doped.

low-doped silicon substrate [29] by using spin-on dopant (SOD). We spin-coated the nanowire by SOD (Borofilm 100 from EMULSITONE CHEMICALS, LLC.) at 3000 rpm for 30 sec, about 30 sec dwelt time before spinning was enough to completely wet the nanowire surface. The spinning speed and time can be tuned according to the length of nanowires. After baking the sample at 270 °C for 15 min, we annealed the sample at a chosen temperature and time to activate the boron and this is called pre-deposition. By choosing the doping temperature and time we can control the doping concentration and uniformity. Borosilicate glass was formed during this procedure and it was removed by BOE etching. The final step was a drive-in process at a higher temperature. We did not use a thin oxide barrier layer as in the low-doped nanowire case [29] since the porous structure may be damaged in the oxidation and etching process. The post-doped porous silicon nanowire remained crystalline and this was verified by TEM.

The p+ wafer had resistivity value 0.001∼0.005 Ω·cm which corresponds to a boron doping concentration of about and was later confirmed by SIMS. As a result, in order to achieve higher doping concentration we should carry the post-doping process at above 800 °C based on the boron solubility in silicon [88, 89]. Our silicon nanowire normally has celery like cross section due to the randomness in dewetting process and it is challenging to accurately model the diffusion profile. However we can always estimate the temperature and time required for targeted doping concentration by solving the diffusion equation

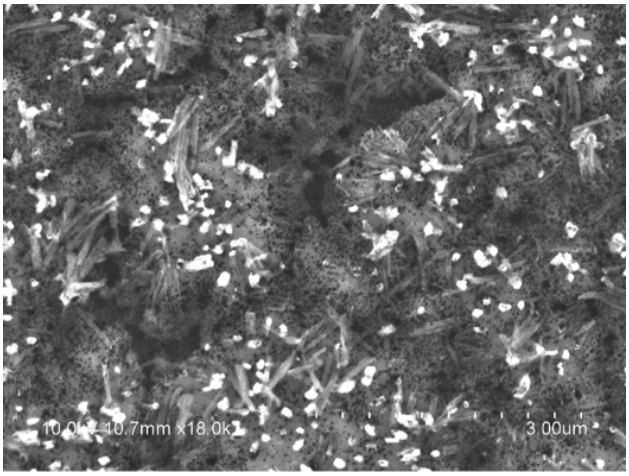

Figure 3.3: Top view SEM of porous silicon nanowire after annealing at 1000 °C. It is possible that most part of the nanowire becomes borosilicate and later removed by BOE.

in a radial system. The dopant concentration on nanowire surface is fixed to the solubility limit N_{sl} at doping temperature and the radius r_0 can be taken as the critical size in the celery cross section (half of the minor axis). The time dependent concentration $N(r,t)$ in the nanowire cross section is then described by [90]

$$\frac{N(r,t)}{N_{sl}} = 1 - 2\sum_{k=1}^{\infty} \frac{J_0[\lambda_k\,(r/r_0)]}{\lambda_k J_1(\lambda_k)} \exp\left(-\frac{D\lambda_k^2}{r_0^2}t\right) \tag{3.1}$$

where D is dopant diffusivity in silicon at temperature T, is the k_{th} zero of the Bessel function J_0. We found the pre-deposition of dopant at 950 °C over 15 min yields uniform doping concentrations across the cross section of a nanowire [29].

What would be the upper limit for pre-deposition temperature? We first tried 1000 °C and most of the silicon surface was no longer covered by nanowire as shown in Fig. 3.3. Possible reason was that at this temperature most of the nanowires became borosilicate glass and were later removed by BOE. After lowering the activation temperature to 950 °C, the nanowire sample survived after the post-doping process. So we have chosen the pre-deposition temperature range to be 800 ∼950 °C at a 50 °C step.

To verify that this post-doping procedure introduced more boron atoms

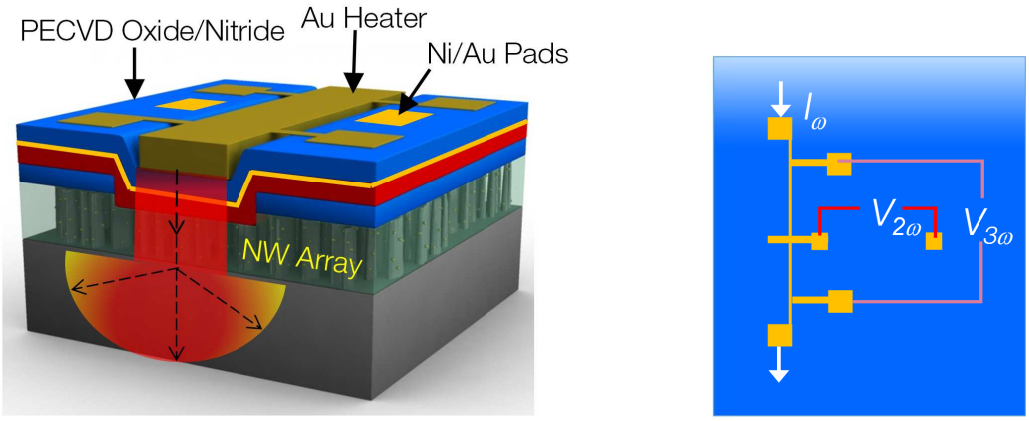

Figure 3.4: Frequency domain Seebeck coefficient and thermal conductivity measurement platform.We show the measured signal in the top view.

to the degenerately doped porous wire, we characterized the doping concentration by secondary ion mass spectroscopy (SIMS). In SIMS measurement, a primary ion beam (Cs^+ for n-type and O_2^- for p-type) was used to etch the sample and for depth profiling, the sputtered ions from the sample were collected and counted. We also measured another standard ion-implanted sample with known dose to extract the relative scaling factor (RSF) for the dopant species. The etching depth was obtain by profilometry measurement.

3.2 Seebeck coefficient and thermal conductivity measurement

3.2.1 Measurement principle and data reduction

To measure the crossplane Seebeck coefficient and thermal conductivity of silicon nanowire, we employed and improved a frequency domain measurement based on the 3ω technique [91] which was previously applied by Yang et al. [92] in characterizing the thermoelectric properties of SiGe superlattice at room temperature. The platform is illustrated in Fig. 3.4.

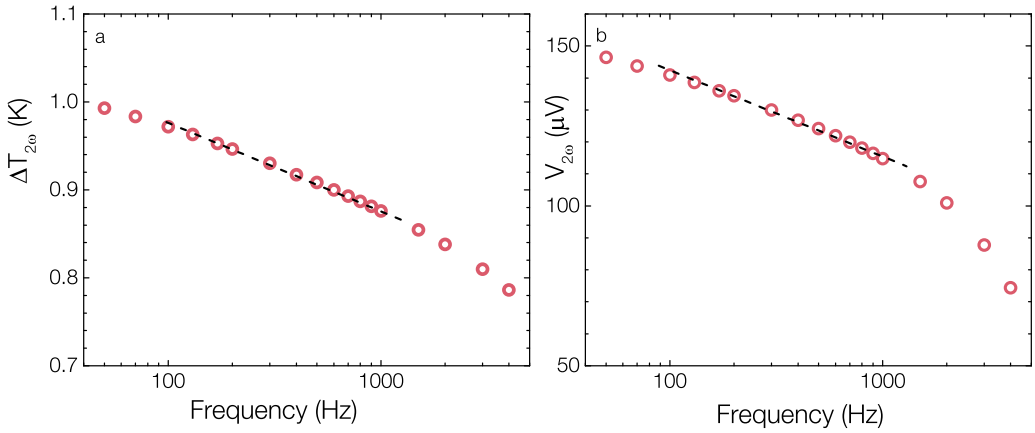

Figure 3.5: Representative plot of measured $\Delta T_{2\omega}$ and $V_{2\omega}$ as a function of frequency.

By sending sinusoidal current of frequency ω through the external Au heater, we set up a temperature field across the structure caused by. In addition to the DC component, the heat is generated at frequency 2ω. The corresponding temperature rise of the heater with amplitude ΔT also oscillates at frequency 2ω but usually out of phase by a frequency dependent angle $\phi(\omega)$. $\Delta T_{2\omega}$ consists of temperature drop at insulation layer $\Delta T_{2\omega,ins}$, NW layer $\Delta T_{2\omega,NW}$ and substrate $\Delta T_{2\omega,sub}$. The voltage drop across heater line has both 1ω and 3ω portion which can be used to extract the temperature increase $\Delta T_{2\omega}$ as shown in Eq. 3.2 [91]

$$\Delta T_{2\omega} = \Delta T_{2\omega,NW} + \Delta T_{2\omega,ins} + \Delta T_{2\omega,sub} = 2\frac{1}{dR/dT}R_0\frac{V_{3\omega}}{V_{1\omega}} \tag{3.2}$$

where dR/dT is obtained from the heater resistance-temperature calibration, R_0 is the resistance of heater at measurement temperature. Since the Seebeck voltage follows the temperature field, the open circuit voltage at 2ω frequency measured between the two metallic pads as shown in Fig. 3.4 is the corresponding Seebeck voltage $V_{2\omega}$. Again it has contribution from nanowire array and substrate as described in Eq. 3.3

$$V_{2\omega} = V_{2\omega,NW} + V_{2\omega,sub} = S_{NW}\Delta T_{2\omega,NW} + S_{sub}\Delta T_{2\omega,sub} \tag{3.3}$$

A representative plot $\Delta T_{2\omega}$ and $V_{2\omega}$ as a function of measurement frequency is illustrated in Fig. 3.5.

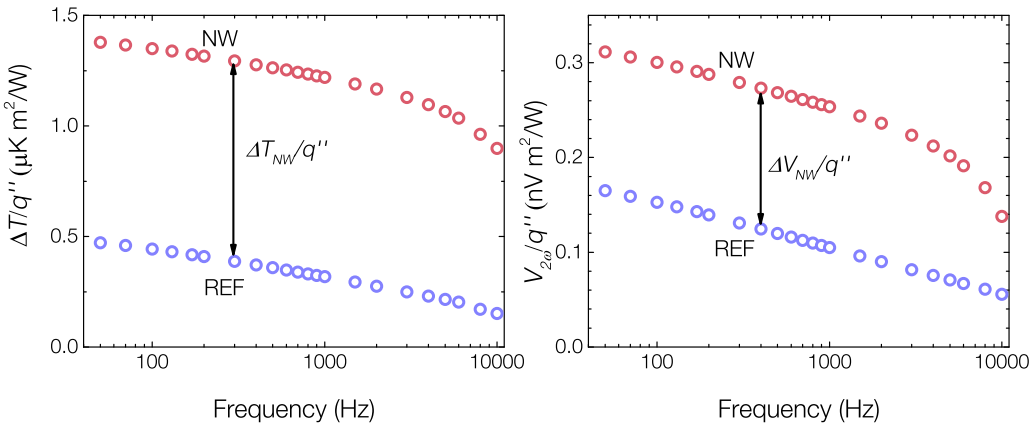

Figure 3.6: Representative plot of measured $\Delta T_{2\omega}/q''$ and $V_{2\omega}/q''$ as a function of frequency for both the NW sample and reference sample.

In order to extract the properties of nanowire layer we need to subtract the contribution from insulation layer and substrate. This is achieved by conducting a differential measurement on a reference sample which is the substrate with same insulation layer. Considering the difference in the amount of heat put into the system, we normalize the temperature increase and Seebeck voltage by power density, as illustrated in Fig. 3.6 and as a result the temperature the corresponding voltage drop across the NW layer are described in Eq. 3.4

$$\begin{aligned} \Delta T_{NW} &= q''_{h,NW} \times \left(\frac{\Delta T_{h,NW}}{q''_{h,NW}} - \frac{\Delta T_{h,REF}}{q''_{h,REF}} \right) \\ \Delta V_{NW} &= q''_{h,NW} \times \left(\frac{V_{NW}}{q''_{h,NW}} - \frac{V_{REF}}{q''_{h,REF}} \right) \end{aligned} \tag{3.4}$$

here the subscript h stands for heater and 2ω is not shown for simplicity. V_{NW} is the total Seebeck Voltage measured for NW sample.

Thus we obtain the Seebeck coefficient of nanowire array by

$$S_{NW} = \Delta V_{NW} / \Delta T_{NW} \tag{3.5}$$

We can also calculate the nanowire/SOG composite thermal conductivity as $k_{comp} = q \times t_{NW} / (\Delta T_{NW} \times wL)$ where q is the power generation of

nanowire sample heater, t_{NW} is the length of nanowire, w is the width and L is the length of the heater. By applying effective medium theory, we further extract the thermal conductivity of nanowire as $[k_{comp}-(1-x)k_{SOG}]/x$ where k_{SOG} is the thermal conductivity of SOG and x is the nanowire area coverage. At room temperature SOG has thermal conductivity of $\sim$0.3 W/(m·K) [93, 94, 95] and this is also verified by our own measurement. For highly thermal conductive nanowire the SOG contribution in trivial however for nanowire with low thermal conductivity such as porous nanowire, accurate values of SOG thermal conductivity is required. We have obtained thermal conductivity of SOG (Filmtronics® 500F) from 15 K to 405 K using 3ω method and this will be discussed in detail in Chapter 5.

Key assumption in differential method is that heat conducts one dimensionally across all the layers under the heater and the substrate contribution remains the same in both NW and Ref samples with same energy density input. Thermal penetration depth $L_p = \sqrt{2\alpha/\omega}$ (α is the thermal diffusivity of the material and note that here ω is angular frequency) represents the distance thermal wave travels in the heat oscillation period. We can see from Fig. 3.6 that at higher frequency (lager than 3000 Hz in this case) the signal from nanowire sample no longer change linearly with the logarithm of the heating current frequency, this is because now the heat wave no longer reaches substrate and hence differential method is not applicable at this frequency range. Similarly for highly diffusive media especially at low temperature, in low frequency range heat wave penetration depth can be larger than the sample thickness or the length of heater and thus differential method fails. Corrections in case of finite heating element were discussed in detail in Ref. [20]

The substrate thermal conductivity can be extracted using a simple slope method [91] as in Eq. 3.6 (when thermal wave diffusion length does not exceeds the heater length and substrate thickness) or by fitting the temperature response based on a thermal model considering the finite heater effect which was developed by J. Sadhu [20]. Seebeck coefficient of substrate can also be extracted by the slope method as $dV_{2\omega}/d\Delta T_{2\omega}$.

$$k_{sub} = \frac{P}{2\pi L}\left(\frac{d(\Delta T_{2\omega})}{d(ln(2\omega))}\right)^{-1} \tag{3.6}$$

here the $\Delta T_{2\omega}$ is the total temperature increase of the heater line.

One large limitation and error source for this 3ω based technique is metal heater resistance-temperature calibration especially at temperature below 30 K. We tried to make the heater R-T calibration consistent by annealing the heater inside the cryostat under vacuum at temperature higher than measurement upper limit and a pulse heating [96]. To better solve this problem, at each measurement temperature we measured the resistance of heater right after $V_{3\omega}$ and $V_{2\omega}$ signal acquisition, this real-time calibration would represent the actual heater response more accurately. For a full temperature measurement we fit the calibration curve by Bloch-Grüneisen relations as shown in Eq. 3.7

$$R(T) = R_0 + A\left(\frac{T}{\Theta_R}\right)^5 \int_0^{\Theta_R/T} \frac{x^5}{(e^x-1)(1-e^{-x})}dx \tag{3.7}$$

where R_0 is the residual resistance due to defect scattering, A is a constant which depends on the velocity of electrons at the Fermi surface, for Au in our experiment we use $A = 4.225$, Θ_R is Debye temperature. A typical Bloch-Grüneisen fitting of our experimental calibration is shown in Fig. 3.7. We see that for temperatures below 30 K, R-T curve is flat and the corresponding dR/dT changes rapidly and loose its sensitivity. Temperature rise calculated from Eq. 3.2 can be abnormally large and as a result the extracted thermal conductivity may have large error.

3.2.2 Error analysis in differential measurement

We measured all the frequency dependent voltage by SR830 lock-in amplifier and error from the instrument is negligible. In differential measurement, as described in previous section, thermal conductivity is calculated as in Eq.

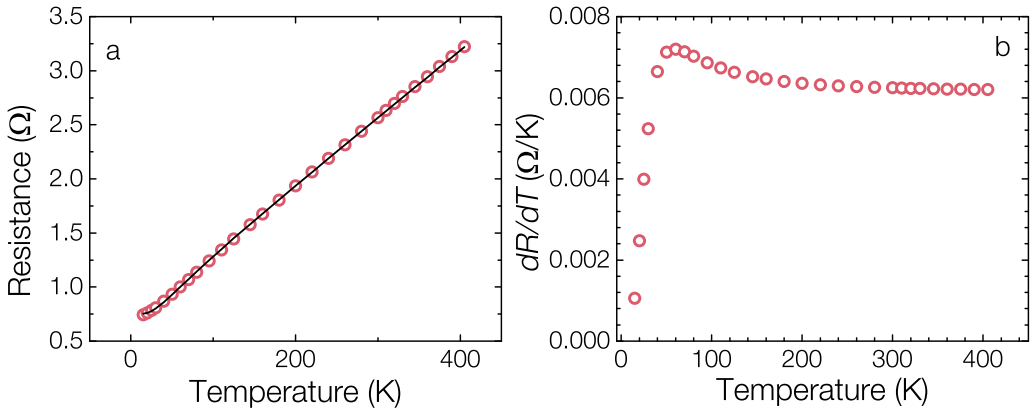

Figure 3.7: (a)Bloch-Grüneisen fitting of a calibration curve.(b)dR/dT extracted for each measurement temperature by fitted curve.

3.8.

$$\begin{aligned} k_{NW} &= \frac{k_{comp} - (1-x)k_{SOG}}{x} \\ &= \frac{t_{NW}q''/\Delta T_{NW} - (1-x)k_{SOG}}{x} \end{aligned} \tag{3.8}$$

There are tree major error sources: nanowire geometrical error i.e. wire effective conducting length t_{NW} and area coverage x; temperature drop normalized by power density $\Delta T_{NW}/q''$. The overall error in nanowire thermal conductivity can be expressed as Eq. 3.9

$$\frac{\delta k_{NW}}{k_{NW}} = \sqrt{\left(\frac{\delta(\Delta T_{NW}/q'')}{\Delta T_{NW}/q''}\right)^2 + \left(\frac{\delta(x)}{x}\right)^2 + \left(\frac{\delta(t_{NW})}{t_{NW}}\right)^2} \tag{3.9}$$

For length and area coverage, as discussed in [20], through extensive SEM study, uncertainty in area coverage $\delta(x)/x$ to be 20% and uncertainty in conducting length $\delta(t_{NW})/t_{NW}$ to be 10% at different locations would be reasonable.For simplicity we use $\Delta\widetilde{T} = \Delta T/q''$ and the uncertainty in normalized temperature drop is

$$\frac{\delta(\Delta\widetilde{T}_{NW})}{\Delta\widetilde{T}_{NW}} = \sqrt{\left[\left(\frac{\Delta\widetilde{T}_{h,NW}}{\Delta\widetilde{T}_{NW}}\right)\left(\frac{\delta\alpha}{\alpha}\right)_{h,NW}\right]^2 + \left[\left(\frac{\Delta\widetilde{T}_{h,REF}}{\Delta\widetilde{T}_{NW}}\right)\left(\frac{\delta\alpha}{\alpha}\right)_{h,REF}\right]^2} \tag{3.10}$$

where $\alpha = dR/dT$. We assume both Nanowire sample heater and reference sample heater calibration should have similar uncertainty and the value is taken to be about 5% [97].

The uncertainty in Seebeck coefficient measured by differential measurement mainly comes from the temperature measurement, as a result

$$\frac{\delta(S_{NW})}{S_{NW}} \cong \frac{\delta(\Delta\widetilde{T}_{NW})}{\Delta\widetilde{T}_{NW}} \tag{3.11}$$

3.2.3 Seebeck measurement platform fabrication

Here in this section we briefly described the Seebeck measurement platform fabrication procedures after the post-doping process is finished. The first and crucial step here is SOG (spin-on glass) fill of nanowire array. We were using SOG 500F manufactured by Filmtronics®. SOG was stored in refrigerator since it degraded quickly in ambient temperature (1 month shelf life compared with 6 months at 4 °C in refrigerator). However it should be acclimated at room temperature for 24 hours before applied. We first dehydrated the nanowire sample at 110 °C hot plate for 1∼2 minutes and then applied several drops of SOG onto nanowire. In order to obtained relatively uniform filling, we did 3-step spinning: first 5 sec at 500 rpm, then 10 sec at 1000 rpm and a finally at 5000 rpm for 20 sec. The spin rate can be adjusted based on the nanowire length. We then bake the filled sample sequentially on 80 °C, 110 °C and 270 °C hot plate for 1 min each. Then the sample was cured in furnace tube at 350 °C (or 425 °C suggested by the company) in N_2 atmosphere. We then etched SOG to the top of nanowire by Freon RIE. The overfileed length was characterized by cross section SEM. The etching recipe was 30 sccm CF_4, throttle pressure 35 mTorr and 100 W power. We calibrated the etching rate bo be about 55 nm/sec. Both CF_4 and CHF_3 etched SOG, however during etching CHF_3 deposited more polymer [98, 96] and contaminated the sample and as a result CF_4 was the primary choice. Silicon nanowire array with SOG overfilled and tip exposed are both shown in Fig. 3.8.

After SOG fill, we deposited the first electrical insulation layer which was 55 nm PECVD nitride and ∼260 nm PECVD oxide for Seebeck contact pads. The purpose of bilayer insulation was to avoid through pin holes. The insulation layer was first patterned using the heater mask and etched by CF_4 for 11 min to a depth of about 220 nm. Then the Seebeck contact pads were defined by 2nd lithography and we exposed about 150∼200 nm NW tip by another 6 min Freon RIE etching (3 min for the remaining oxide/nitride and 3 min for SOG). By applying this 2-step patterning, we can avoid contamination from photoresist, which was very crucial to form good electrical contact and key to the success of the measurement. We deposited about 220 nm Ni and 80 nm Au as contact metal. Nickel was widely used as contact metal to silicon nanowires based on many previous studies [99] and Au here was to protect the Ni surface from being oxidized as well as beneficial to wire bonding. Palladium was also tested however its adhesion to gold wire was not strong. The metal contact was later annealed to form silicide. We did rapid thermal anneal (RTA) at 320 °C for 3∼5 min and tuned this recipe based on others study [99, 100, 101].

We then deposited ∼ 55 nm PECVD nitride and ∼ 250 nm PECVD oxide as 2nd electrical insulation layer for metal heater. It would be better to deposit insulation layer for reference sample at the same time to avoid the inconsistence of PECVD systems. A 150 nm thick gold heater with 30 µm in width and 600 µm in length was deposited right above the portion of Seebeck voltage pad which was in contact with nanowire. Finally we expose the contact pads by etching for about 13∼15 min in Freon RIE. We over-etched for about 1∼2 min for a clean gold surface since CF_4 etched gold slowly [102], however too long over-etching may introduce polymer contamination [103] and should be taken into consideration. Finally we packaged the sample to a chip holder by wire bonding and mounted it into cryostat for measurement.

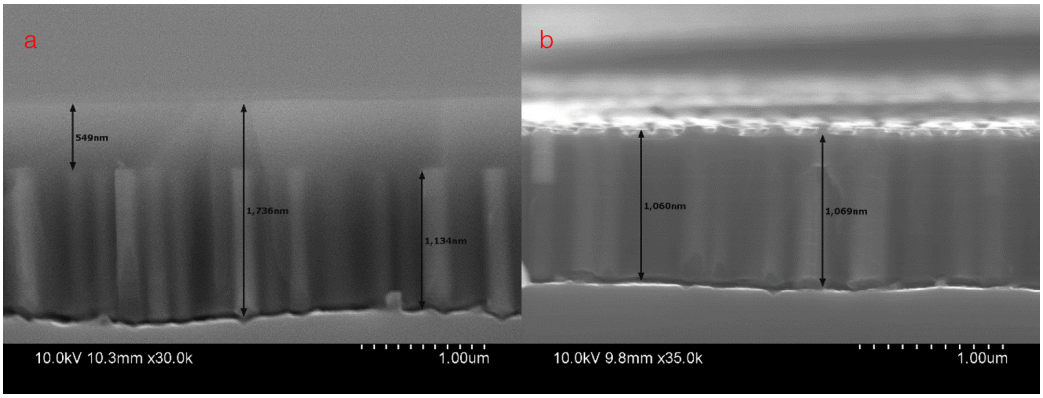

Figure 3.8: (a) Silicon nanowire array with about 549 nm SOG overfilled. (2) After Freon RIE etching, roughly 100 nm tips are exposed.

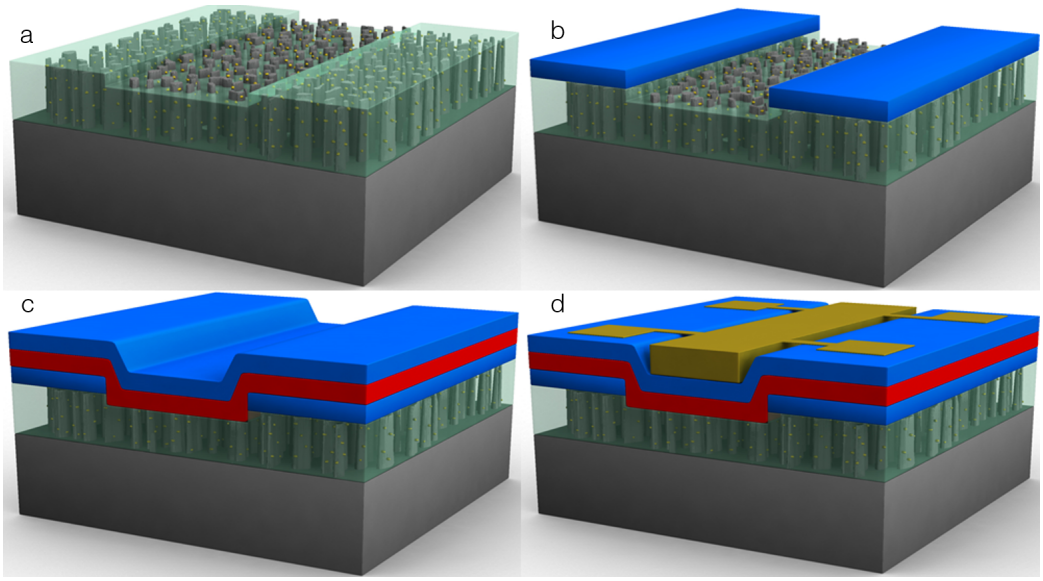

Figure 3.9: Illustration of Seebeck measurement platform fabrication steps.(a)Nanowire array was filled with SOG and etched to the nanowire top. (b) first insulation layer was deposited and patterned. After exposing about 150 nm NW tip, contact metal was ready to be deposited. (c)contact pad and 2nd insulation layer are deposited. (d) Metal heater is deposited.

3.3 Nanowire electrical conductivity measurement

3.3.1 Two-point probe electrical measurement on nanowire array

To begin with, we studied the electrical conductance of a silicon nanowire array by two-point probe (2pp) measurement between isolated top contacts. In order to make metal contact to the nanowire, we first filled the silicon nanowire sample with spin-on-glass (SOG) and then etched the overfilled SOG by Freon RIE till we exposed 150∼200 nm nanowire tip. The detailed procedure was discussed in Section 3.2.3. Based on the same consideration, we avoided using photoresist to do the contact pads patterning, instead a shadow mask was directly used. The contact metals were Ni and Au. After annealing the contact, we conducted two-point probe I-V test by probe station.

3.3.2 Four-point probe electrical measurement of single wire

Electrical resistivity of nanowire can be bettered estimated from four-point probe measurement on single silicon nanowire. We tried to do transmission line measurement (TLM) [104, 105] on silicon nanowire array by varying the contact pad size and distance, however the resistance values showed no clear relation with either the distance between pads or the size of the pads. This may be attributed to large contact resistances.

We first scraped the silicon nanowire from the substrate with a razor blade and then sonicated in IPA to make a nanowire suspension. Then we dispersed nanowires onto a cleaned silicon substrate. The substrate was covered with 300 nm PECVD nitride or thermal oxide and Au landmarks used to locate the silicon nanowire were patterned by E-beam lithography. Silicon nanowires adhered to the substrate very well via Van de Waals forces and could not be removed by an IPA wash or N_2 gun. We searched for nanowires under an SEM and took an image of a wire together with two landmarks, by mapping this SEM image to the original pattern file which was used to define the

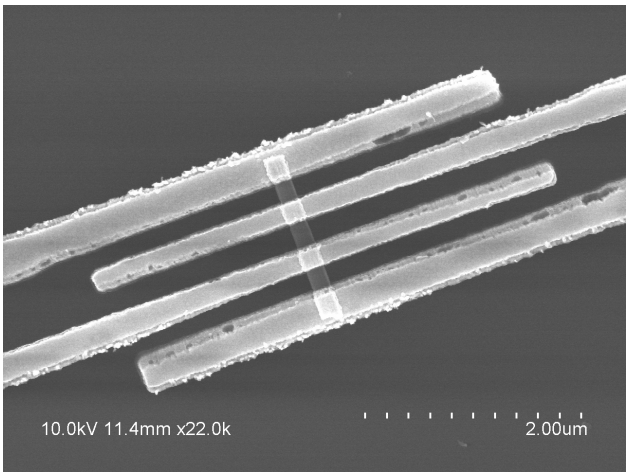

Figure 3.10: SEM image of a single wire electrical conductivity measurement platfrom

landmarks, we managed to locate the nanowire. Before E-beam lithography, we passivated the nanowire surface with ∼20 nm PECVD oxide. The passivation is critical for two reasons: first, surface passivation can reduce the interface trapped states density which we will discuss shortly [106]; second, this thin oxide layer protect the nanowire surface from being contaminated by PMMA. We then defined the four electrodes by another E-beam lithography. Before metallization, we cleaned the contact area by O_2 Plasma and then etched away the passivation layer and native oxide. The metal contact pads were 130 nm Ni and 20 nm Au. The contact pads were annealed under the condition discussed in Section 3.3.1. A SEM image of four-point probe platform and representative I-V curve when ohmic contact was achieved are shown in Fig. 3.10.

With resistance extracted from the I-V curve and the dimensions of the nanowire, we can calculate the resistivity of the nanowire. However due to the surface depletion effect [106, 107] the radius which contributes to the charge transport r_{elec} may be different from the physical radius of the nanowire r_{phys}. Trapped charges at or near the vicinity of Si to SiO_2 interface can attract the charges from the nanowire and forms depletion region near the surface [106, 107]. The density of trapped states is characterized by interface trap level density D_{it} (eV^{-1} cm^{-2}). Figure 3.11 (adopted from Ref. [20, 108]) demonstrated that r_{elec} depends on the doping concentration and original

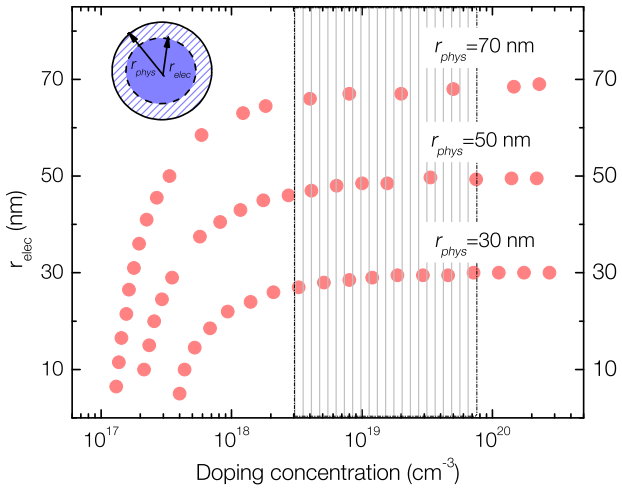

Figure 3.11: Surface depletion model for silicon NWs showing the radius of undepleted region (r_{elec}) in comparison to their physical radius (r_{phys}) against dopant concentration. The shaded region indicates the NW doping range studied in this paper. Image is adopted from [20, 108]

r_{phys}, following the Eq. 3.12 from [107, 109]

$$r_{elec} = \sqrt{{r_{phys}}^2 + \frac{2r_{phys}Q_f - 2r_{phys}e^2D_{it}\psi_0}{e(N_D - N_A)\left(1 + \frac{r_{phys}e^2}{2\varepsilon_0\varepsilon_s}D_{it}\right)}} \tag{3.12}$$

Another big error source is the estimation of the cross sectional area. As we can see from Fig. 3.1, the cross section of nanowire formed is more like celery instead of regular shape, this is because dewetting is a random process. In order to get a better estimation of the actual cross-sectional area, we cut the measured wire using a Focused Ion Beam (FIB) and calculated the actual cross section area based on the image, this is demonstrated in Fig. 3.12.

3.4 Raman characterization

Raman spectroscopy is a powerful technique in studying the free carriers of doped bulk silicon [110, 111, 112, 113, 114, 115, 116]. In doped silicon, the long wavelength optical vibration can cause a dynamic carrier redistribution among energy bands [110], the effect is equivalent to a softening of the lattice and is translated into a red-shift in Raman spectrum [110]. For boron

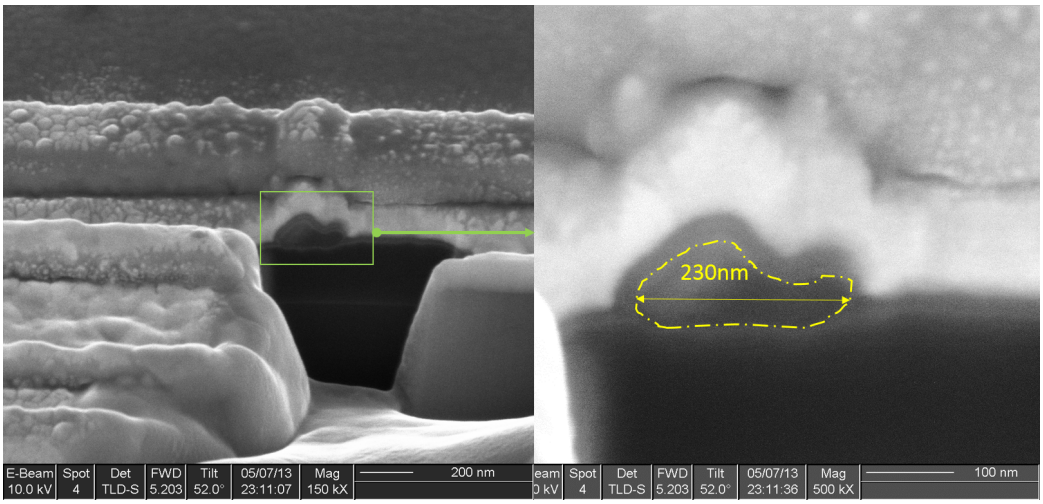

Figure 3.12: FIB cut cross section of a nanowire on which four-point probe electrical measurement was performed. The actual area is marked with the yellow dash line. The "diameter" of this wire would be 230 nm if only analyzing from top view SEM.

doped silicon, redistribution of holes within and between light and heavy-hole bands strongly affects the Raman frequency [110]. Moreover Fano-type [117] interaction between the discrete one-phonon scattering and a continuum of electronic scattering results in an asymmetric broadening of Raman spectrum especially in p-type silicon [111]. People have successfully demonstrated doping concentration characterization by Raman spectroscopy in bulk silicon [118, 119, 120] as well as silicon nanowire [121, 122, 123].

Researchers also attempted to characterize porous silicon by Raman spectroscopy [124, 125, 126, 127, 128, 129, 130, 131, 132, 133]. The results were quite diverse, this may be due to the difference in fabrication conditions such as doping level, morphologies such as crystalline size and porosity and different measurement conditions. In an early study, Goodes et al. [124] interpreted the spectrum of their porous silicon by the effect of phonon with short coherent length, however this was later pointed out by Münder et al. [125] that the spectra were mainly due to heating effect. Through detailed study, they explained the porous silicon Raman spectra by phonon confinement or localization in nanocrystal [134, 135] and extracted their size information. This approach was adapted by following researchers [126, 128, 129, 130, 131, 132, 133] in the interpretation of porous silicon

Raman spectra. Phonon confinement induced Raman peak red-shift and broadening were also observed in ultra-thin silicon nanowires [136, 137, 138]. At the same time, local heating by laser also exhibited the same effect in silicon nanowire Raman spectrum [139, 140, 141, 142]. Hence we should carefully choose the laser power to avoid the heating effect when extracting the crystalline size information by Raman spectroscopy.

3.4.1 Raman spectroscopy basics

The system we were using was NanoPhoton Laser Raman-11, two wavelengths excitation laser are available: 532 nm and 785 nm. The system can only measure Stokes spectrum. Three gratings are installed which are 2400 gr/mm (not available for 785 nm excitation laser), 1200 gr/mm and 600 gr/mm; the highest resolution is 1.5 cm^{-1} for 532 nm with 2400 gr/mm grating and 1.2 cm^{-1} for 785 nm with 1200 gr/mm grating. The samples were measured in a backscattering configuration, and polarization of the excitation light and the collected scattered light were parallel to each other. We applied a line focus and x-y imaging to reduce the spectrum noise [143] which is illustrated in Fig. 3.13.

The observed Raman peak is the convolution of a Lorentzian shape of the actual photon with the response function of the spectrometer [144]. Though the actual shape of this function should be triangular, we often consider the response function as a Gaussian and the convolution results are almost identical [144]. The convolution product of a Lorentzian and a Gaussian is a Voigt profile [144]. To rigorously study the materials intrinsic FWHM, one needs a deconvolution of the measured spectrum.

We measured the Raman spectrum of a low-doped p-type bulk silicon piece ($10 \sim 20\ \Omega\cdot$ cm) with the same instrument settings used for nanowire characterization (532 nm, 60 µm confocal size, incident laser power is 0.1 mW and exposure time is 60 sec) to study the effect of instrument broadening. We fitted the measured spectrum by both Voigt and Lorentzian profile as shown in Fig. 3.14 and the fitting parameters are listed in Table 3.1. Both fittings agrees fairly well with the experimental data except that Lorentzian

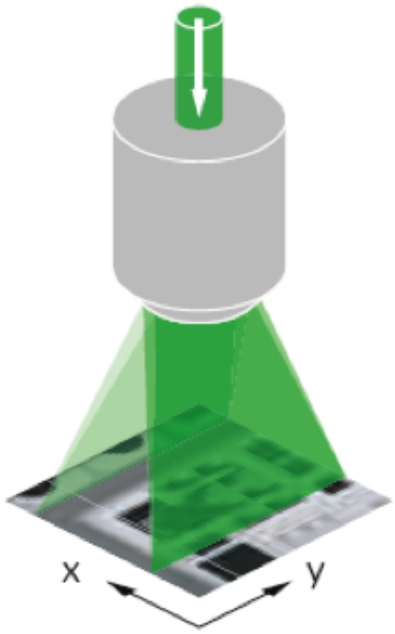

Figure 3.13: The sample are scanned with x-y imaging, laser intensity is uniformly distributed along the line-shaped Raman scattering light. Image is adopted from the product datasheet.

Table 3.1: Fitting Parameters of Voigt fitting and Lorentzian fitting of experimental spectrum of a low doped p-type (10∼20 Ω·cm) bulk silicon.

Fitting Profile	**FWHM** ($\mathbf{cm^{-1}}$)	**Peak Position** ($\mathbf{cm^{-1}}$)	**Adjusted** R^2
Voigt Fitting	3.5763	521.73947	0.9995
Lorentzian Fitting	3.38975	521.73922	0.99778

overestimates the peak portion and hence gives smaller FWHM.

The width of the response function of the spectrometer can be determined by measuring the laser spectrum width of the built-in Neon reference with the same confocal slit size (60 µm) [144]. At 532 nm incident wavelength, the excited laser spectrum has a width of about 0.05 nm or 1.7 cm^{-1} equivalently. We can adopt a simplified procedure to do the deconvolution by using Posener's table [144, 145]. For measured FWHM ∼3.5763 cm^{-1} and instrument response function width $\Delta\nu_G \sim 1.7$ cm^{-1} which was determined by measuring the Neon spectrum width, the natural photon FWHM of the measured silicon at room temperature is ∼2.65 cm^{-1} ,which agrees very well with the litera-

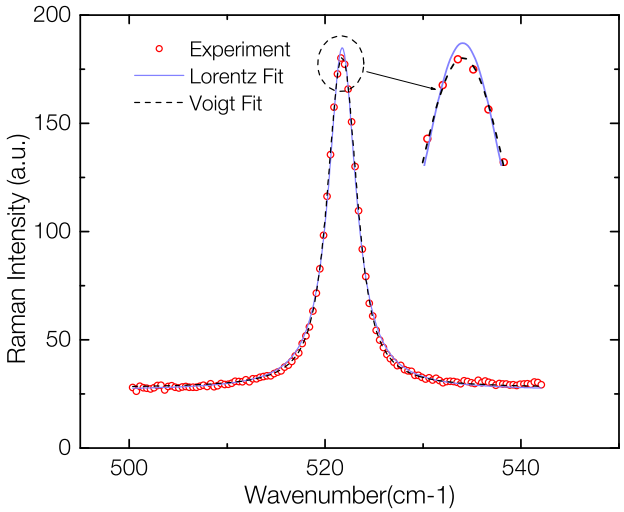

Figure 3.14: Voigt fitting and Lorentzian fitting of experimental spectrum of a low doped p-type (10∼20 Ω·cm) bulk silicon.

ture value [144]. The measured effective FWHM $\Delta\nu_{eff}$ can also be roughly approximated by [145] $\Delta\nu_{eff} \sim (ln2)^{-1/2}\Delta\nu_G\left(1+\left(\frac{\Delta\nu_L}{(ln2)^{-1/2}\Delta\nu_G}\right)^2\right)^{1/2}$ and as a result, when $\Delta\nu_L >> (ln2)^{-1/2}\Delta\nu_G = 2.04$ cm^{-1}, $\Delta\nu_{eff} \sim \Delta\nu_L$.

For heavily-doped silicon, the discrete one-phonon scattering and a continuum of electronic scattering results in an asymmetric broadening of Raman spectrum which is Fano-line [117] especially in p-type silicon [111]. We will discuss this effect in detail in the following section. Considering the system broadening, the actual spectrum is a convolution of a Gaussian and Fano-line. The most accurate fitting of the experimental spectrum can be obtained by the convoluted distribution [146, 119]. However this process is complicated and computational costly. Instead, when discussing the spectrum broadening due to free carriers, most literature [111, 112, 113, 116] directly fitted the experimental data with standard Fano equation. From Ref. [119] we see that for instrument broadening of 2.5 cm^{-1}, the difference between deconvoluted width ($\Gamma = 2\Gamma_p$) and width without correction is less than 1 cm^{-1}. The difference would be smaller in our case due to less instrument broadening (1.7 cm^{-1}) and Fano line shape fits our highly doped bulk spectrum quite well.

As a result, later when analyzing the size, carrier concentration and im-

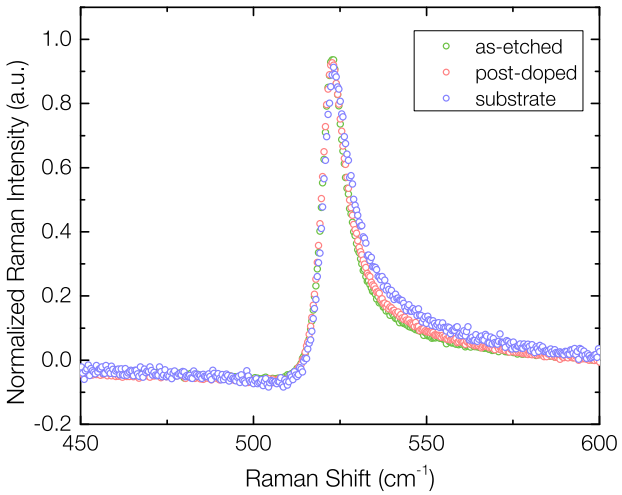

Figure 3.15: Normalized 785nm Raman spectrum of as-etched porous nanowire, post-doped porous nanowire and the substrate from which the nanowires were fabricated. The three spectrum overlapped with each other, this is an indication that all the signal are collected from the substrate

purity effects, we fitted the spectrum with a modified Lorentzian and the instrument response function is not included in the expression, similar approaches were applied in most of the previous studies [134, 135, 147, 137] , however its effect should be kept in mind.

As of the choice of laser wavelength, 532 nm incident light will cause resonant excitation, which means most of the signal are from the nanowire layer; when using 785 nm incident laser, we were actually collecting most of the signal from substrate, this is clearly illustrated in when we normalize the as-etched, post-doped and substrate spectrum as shown in Fig. 3.15.

We also carefully chose the laser power to be as low as possible to avoid heating effect. A previous study [139] showed that peak asymmetric broadening as well as red-shift reported for silicon nanowire Raman spectrum were actually due to laser local heating instead of size induced phonon confinement. As-etched nanowire Raman spectrum were measured under different incident power to study the heating effect. We started from the lowest laser power and gradually increased the power, meanwhile the peak position and FWHM were measured as shown in Table 3.2. We see that the peak shift is more sensitive to the laser power. However at power < 0.05 mW, Ra-

Table 3.2: As-etched nanowire sample measured with different incident laser power, from the table we can see that for power below 0.1 mW, the heating effect on FWHM can be neglected.

Laser Power (mW)	**Peak Position (cm^{-1})**	**FWHM (cm^{-1})**
0.002	520.41	5.53
0.005	520.43	5.57
0.010	520.55	5.63
0.020	520.28	5.50
0.030	520.27	5.47
0.040	520.24	5.50
0.050	520.16	5.52
0.101	520.01	5.58
0.204	519.72	5.77
0.312	519.57	5.81
0.525	519.15	5.89

man spectrum has large noise and fitting error is large. We also see that when incident power is below 0.1 mW, the heating effect on FWHM can be neglected; if we further increase the power, significant heating effect started contributing to the spectrum. Since weve measured that both as-etched and post-doped silicon nanowire have very similar thermal conductivity ($\sim$2 W/(m·K) at room temperature), the laser heating should be similar for post-doped nanowire. At the same time, higher power means better signal-to-noise ratio and as a result we kept incident laser power to be $\sim$0.1 mW for the nanowire samples. The corresponding temperature rise under this excitation laser power is less than 10 K by Eq. 3.13 and we will discuss this shortly.

3.4.2 Parameters that cause peak shift and width broadening of Raman spectrum

Raman peak shift and broadening can be affected by many parameters, for example temperature [139, 148, 141, 142], strain [149, 150], impurity, free

carrier [111, 113, 116, 110], crystalline size induced phonon confinement [134, 135, 147, 137] and etc. We will discuss their effects quantitatively and try to explain the porous NW spectrum.

1. Temperature Effect

Local heating can cause peak red-shift and broadening [139]. By fitting the experimental data, empirical relations Eq. 3.13 describes the heating effect on peak shift and FWHM Γ [148, 141, 142]

$$\begin{aligned} \frac{d\omega}{dT} &= 0.022 \pm 0.001 \text{ cm}^{-1} \cdot \text{K}^{-1} \\ \frac{d\Gamma}{dT} &= 0.0102 \text{ cm}^{-1} \cdot \text{K}^{-1} \end{aligned} \tag{3.13}$$

As we discussed before, Raman spectrum peak shift is more sensitive to temperature change. For $\Delta T < 10$ K, FWHM broadening due to heating effect is less than 0.1 cm^{-1}.

2. Strain Effect

Uniaxial stress can cause the Raman peak to split due to the breaking of optical phonon degeneracy and shift linearly with the applied stress [149]. A negative compressive stress along [100] direction will result in blue-shift (towards the high wave number) and positive tensile stress leads to a red-shift of the Raman peak which is estimated to be [150].

$$\frac{d\omega}{dT} \sim -0.004 \text{ cm}^{-1}/\text{MPa} \tag{3.14}$$

Strain effect on spectrum FWHM Γ is not well documented. According to Ref. [149], static uniaxial stress does not affect FWHM. However, Kunz et al. [119] stated that the peak splitting cannot be individually resolved and thus both peak shift and broadening will occur. No quantitative evaluation was provided.

3. Impurity Effect

In doped silicon, impurity i.e. dopant atoms affect the phonon frequency through a change in the average atomic mass and change in average atomic volume which affects the phonon frequency via Grüneisen parameter [110]. Impurities induced frequency shift can be approximated by

$$\frac{\delta\omega_0}{\omega_0} \sim \frac{1}{1000}\left(\frac{1}{2}a_M + 3\gamma a_V\right)\left(n \times 10^{-19} \times Q\right) \tag{3.15}$$

Where $\delta\omega_0$ is the frequency shift, ω_0 is the optical phonon frequency or Raman peak shift when no impurity exists,a_M and a_V is the fractional change in average mass and volume due to the impurity respectively, for boron doped silicon, $a_M = 0.64$ and $a_V = 0.2$; γ is Grüneisen parameter and is approximately to be 1, n is the doping concentration and constant $Q = 0.2$ for silicon. Then dependence of peak width on impurity was not reported because in most of the cases it is coupled with free carrier effect. Impurity effect does not depend on temperature.

4. Free Carrier Effect

In doped silicon, the long wavelength optical vibration can cause a dynamic carrier redistribution among energy bands [110], the effect is equivalent to a softening of the lattice and is translated into a red-shift in Raman spectrum. For boron doped silicon, redistribution of holes within and between light and heavy-hole bands strongly affects the Raman frequency [110]. Moreover Fano-type [117] interaction between the discrete one-phonon scattering and a continuum of electronic scattering results in an asymmetric broadening of Raman spectrum especially in p-type silicon [111].

The Fano line-shape is given by

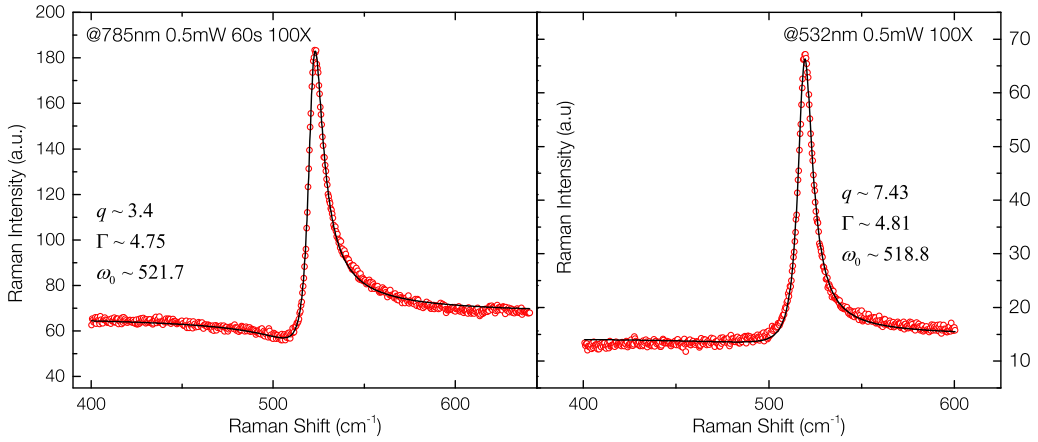

Figure 3.16: Raman spectrum of highly boron doped silicon ($\sim 3 \times 10^{19}$ cm^{-3}) at 785 nm and 532 nm excitation wavelength respectively, spectrum is fitted by Fano line-shape.

$$I(\omega) = A\frac{(q_p + \epsilon)^2}{1+\epsilon}$$
$$\epsilon = \frac{\omega - (\omega_p + \delta\omega_p)}{\Gamma_p} \tag{3.16}$$

where q_p is asymmetric factor, smaller q_p indicates more asymmetric; ω_p is the optical phonon frequency in intrinsic silicon, $\omega_p + \delta\omega_p$ is the phonon frequency in doped silicon, Γ_p is the linewidth factor. Peak position of the Fano-shape line is given by

$$\omega_M = \omega_p + \delta\omega_p + \frac{\Gamma_p}{q_p} \tag{3.17}$$

This can be obtained by taking $dI(\omega)/d\epsilon = 0$.

We can fit the bulk Raman spectrum by Fano very well as is shown in Fig. 3.16 and the fitted parameter agrees well with the literature value [116] shown in Table 3.3.

From Table 3.3 we can tell that: (1) the asymmetric factor q_p strongly depends on exciting wavelength, longer excitation wavelength cause stronger Fano interaction, this is also demonstrated in our measurement Fig. 3.16; (2) width parameter Γ_p and shifted peak $\omega_p + \delta\omega_p$ do not depend on the excitation

Table 3.3: Fano parameters of the optical phonon in p-type silicon at different doping. Adopted from Table 1 of Ref. [116].

Carrier Concentration (cm^{-3})	**Exciting Wavelength (Å)**	**Optical Phonon**		
		q_p	Γ_p **(cm^{-1})**	$\omega_p + \Delta\omega_p$ **(cm^{-1})**
4×10^{20}	4579	4.54	12.4 ± 0.5	512 ± 2
	5145	2.57	11.8 ± 0.5	511 ± 2
	6471	0.55	12.6 ± 0.5	509 ± 2
			average	average
			12.3 ± 0.5	510.7 ± 1.5
1.5×10^{20}	4880	6.0	9.2	516.7
	6471	1.8	8.5	514.8
			average	average
			8.85 ± 0.5	515.7
6×10^{19}	4880	10	6.2	519.7
1.5×10^{19}	4880	44	3.1	520.2
	6471	20	2.65	520.2
			average	average
			2.88	520.2
5×10^{18}	4880	200	1.8	520
Pure Silicon (10^{13})			1.5	520

frequency at a given carrier concentration; (3) with increasing carrier concentration, Raman spectrum becomes more asymmetric (smaller q_p), wider (larger Γ_p) and the peak red-shift (towards lower wave number) due to free carrier is increased.

Now lets briefly discuss the Fano width parameter Γ_p. Since Fano line-shape is asymmetric and has a local minimum (at $\omega_p + \delta\omega_p - \Gamma q$), we could not define a FWHM as in the the Lorentzian or Voigt shape. In Fano's original paper [117], $\Gamma = 2\Gamma_p$ indicates the spectral width. When $q \to \infty$ in intrinsic silicon, Fano line-shape approaches Lorentzian, and $2\Gamma_p$ should be the FWHM of intrinsic silicon which is 3.0 cm^{-1} as shown in Table 3.3. We have to keep in mind that in Table 3.3, the Fano fitting is for experimental spectrum and hence instrument broadening is included.

5. Crystalline Size Effect

When nano-crystalline with critical dimension less than 30 nm exists, the phonon is confined or localized in the nano-crystalline volume [134] and results in a relaxation of the $k = 0$ selection rule (k is the optical phonon wave vector), which means additional $k \neq 0$ transition is also contributing to the Raman spectrum. This relaxation will lead to peak broadening and red-shift. To describe this phonon confinement, the wave function for a phonon in an infinite crystal is multiplied by a Gaussian weighted function. There is no physical reason to assume this form of confinement or its particular value at the crystalline boundary [135]. The first-order Raman spectrum is [134, 135]

$$I(\omega, R) \propto \int_0^{2\pi/a} \frac{|C(k)|^2 \, dk^3}{\left(\omega - \omega_0(k)\right)^2 + \left(\Gamma_0/2\right)^2} \tag{3.18}$$

where R is the critical dimension of the nano-crystalline, a is the lattice constant, $|C(k)|^2$ is the Fourier coefficient of the confined phonon wave function, Γ_0 is the phonon natural width convoluted with the instrument broadening [137] or the FWHM of the spectrum, ω is wave number and $\omega_0(k)$ is the optical phonon dispersion curve. In most of the literatures, an isotropic optical

phonon dispersion of bulk silicon is used [137, 139]

$$\omega_0(k) = \sqrt{A + B\cos(ka/4)} \tag{3.19}$$

where $A = 1.714 \times 10^5$ cm^{-2} and $B = 1.0 \times 10^5$ cm^{-2} were determined from neutron scattering data for the TO branch [137, 151, 152].

For the Fourier coefficient $|C(k)|^2$ is usually taken in the form of [135]

$$|C(k)|^2 = \exp\left(-\frac{k^2R^2}{2\beta^2}\right) \tag{3.20}$$

where β is a factor representing the phonon confinement. A wide range of $1.4 < \beta < 10.4$ has been reported in the literature for silicon nano structure and according to Ref. [137, 138], β should be determined from the experiment with known crystalline dimension. $\beta = 2\sqrt{2}\pi$ is the mostly used value.

We can also assume the crystalline size has a Gaussian distribution

$$\varphi(R) = \frac{1}{\sqrt{2\pi\sigma^2}}\exp\left(-\frac{1}{2}\frac{(R-R_0)^2}{\sigma^2}\right) \tag{3.21}$$

And the first-order Raman spectrum is modified as [129]

$$\begin{aligned} I(\omega, R) &\propto \int_0^{2\pi/a} |C(k)|^2 \frac{dk^3}{(\omega - \omega_0(k))^2 + (\Gamma_0/2)^2} \\ &= \int_0^{2\pi/a} f(k) exp\left(-\frac{f(k)^2 {R_0}^2 k^2}{2\beta^2}\right) \frac{dk^3}{(\omega - \omega_0(k))^2 + (\Gamma_0/2)^2} \end{aligned} \tag{3.22}$$

where

$$f(k) = \left[1 + (\sigma k)^2/\beta^2\right]^{-1/2} \tag{3.23}$$

If we further consider the Fano interaction, then the Raman spectrum may be modified as in Eq. 3.24 similar approaches were used in Ref. [153]

$$I(\omega, R) \propto \int_0^{2\pi/a} dk^3 \frac{|C(k)|^2[\Gamma_0 q_p/2 + \omega - \omega_0(k)]^2}{(\omega - \omega_0(k))^2 + (\Gamma_0/2)^2} \tag{3.24}$$

3.4.3 General steps for Raman spectrum analysis

Since we are collecting Raman signal from a layer of $\sim 1\,\mu m$ nanowire, we should accurately focus on top of the sample. A 100X objective would be beneficial due to its small depth of focus. And better focus is achieved by checking laser spot in NanoPhoton Laser Raman-11 system. By comparing the Raman spectrum we noticed that a polarizer is not necessary. Considering the system error due to spectrometer or grating drifting, we should finish all the measurement in one operation session. Carefully calibration with standard Neon spectrum before measuring the sample is also a choice. To get a better signal-to-noise ratio, it would be better to use line scanning and the exposure time can be adjusted, currently we were using 60 sec.

In order to extract the size or doping information from Raman spectrum analysis, we have to consider all the possible factors that cause peak shift or broadening. We have discussed this in detail in Sectiion 3.4.2. Specifically, when analyzing the Raman spectrum of porous nanowire to extract the carrier concentration information, instead of peak shift and asymmetric factor q_p, we mainly use spectrum width as the evaluation parameter by comparing it with the literature values listed in Table 3.3. This is because: peak shift is also sensitive to heating, strain, and at the same time system drift also introduces large error in the peak position; asymmetric factor q_p strongly depends on the excitation wavelength. However the spectrum width cannot be directly obtained by fitting with Voigt function. As we will see in Section 4.2, we have to separate the size induced phonon confinement and free carrier effect. Key assumption is that all the effects mentioned above on spectrum width are independent, similar approaches were used by Becker et al. [118] and Kunz et al. [119] . In other words, we assume an imaginary identical solid nanowire system of same free carrier concentration has a *natural* FWHM Γ_0, and then randomly distributed pores further broaden the spectrum to its total width Γ. By fitting the spectrum with Eq. 3.18 or 3.22. we then extract Γ_0 of this imaginary nanowire system which has purely free carrier contribution. By comparing this with the literature value, we would estimate the carrier concentrations. We could also fit the spectrum with Eq. 3.24, however we found that our Raman spectra do not have significant

asymmetry and thus this approach would not improve the fitting accuracy, the possible reason is that the Fano effect is suppressed in porous silicon. We will discuss the analysis of as-etched and post-doped porous nanowire in detail in Section 4.2.

CHAPTER 4

ELECTRON TRANSPORT PROPERTIES IN POROUS SILICON NANOWIRE

In this chapter, we will discuss the electrical transport properties i.e. electrical conductivity and Seebeck coefficient in porous silicon nanowire under different doping conditions. By *I-V* test, Raman spectroscopy and Seebeck coefficient analysis we obtain electrical transport information such as carrier concentration, mobility and the scattering process, although not complete. Experimental technique and data analysis was discussed in detail in Chapter 3.

4.1 Electrical conductance of porous silicon nanowire at different doping conditions

4.1.1 Two-point probe conductance measurement

We did two-point probe *I-V* test on as-etched porous silicon nanowire array as well as post-doped silicon nanowire array. As mentioned above, we have tested four pre-deposition temperatures range from 800∼ 950 °C with a 50 °C step. In the actual test, we used two batches of porous nanowire: the batch doped at 950 °C had length ∼700 nm while another batch with length 1.2∼1.5 µm was used to test the doping effect at 800 °C, 850 °C and 900 °C. Thus we are comparing the electrical conductance of the post-doped nanowires with their corresponding as-etched reference. The metal contact pads were separated by different distances. Since the substrate was highly conductive, the resistance of silicon nanowire and nanowire/metal contact should be dominate. This was verified in the experiment that the two-point probe *I-V* curves were independent of the distance between the contact pads.

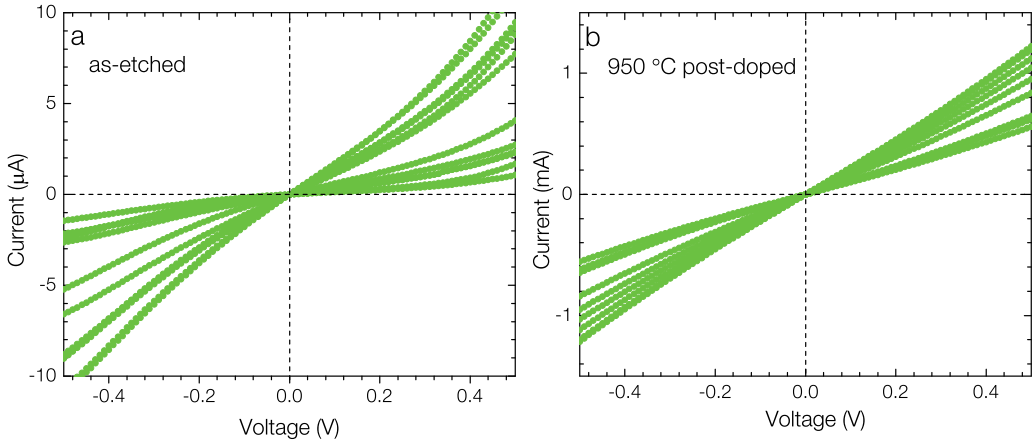

Figure 4.1: (a) Two-point probe I-V curve of as-doped silicon nanowire array. (b) Two-point probe I-V curve of porous silicon nanowire array doped at 950 °C.

We first discuss the electrical performance doped at 950 °C shown in Fig. 4.1.

After post-doping, the electrical conductance clearly showed a 2 to 3 orders increase for the sample doped at 950 °C compared with the as-etched sample. For samples doped at lower temperatures, the porous wires doped at 900 °C had a 1 order of magnitude increase in electrical conductance while the 850 °C and 800 °C doped samples did not show significant improvement. The possible reason is that although boron solubility in silicon at 800∼850 °C (between 5×10^{19} cm^{-3} and 8×10^{19} cm^{-3}) was higher than the initial substrate doping ($\sim 3 \times 10^{19}$ cm^{-3}), the extra dopant atoms introduced into the nanowire were not enough to result in significant change. The result here was inspiring, we successfully demonstrated that even for the degenerately doped porous silicon nanowire, we were able to enhance its electrical conductance. However we could not differentiate the nanowire contribution from the total resistance because of the contact resistance was unknown.

Now we estimate the bounds of electrical conductivity of post-doped nanowire from two-point probe measurement. When assuming all the resistances come from nanowire we get the upper limit of electrical resistivity. Contact pad area of nanowire doped at 950 °C was $210 \times 210 \times 0.25$ μm^2 and conducting length was about 500 nm; for nanowires post doped at other temperatures, the contact pad area was about $600 \times 30 \times 0.35$ μm^2 and conducting length

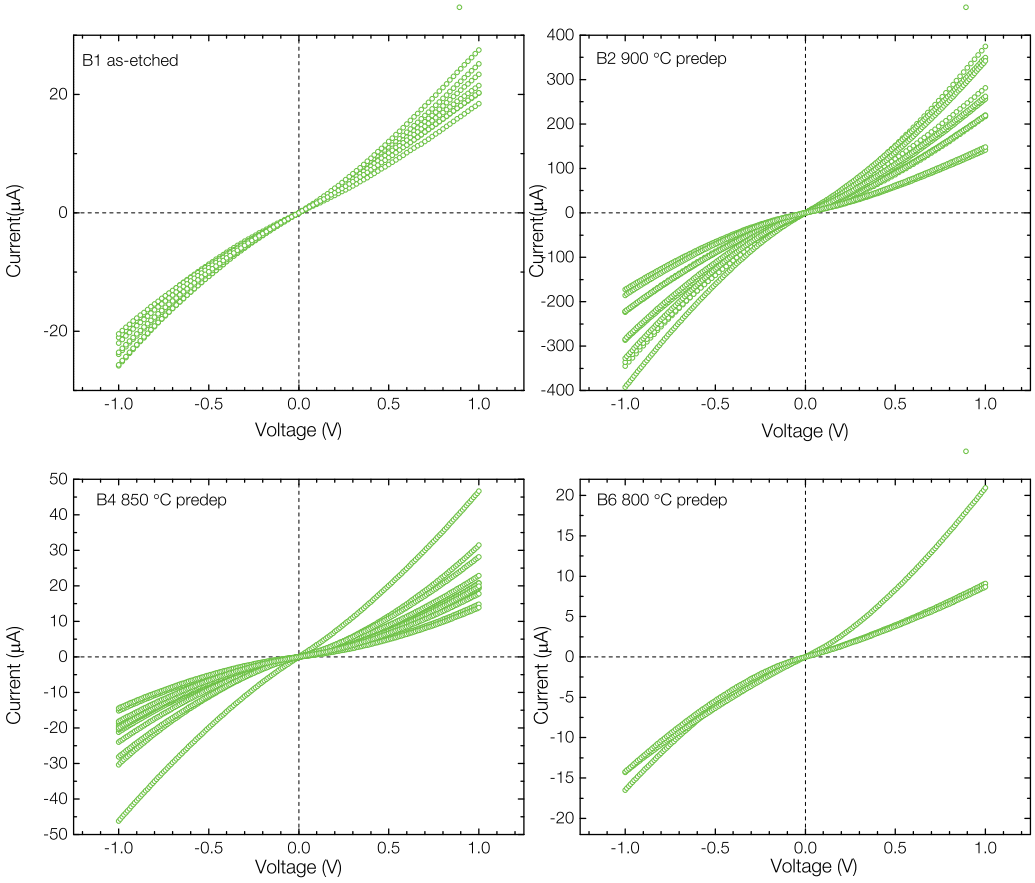

Figure 4.2: Two-point probe I-V curve of as-etched porous silicon nanowire array and nanowire doped at 800∼900 °C.

was about 1200 nm. Since the substrate was degenerately doped, its contribution to the overall resistance was negligible. For 950 °C post-doped nanowire, the upper limit of electrical resistivity would be on the order of $10 \sim 10^2$ Ω·cm and this was three orders of magnitude lower than the corresponding as-etched nanowire resistivity; for porous nanowire post-doped at 900 °C, the upper limit of electrical resistivity was $10 \sim 20$ Ω·cm compared with the corresponding as-etched resistivity which was $130 \sim 150$ Ω·cm. Contribution from contact is hard to characterize and no literature values have been reported for porous nanowire. We previously estimated the contact resistivity for smooth nanowires [29] and for low doped silicon nanowire, the contact resistivity can be up to 0.13 Ω·cm^2. Thus contact resistance can be up to 1.18 kΩ for one pad (950 °C doped sample) and it is possible the 2pp resistance was dominated by contact, i.e. resistivity of porous nanowire after post doping at 950 °C had more than 3 orders of magnitude reduction. Similar argument also applies for nanowire post doped at 900 °C.

4.1.2 Four-point probe single wire electrical conductivity measurement

In order to measure the exact electrical conductivity of the porous wire, we conducted four-point probe measurement on single porous silicon nanowire with longer length. The I-V curve of an as-etched single silicon nanowire is shown in Fig. 4.3. Based on the dimension of the measured wire, we extracted the electrical resistivity of as-etched porous wire was 7 orders of magnitude higher than the bulk value (10^{-3} Ω·cm) of same doping level ($\sim 3 \times 10^{19}$ cm^{-3}). We can also see from the inlet of Fig. 4.3 that the two-point probe I-V curve was quite similar to the four-point probe I-V curve, which indicated that in this case the dominant resistance was the wire instead of contact resistance.

We then performed four-point probe electrical measurement on a single post-doped porous wire. However the wire length in the previous mentioned post-doping study was about 700 nm and 1.2∼1.5 µm which are suitable for Seebeck measurement. In order to properly locate and place four electrodes,

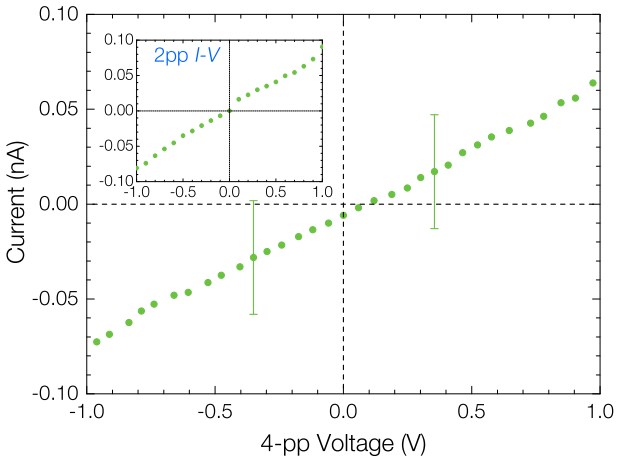

Figure 4.3: I-V measurement of a successful four-point probe measurement of as-etched single porous nanowire. Inlet shows the two-point probe I-V curve between two inner electrode.

we required wires longer wires. We fabricated another batch of porous silicon nanowire with length 1.8 µm and post doped it using the same recipe. The best chance would be the nanowire doped at 950 °C. Unfortunately, we did not get proper linear I-V curve. We investigate the possible reason by SIMS. Figure 4.4 shows the boron concentration of porous silicon nanowires we have tested. The 950 °C post doped porous wires of length ∼700 nm shows relatively uniform boron concentration level of $1 \sim 2 \times 10^{21}$ cm^{-3} while NW post doped at 900 °C has an average 1.4×10^{20} cm^{-3}; for the 1.8 µm long wire, only the first 1000 nm from the top were doped to 10^{21} cm^{-3} level and the remaining part of the wires have a doping profile gradually decreases to the starting doping level of 3×10^{19} cm^{-3}. As a reference, the boron concentration in as-etched sample is similar to the substrate. The nonuniform boron concentration in 1.8 µm nanowire indicates that the bottom of the wires were not well wetted by the SOD, moreover, different segments between the electrodes were at different doping level and low-doped portion would dominate. This may partly explain why we could not get good result. Another difficulty comes from the nanowire fabrication technique, porosity reduces from top to bottom during etching process [85] and this nonuniformity is more significant for long porous wire.

The other interesting phenomena we can read from the SIMS profile is that

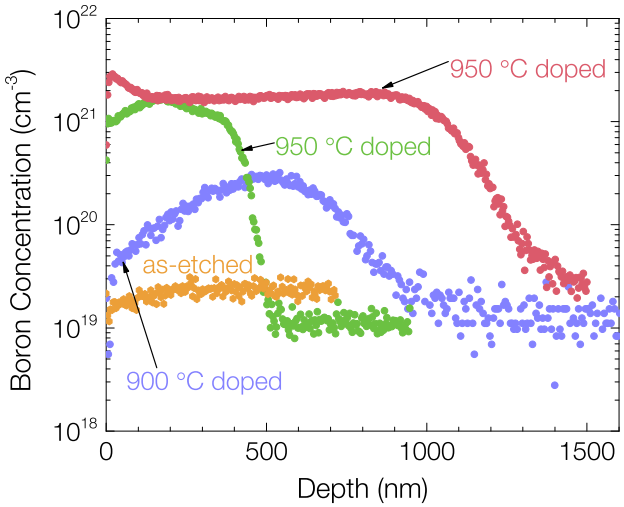

Figure 4.4: Boron concentration of as etched/post-doped porous silicon nanowire characterized by SIMS.

the boron concentration not only exceeds the solubility at the temperature used ($2 \times 10^{20} \sim 4 \times 10^{20}$ cm^{-3} at 950 °C [88, 89]) but also the solubility limit at 1350 °C [88]. In a recent published review on boron diffusion in silicon and germanium, Mirabella et al. [154] pointed out that this extraordinary high boron doping concentration is due to the boron-interstitial clustering.

4.2 Carrier concentration analysis by Raman spectroscopy

In this section, we will try to extract the carrier concentration as well as crystalline size information from Raman spectrum analysis. The general procedure was discussed in Section 3.4.3. We will also discuss the limitations and possible drawback of this approach.

As discussed previously, 785 nm excitation wavelength collects most of the signal from substrate and as a result, we only analyze the Raman spectrum with 532 nm excitation wavelength. And the line focused laser power was kept at 0.1 mW with exposure time 60 sec. For substrate measurement we used 0.2 mW to achieve better signal-to-noise ratio without affected by heating since it has much larger thermal conductivity (~90 W/(m·K) at

Table 4.1: Fitted parameters of the Raman spectrum of as-etched and post-doped porous silicon NW and the substrate from which the NWs were fabricated. The substrate peak shift was obtained by Fano line-shape fitting $\omega_0 + \delta\omega_0$, Γ/q is not included.

Sample	**Peak Position (cm^{-1})**	**FWHM (cm^{-1})**
p+ substrate (2013)	520.49	9.14
p+ substrate (2014)	520.78	6.94
as-etched porous NW (2013)	518.83	6.14
as-etched porous NW (2014)	519.06	5.46
post-doped porous NW (950 °C)	517.82	14.1
post-doped porous NW (900 °C)	518.46	11.2

room temperature) compared with porous silicon nanowire. The normalized measured spectra of the representative tested porous NW is shown in Fig. 4.5 and the fitting parameters are listed in Table 4.1. Post-doped and as-etched porous NW both showed a red-shift compared with the substrate and post-doped NW has larger red-shift. While as-etched NW is narrower than the substrate, post-doped NW exhibits a much wider peak width. How do we explain the changes?

For temperature effects, as we discussed before, ΔT due to laser heating at 0.1 mW is smaller than 10 K and the corresponding width broadening is less than 0.1 cm^{-1}. Since we are using spectrum width as evaluation parameter, heating effect can be neglected.

Tensile stress can also cause the red-shift of Raman spectrum. However regardless of the stress type, it will broaden the spectrum. This contradicts with the fact that the Raman spectrum of as-etched NW is narrowed compared with the bulk.

For both the nanowire samples, we have already confirmed the existence of nanocrystalline in porous Si NW with TEM and the dimension is roughly around 10 nm. Based on theory calculation, Raman spectrum width broadening due to 10 nm nanocrystalline is less than 1.5 cm^{-1} [135]. We also have

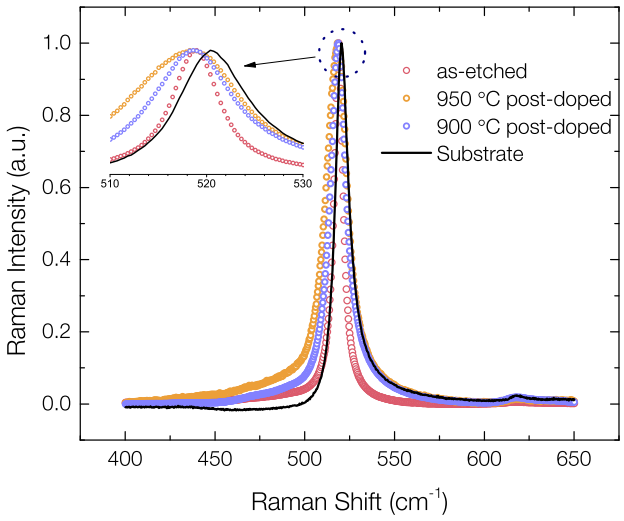

Figure 4.5: Normalized Raman spectrum of as-etched and post-doped porous silicon NW and the substrate from which the NWs were fabricated. The excitation wavelength was 532 nm.

doping information from SIMS analysis, hence the Raman spectrum should have contribution from both the nano crystalline induced phonon confinement and doping/carrier, as a result Eq. 3.18 is used to fit the NW Raman spectrum. The doping concentration of as-etched NW and substrate is about 3×10^{19} cm^{-3} and the 950 °C and 900 °Cpost-doped nanowire has a boron concentration about 1×10^{21} cm^{-3} and 1.4×10^{20} cm^{-3}. We will first discuss the as-etched NW spectrum and later extend it to post-doped NW analysis.

4.2.1 Analysis of as-etched porous nanowire Raman spectrum

Regarding the peak shift, for dopant concentration of 3×10^{19} cm^{-3}, we can calculate the peak shift due to impurity effect based on Eq. 3.15 to be $\sim$ +0.28 cm^{-1} and from Table 3.3 we can also read that for bulk silicon -0.3 cm^{-1}$< \delta\omega_p <$0 . So the red-shift of as-etched NW should be mainly attributed to the phonon confinement effect.

Then how do we explain the narrower spectrum peak width of as-etched

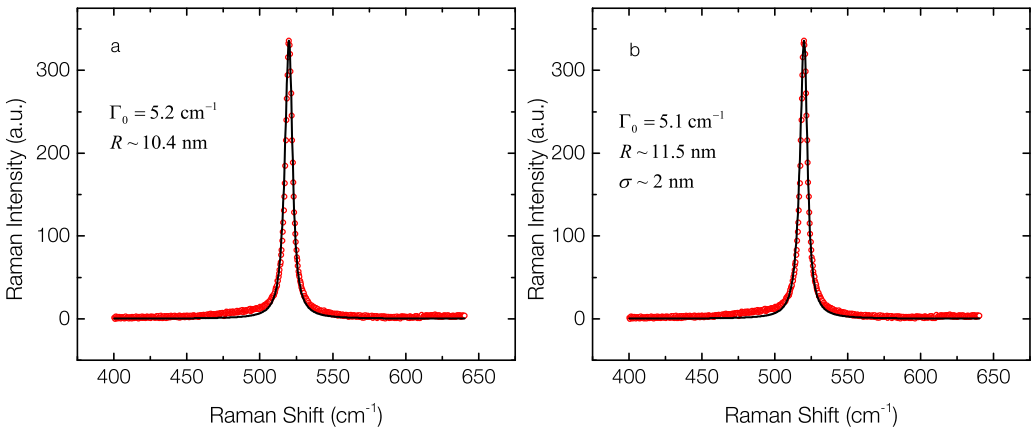

Figure 4.6: Raman spectrum of as-etched porous nanowire fitted by phonon confinement model (a) assume one critical size (b) assume crystalline size has a Gaussian distribution.

porous NW compared with substrate? Both phonon confinement and high doping concentration are supposed to broaden the peak. We learnt from our previous electrical measurement that in the as-etched porous nanowire, it is 10^7 more resistive than the bulk silicon with similar doping. There might be a large reduction of free carriers in a-etched porous nanowire which is similar to that observed in other previous studies on porous silicon [33, 49]. As a result, we should compared the peak width of an-etched NW with low doped bulk silicon, for example 3.57 cm^{-1} for silicon with $10 \sim 20$ Ω·cm resistivity as mentioned in Section 3.4.1.

We can fit the Raman spectrum based on Eq. 3.18 and 3.22 as shown in Fig. 4.15. Actually a range of $\Gamma_0 = 5 \pm 0.2$ cm^{-1} and $R \sim 10 \pm 1$ nm (if only consider one critical size) or $R \sim 12 \pm 2$ nm, $\sigma \sim 3 \pm 1$ nm (Gaussian distributed size) can fit the experiment spectrum quite well.

Now we compare the phonon natural FWHM $\Gamma_0 \sim 5$ cm^{-1} (instrument broadening included) with literature value in Table 3.3. We see that the value is between spectrum width of bulk silicon with 5×10^{18} cm^{-3} and 1.5×10^{19} cm^{-3} carrier concentration. In other words, the free carrier concentration in our as-etched nanowire is less than its doping level which is about 3×10^{19} cm^{-3} but should be higher than 5×10^{18} cm^{-3}. This is a clear indication of loss of free carriers. Phonon confinement leads to an additional 0.6 cm^{-1} broadening.

Table 4.2: Raman peak shift in highly boron doped silicon. Data adopted from Ref. [111]. Impurity induced peak shift is calculated by Eq. 3.15.

Carrier Concentration (cm^{-3})	$\delta\omega_{total}$ **(cm^{-1})**	$\delta\omega_{impurity}$ **(cm^{-1})**	$\delta\omega_{free-carrier}$ **(cm^{-1})**
1.6×10^{20}	-4.9	+1.3	-6.2
4.0×10^{20}	-11.8	+3.8	-15.6

4.2.2 Analysis of post-doped porous nanowire Raman spectrum

Temperature and strain effect arguments are the same as before.

We first look into the peak shift. Again by applying Eq. 3.15, for boron concentration 1×10^{21} cm^{-3} (sample doped at 950 °C) , peak would have a blue-shift of $\sim$ 9.6 cm^{-1} due to impurity effect only while the spectrum has a redshift $\sim$ 3.6 cm^{-1} compared with doped substrate (without Γ_p/q). Thus there must be some other mechanisms to cause a redshift of $\sim$ 13.2 cm^{-1} . This cannot only be due to phonon confinement because that: (1) by assuming the phonon natural width is the same as as-etched NW i.e. $\Gamma_0 \sim 5$ cm^{-1}, a crystalline size $\sim$1 nm is required to achieve such a large redshift; (2) with this crystalline size the spectrum would be greatly distorted as shown in Fig. 4.7. From the highly doped bulk silicon data in Ref. [111], we can approximate the free-carrier induced peak redshift as listed in Table 4.2. Thus free carrier concentration in between 1.6×10^{20} cm^{-3} and 4.0×10^{20} cm^{-3} together with phonon confinement should be able to induce a redshift required for the post doped porous nanowire. As we will discuss in detail shortly, by fitting the measured Seebeck coefficient of post-doped porous nanowire, we extracted the free carrier concentration to be $\sim 1.6 \times 10^{20}$ cm^{-3} , this agrees well with the doping range we discussed above considering the experimental error.

To start with, we fitted the experimental spectrum with on Eq. 3.18 and 3.22, phonon natural width Γ_0 and crystalline size are fitting parameters. The fitting results are shown in Fig. 4.8. As in the as-etched porous nanowire case, $\Gamma_0 = 14 \pm 0.6$ cm^{-1} and $R = 6.5 \pm 0.5$ nm (if only consider one critical size)

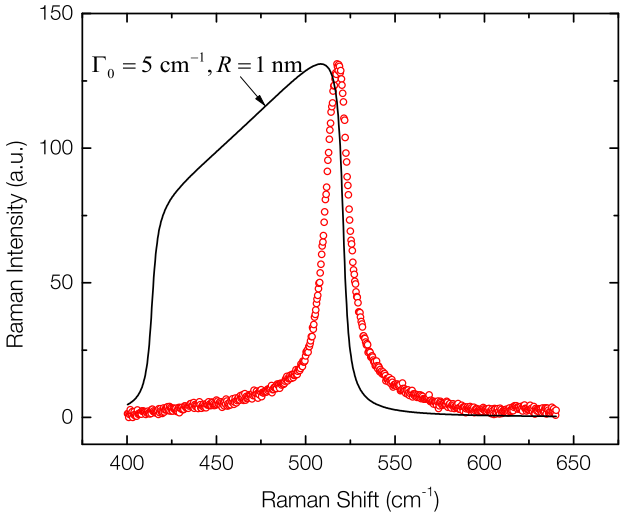

Figure 4.7: In order to achieve peak redshift ∼13 cm^{-1} only by phonon confinement effect, the crystalline size has to be as small as ∼1 nm and the simulated spectrum is greatly distorted..

or $R \sim 7.5 \pm 1.1$ nm and $\sigma \sim 1.6 \pm 0.7$ nm (size has Gaussian distribution) can reasonably fit the experiment spectrum.

Raman spectrum of NW that was post-doped at 900 °C can be analyzed in the same way as illustrated in Fig. 4.9. $R = 7.7 \pm 1$ nm and $\sigma = 1$ nm can reasonably fit the experiment spectrum.

Now let us try to introduce the Fano interaction by Eq. 3.24. By setting asymmetric factor q_p to be equal to the bulk value (1.6×10^{20} cm^{-3} free carrier concentration) listed in Table 3.3, the fitting does not agree with the experimental spectrum because it does not show a clear Fano signature (asymmetric peak with a local minimum). This may be attributed to the suppression of Fano effect in porous silicon by quantum confinement of electrons, which results in the discretization of continuum electron energy [155]. When we increase q_p to above 20, the higher wavenumber portion can be fitted well as illustrated in Fig. 4.10.

However, for the fitted phonon natural width Γ_0, we cannot simply compare it with the bulk value width $2\Gamma_p$ in Table 3.3 to estimate the free carrier concentration. This is because that their line-shape are different. From Fig. 4.10 we can see that the Fano line-shape should have larger line width than the width of experimental spectrum due to the local minimum in the

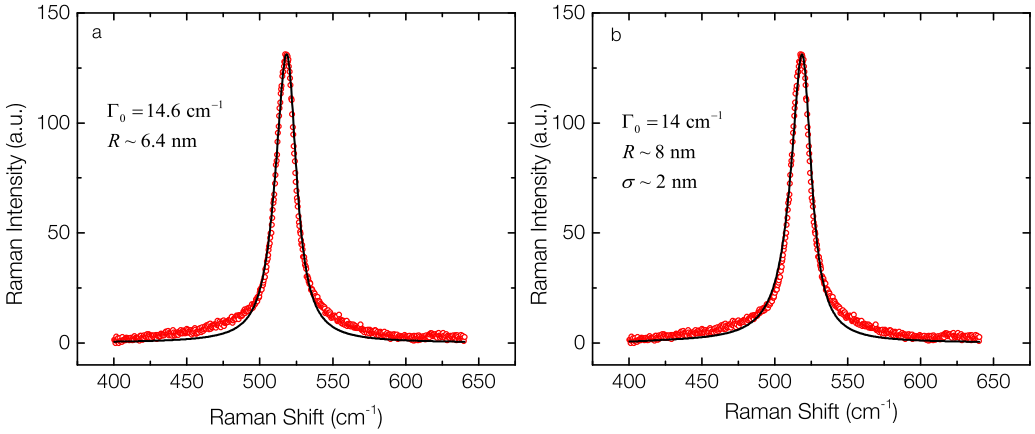

Figure 4.8: Raman spectrum of porous nanowire post doped at 950 °C fitted by phonon confinement model (a) assume one critical size (b) assume crystalline size has a Gaussian distribution.

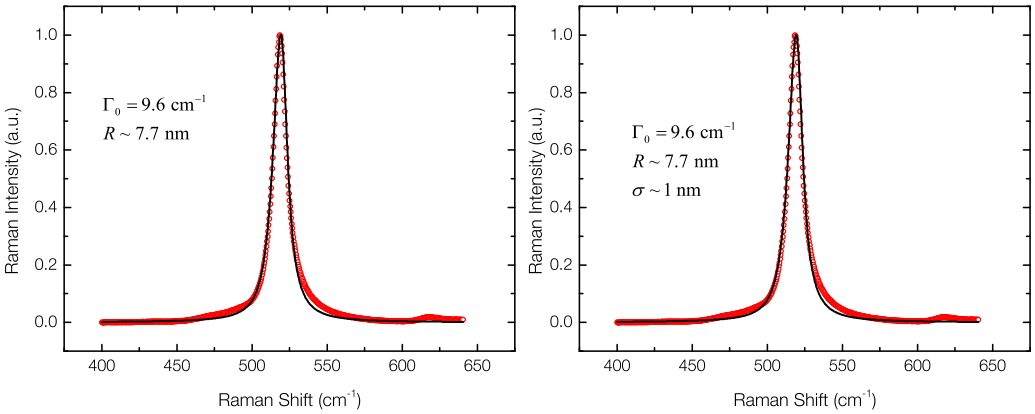

Figure 4.9: Raman spectrum of porous nanowire post doped at 900 °C fitted by phonon confinement model (a) assume one critical size (b) assume crystalline size has a Gaussian distribution.

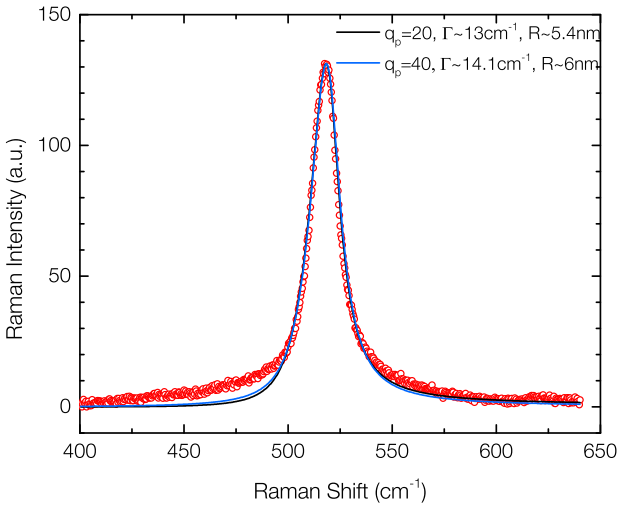

Figure 4.10: Raman spectrum of post-doped porous nanowire fitted by phonon confinement model coupled with Fano interaction (Eq.3.24).

low wave number part. Besides different system have different instrument broadening. Take these into consideration, $\Gamma_0 = 14 \pm 0.6$ cm^{-1} indicates that the free carrier concentration in the 950 °C post-doped porous silicon nanowire should be larger than 6×10^{19} cm^{-3} ($2\Gamma_p = 12.4$ cm^{-1}) and close to 1.6×10^{20} cm^{-3} ($2\Gamma_p = 16.4$ cm^{-1}) [111] or 1.5×10^{20} cm^{-3} ($2\Gamma_p = 17.7$ cm^{-1}) (as shown in Table 3.3). For 900 °C doped sample, $\Gamma_0 \sim 9.6$ cm^{-1} and we estimated the carrier concentration to be between 1.5×10^{19} cm^{-3} and 6×10^{19} cm^{-3}.

4.2.3 Discussion on the Raman spectrum analysis

From Raman spectrum analysis, it is conclusive that there are loss of free carriers in those porous nanowires and post-doping does introduce more carriers. However the role of carrier mobility is not clear and very rarely discussed.

When applying the phonon confinement model, we can estimate the nano crystalline size. Here we were assuming the nano crystalline in between the pores has a cylinder like shape instead of nano sphere. The extracted nanocrystalline size is around 10 nm and agrees with the estimation from TEM images. It seems that after post-doping, the crystalline size was de-

creased. One possible reason might be sintering at high temperature. The major concern with this fitting process is the phonon confinement constant. From Eq. 3.18, 3.20 and 3.22, we see that it is R/β that really affects the spectrum simulation. Besides we were assuming cylindrical nanocrystalline and this is a simplification of the disordered structure. Though $\beta = 2\sqrt{2}\pi$ were mostly used value in the literature, we still needs other confirmation to get the exact value of nanocrystalline size.

In the fitting, we were using Eq. 3.19 for optical phonon dispersion. $\omega_0 \sim$ 521 cm^{-1} should be intrinsic silicon Raman shift peak position when $k = 0$ selection rule is valid. For 3×10^{19} cm^{-3} boron doped silicon, both from literature and our calculation in previous section we concluded that the doping effect on peak shift is negligible, hence this A and B is applicable in as-etched nanowire spectrum simulation. When boron doping concentration reaches 1×10^{21} cm^{-3} , we are not certain how this will affect the optical phonon dispersion. Take 950 °C doped sample as example, when analyzing the Raman spectrum by phonon confinement model, it is possible that the Raman spectrum peak of nanowire with 1×10^{21} cm^{-3} dopants and 1.6×10^{20} cm^{-3} remains the same before size effect is introduced. Since we are using FWHM Γ_0 as evaluation parameter, we may neglect the error in the peak shift position analysis.

Although through natural width analysis we can confirm the higher free carrier concentration, we still have to investigate why the Fano line asymmetry became much less prominent. Moreovre, it is not quite clear that how much contribution is from the substrate in the nanowire Raman spectrum under resonant excitation. However, the clear difference in width between as-etched NW, post-doped NW and substrate might be an evidence that the substrate contribution is negligible.

4.3 Seebeck coefficient of porous silicon nanowire

4.3.1 Experimental data of Seebeck coefficient

In Fig. 4.12 we show the measured Seebeck coefficient of the as-etched and post-doped porous nanowire (post-doping temperature 900 °C and 950 °C), as a comparison we also plot the Seebeck coefficient of substrate from which those porous nanowire were fabricated. We see that as-etched porous nanowire has similar Seebeck coefficient as substrate and both the post-doped nanowires have lower Seebeck coefficient because of increased free carriers.

Note that as-etched data is not smooth and has large error, one reason is the limitation of our measurement technique. For highly resistive media such as the as-etched porous nanowire, there would be huge phase difference between the top of nanowire and the bottom of the nanowire and hence the measured $V_{2\omega}$ is no longer a good representative of the average voltage drop due to the $\Delta T_{2\omega}$, this effect is more severe for longer as-etched nanowires. For post-doped nanowires, however the $V_{2\omega}$ signal follows the temperature oscillation. We demonstrated this effect by showing $V_{2\omega}$ phase from room temperature measurement in Fig. 4.11. The other reason comes from the instrument limitation. SR830 Lock-in amplifier has an input impendence of 10 MΩ. As shown previously in [20], electrical resistance increased with decreasing temperature. At room temperature for $\sim 1.2\,\mu$m as-etched nanowire the resistance between two Seebeck voltage pads was about 0.5 MΩ and it reached several MΩ at low temperature. In this case the lock-in amplifier can no longer measure the correct $V_{2\omega}$ voltage and that is why we do not have data below 110 K for as-etched wire.

4.3.2 Theory of Seebeck coefficient

The Seebeck effect arising from diffusion of charge carriers along temperature gradient is usually enhanced by drag imposed on the carriers by the accompanying diffusion of phonons. Thus the total Seebeck coefficient is generally

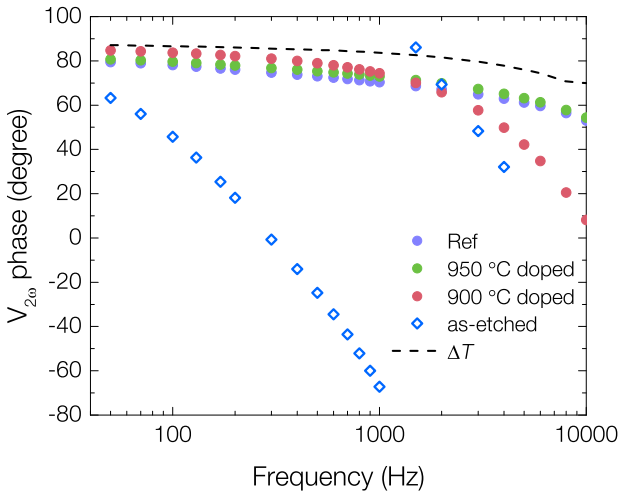

Figure 4.11: Phase of Seebeck voltage $V_{2\omega}$ at 300 K measurement. We see from the figure that for post-doped nanowire and reference sample, the phase follows temperature oscillation. For as-etched nanowire the Seebeck voltage signal has huge phase difference across the frequency range.

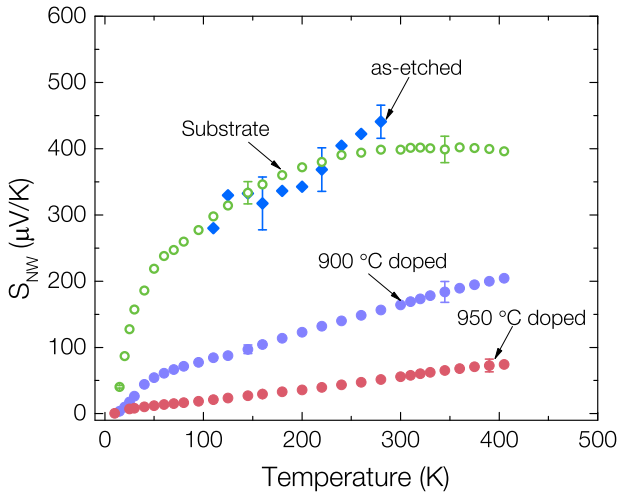

Figure 4.12: Seebeck coefficient of as-etched porous nanowire, post-doped porous nanowire (post-doping temperature 900 °C and 950 °C). Bulk silicon with about 3×10^{19} cm^{-3} boron concentration is also shown by the open circle.

expressed as a sum of diffusion component S_d and phonon drag contribution S_{ph} [156]. The diffusion component S_d is a measure of the average energy transported by the an electron (or hole) above the Fermi level under the open circuit condition [5]. It is expressed by Eq. 4.1

$$\begin{aligned} S_d &= \frac{1}{eT}\left(\frac{\langle \tau E\rangle}{\langle \tau\rangle} - E_F\right) \\ &= \frac{1}{eT}\left(\frac{\int_{E_b}^{\infty} ED(E)v(E)\Lambda(E)\frac{\partial f_0}{\partial E}dE}{\int_{E_b}^{\infty} D(E)v(E)\Lambda(E)\frac{\partial f_0}{\partial E}dE} - E_F\right) \end{aligned} \tag{4.1}$$

where $D(E)$ is density of states, $v(E)$ is the velocity of the carrier and f_0 is the equilibrium Fermi-Dirac distribution at temperature T, E_F is the Fermi energy and energy at band edge E_b is set to be zero, $\Lambda(E) = v(E)\tau(E)$ is the electron mean free path (MFP). The first term in Eq. 4.1 depends ont the dominant carrier scattering process and second term i.e. the Fermi energy E_F depends on the carrier concentration. In order to evaluate this scattering process there are two approaches [20]: (1) solve the Boltzman transport equation for detailed carrier scattering rates with acoustic phonons, ionic impurities, inter-valley scattering, boundary scattering, optical phonon and plasma scattering. The overall scattering rate τ^{-1} or MFP Λ is evaluated by Matthiessen's rule [21]; (2) assume the electron mean free path follows a power law dependence on energy $\Lambda \propto E^r$ where r is the characteristic scattering constant [157], or electron relaxation time $\tau_e \propto E^{r-1/2}$. Using the second approach, S_d can be written as

$$S_d = \frac{k_B}{e}\left[\frac{(r + D/2 + 1/2)F_{r-1/2+D/2}(\eta)}{(r - 1/2 + D/2)F_{r+D/2-3/2}(\eta)} - \eta\right] \tag{4.2}$$

where D is the dimensionality factor, eta is the reduced Fermi energy and $F_j(\eta) = \int_0^{\infty} \frac{x^j}{1+\exp(x-\eta)}dx$ is the jth order Fermi-Dirac intergral. Note that scattering constant r defined here has a 1/2 difference with the definition by Pichanusakorn and Bandaru [157]. In the case of 3D material, S_d is simplified as

$$S_d = \frac{k_B}{e}\left[\frac{(r + 2)F_{r+1}(\eta)}{(r + 1)F_r(\eta)} - \eta\right] \tag{4.3}$$

Normally, the scattering constant r varies between 0 and 2 [20]. $r = 0$ stands for scattering with longitudinal acoustic phonon, $r = 1$ is for optical

phonon scattering and $r = 2$ represents the extreme limit for ionic impurity scattering.

In the case of degenerately doped semiconductor or metal, diffusion part of Seebeck can be descried by Mott formula [158], shown in Eq. 4.4

$$S_d = \frac{\pi^2}{3}\frac{k_B^2 T}{e}\left\{\frac{d[ln(\sigma(E))]}{dE}\right\}_{E=E_F} \tag{4.4}$$

where $\sigma(E) = e^2\tau(E)v^2D(E)$ is differential conductivity which is a measure of contribution of electrons with energy E to the total electrical conductivity (total conductivity $\sigma = \int \sigma(E)\left(-\frac{\partial f}{\partial E}\right)dE$). Mott formula is general valid regardless of conduction mechanisms, to name a few, through band states, localized states, hopping and etc [159]. For nearly free electrons or holes, Eq. 4.4 can be further calculated as in Eq. 4.5 [160]

$$S_d = \frac{8\pi^2 {k_B}^2}{3eh}m^*T\left(\frac{\pi}{3n}\right)^{2/3}\left(1 + \frac{d(\ln(\lambda))}{d\ln(E)}\right)_{E=E_F} \tag{4.5}$$

where m^* is the density of states effective mass [6, 160], in Si for hole $m^* = 0.81m_e$; n is carrier concentration and λ is scattering length. In the case of parabolic band and energy-independent approximation [160], Eq. 4.5 has the simplest form

$$S \doteq \frac{8\pi^2 {k_B}^2}{3eh}m^*T\left(\frac{\pi}{3n}\right)^{2/3} \tag{4.6}$$

Theory and experiment work on phonon drag component S_{ph} is incomplete. Contributions of phonon drag were first observed in low temperature Seebeck coefficient of single crystal bulk Si [161, 162] and Ge [156, 163]. Previous theories proposed a non-equilibrium approach to model momentum exchange between electron and phonon [164]. People had the notion that S_d reduced significantly at room temperature especially at highly doped material [165], Sadhu et al. [20] recently discovered that contrary to the traditional understanding, phonon drag contributed significantly of the Seebeck coefficient of Si ($\sim$ 33 %) even at 300 K and $\sim 10^{19}$ cm^{-3} doping. And at the same time phonon boundary scattering completely quenched S_d in silicon

nanowires.

Traditionally phonon drag component in semiconductor was modeled by

$$S_{ph} = \frac{1}{3ne} \int_{\omega} C_{\omega} \frac{\tau_{pp}(\omega)}{\tau_{pp}(\omega) + \tau_{ep}(\omega)} \, d\omega \tag{4.7}$$

where C_ω is the volumetric specific heat capacity of phonon mode, τ_{pp} is the phonon lattice interaction relaxation rate and τ_{ep} is the electron phonon interaction relaxation rate. From Eq. 4.7 we see that when Umklapp scattering starts τ_{pp} is reduced significantly hence quenched the S_{ph}, similar arguments also applies in the highly doped case when phonon impurity scattering is increased. This is how the traditional interpretation that S_{ph} is inconsequential at room temperature and highly doping comes from. However, Sadhu et al. [20] pointed out that a spectrum of phonon frequencies contributing to phonon drag component S_d should be considered, i.e. low frequency phonons that contribute to S_{ph} and high frequency phonons which is important in heat conduction should be distinguished. With this consideration, an frequency upper limit in the integral of Eq. 4.7 has to be placed. Sadhu provided a formal theory for phonon drag component S_{ph} [20].

4.3.3 Explanation of Seebeck coefficient of porous silicon nanowire

In our previous study we discovered that in silicon nanowire, the phonon drag contribution was completely quenched by phonon boundary scattering and left with diffusion part S_d. Since all the porous silicon nanowires were fabricated from degenerately doped silicon, we first simply analyzed the Seebeck coefficient with Mott formula Eq. 4.6. For post-doped porous wires, By fitting S-T with Mott formula we can extract the actual amount of carriers. The fitting is shown in Fig. 4.13. For 950 °C post-doped sample, we can fit the data from 25 K to 405 K; however for 950 °C post-doped nanowire, S deviates from Mott formula below 50 K. This may indicate that at low temperature, phonon drag still exists in 900 °C doped sample [160, 20].

For porous nanowire post doped at 950 °C, we extracted carrier concen-

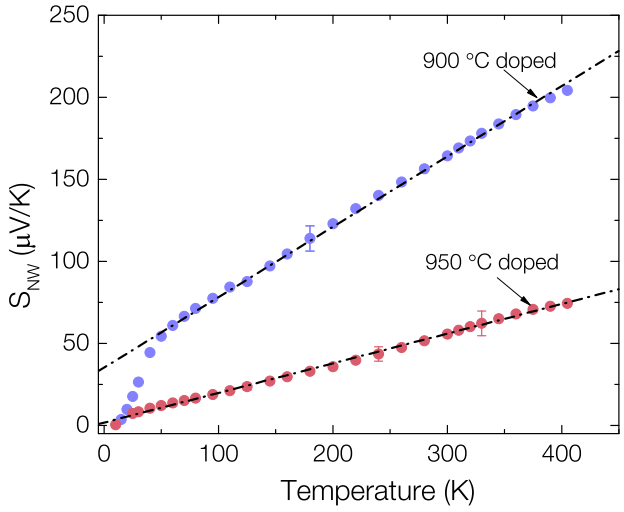

Figure 4.13: Seebeck coefficient of post-doped porous nanowire (post-doping temperature 900 °C and 950 °C) fitted by Mott formula. Carrier concentration extracted is about 1.6×10^{20} cm^{-3} and 4.5×10^{19} cm^{-3} for 950 and 900 °C) post-doped sample respectively.

tration to be about 1.6×10^{20} cm^{-3} and for 900 °C post-doped nanowire, we extracted the hole concentration is about 4.5×10^{19} cm^{-3}. These results agree fairly well with the analysis of Raman spectrum discussed in Section 4.2.

Now let us investigate the electron transport by analyzing the Seebeck coefficient with Eq. 4.3. For as-etched nanowire, the low electrical conductivity may be due to loss of free carriers which are trapped by surface states. Moreover, disturbance either from surface states trapping or disordered structure caused geometrical effect also reduces carrier mobility significantly. We have discussed this in Section 2.3. From Raman analysis of the as-etched nanowire, we concluded the hole concentration in as-etched nanowires was less than 1.5×10^{19} cm^{-3} and larger than 5×10^{18} cm^{-3}. As mentioned in Section 4.1.2, due to the fact the wire resistance dominates over contact resistance, we were able to measure the as-etched porous wire electrical conductivity based on a two-point probe array scale. We measured conductivity as function of temperature, shown in Fig. 4.14. Since $\mu = \sigma/(ne)$ and n is constant with temperature for degenerately doped silicon, carrier mobility and conductance of our as-etched nanowire should follow the same temperature trend. It make sense for us to also plot the mobility data of a porous silicon from Ref. [77] in the same figure under same scale as a comparison.

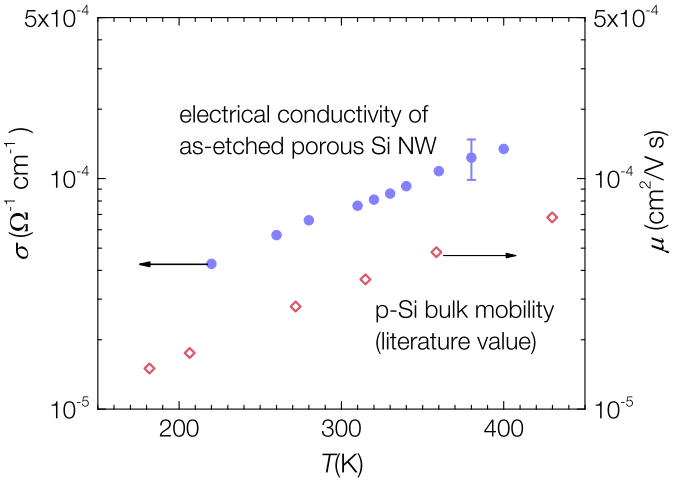

Figure 4.14: Measured electrical conductivity of as-etched porous nanowire as a function of temperature. Literature data of porous silicon mobility is shown as a comparison [77].

Carrier mobility can also be described by the energy scattering exponent r as in Eq. 4.8 [157]. For a given system, both diffusion contributed Seebeck coefficient and mobility should have the same scattering energy parameter r. Thus we can fit Seebeck coefficient (diffusion dominated) and conductivity (identical to mobility fitting) separately to extract the scattering parameter r, only the actual carrier concentration condition can give a good match between the two exponents.

$$\sigma \propto \mu = A\frac{e}{m_\sigma}(k_B T)^{r-1/2}\frac{F_r(\eta)}{F_{1/2}(\eta)} \tag{4.8}$$

To start with we tried to fit the Seebeck coefficient of as-etched nanowire by setting carrier concentration to be the same as doping level $\sim 3 \times 10^{19}$ cm^{-3}. We require an abnormally high scattering index $r = 3.8$ while a best fit for conductivity gives $r = 3$. This further verifies that the free carrier concentration is less than the doping level. We then repeat this procedure in the range of $5 \times 10^{18} < n < 1.5 \times 10^{19}$ cm^{-3}. $r = 2.6 \sim 2.7$ gives a good fit for electrical conductivity fit in all the tested carrier concentration range, while for Seebeck coefficient, $r = 2.3 \sim 2.7$ can fit the data because of the large measurement error. The fitting for $n = 1.3 \times 10^{19}$ cm^{-3} and $r = 2.7$ is shown in Fig. 4.15.

Based on the fitting result, we estimate the free carrier concentration in

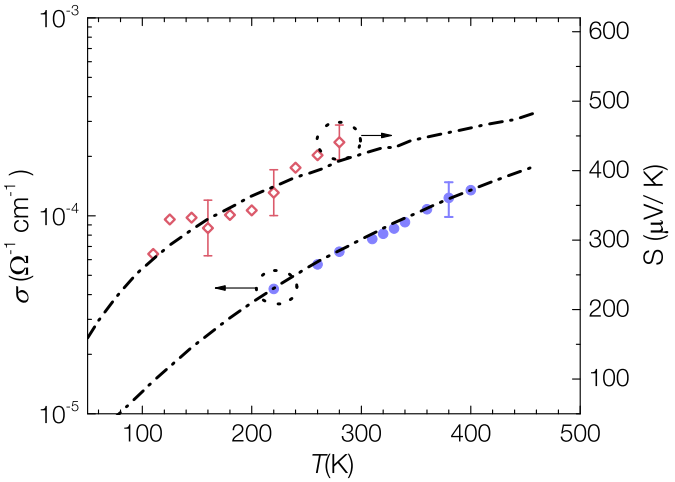

Figure 4.15: Electrical conductivity and Seebeck coefficient fitting of as-etched porous silicon nanowire. Here we are using carrier concentration 1.3×10^{19} cm^{-3} and scattering parameter $r = 2.7$.

as-etched nanowire to be around 1×10^{19} cm^{-3}. It is clear that both reduction of free carriers and their mobility contribute to the low electrical conductivity. The extraordinary large r may indicate a strong electron scattering in as-etched porous nanowires.

For porous nanowire post-doped at 900 °C and 950 °C, we directly use $n = 4.5 \times 10^{19}$ cm^{-3} and $n = 1.6 \times 10^{20}$ cm^{-3} respectively. The fitting result is shown in Fig. 4.16. We extracted $r = 0.7$ for 900 °C post-doped nanowire and $r = 0$ for 950 °C post-doped nanowire. $r = 0$ is a clear evidence that the dominant scattering is electron acoustic phonon scattering. Electron scattering is enhanced in 900 °C post-doped nanowire which means porous structure may also play a role in electron transport.

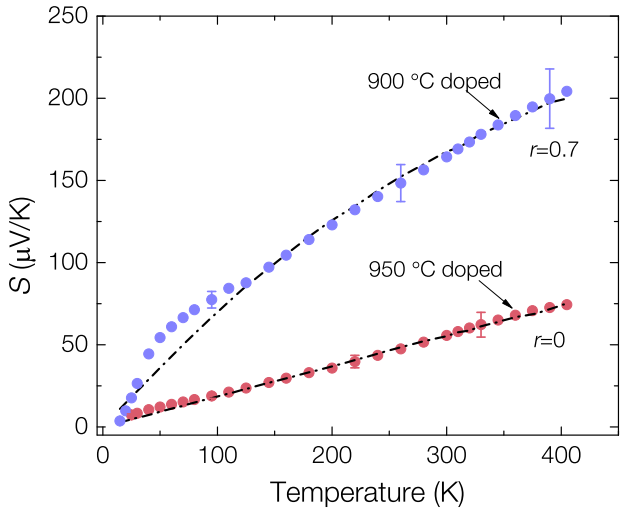

Figure 4.16: Seebeck coefficient fitting of porous silicon nanowire post doped at 900 °C and 950 °C. Carrier concentration and scattering component are $n = 4.5 \times 10^{19}$, $r = 0.7$ and $n = 1.6 \times 10^{20}$, $r = 0$ respectively.

CHAPTER 5

THERMAL TRANSPORT IN POROUS SILICON NANOWIRE

5.1 Detailed thermal conductivity measurement results

We have measured thermal conductivity data of as-etched porous nanowire, 900 °C and 950 °C post-doped porous nanowire from 30∼405 K using the platform discussed in Section 3.2. As mentioned previously, SOG thermal conductivity should be accurately determined at all the measurement temperature. We spun coat SOG on silicon substrate and measured its thickness by both ellipsometry (n and k of our SOG were extracted and attached in Appendix B and cross-section SEM. Then we directly patterned gold heater onto it since SOG itself was a good dieletric material and conducted 3ω measurement. The measurement result is shown in Fig. 5.1.

By differential measurement we extracted the thermal conductivity of nanowire/SOG composite, the composite thermal conductivities of all the porous nanowires are shown in Fig. 5.2. Thermal conductivity of SOG is also included in the plot.

Knowing area coverage of nanowire as x, we can calculate thermal conductivity of nanowire by $[k_{comp}-(1-x)k_{SOG}]/x$. Experiment results are shown in Fig. 5.3. Big error bar mainly comes from the geometrical factors, i.e. actual conducting length and area as discussed in Section 3.2.2. Error was analyzed as described in Section 3.2.2, the overall uncertainty in thermal conductivity was between 23 ∼24%. Within the error range, all the measured nanowire have similar thermal conductivity regardless of doping condition, this may indicate that the low thermal conductivity should mainly be attributed to the porous structure.

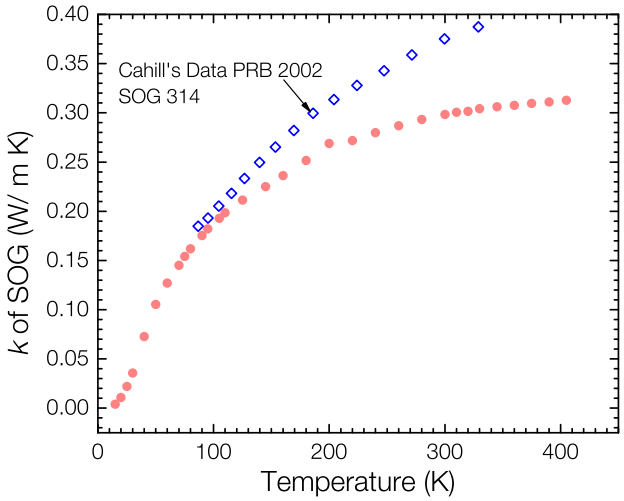

Figure 5.1: Thermal conductivity of SOG used in our experiment (Filmtronics® SOG 500F). Thermal Conductivity of SOG 314 measured by Costescu et al. [93] is shown as a reference.

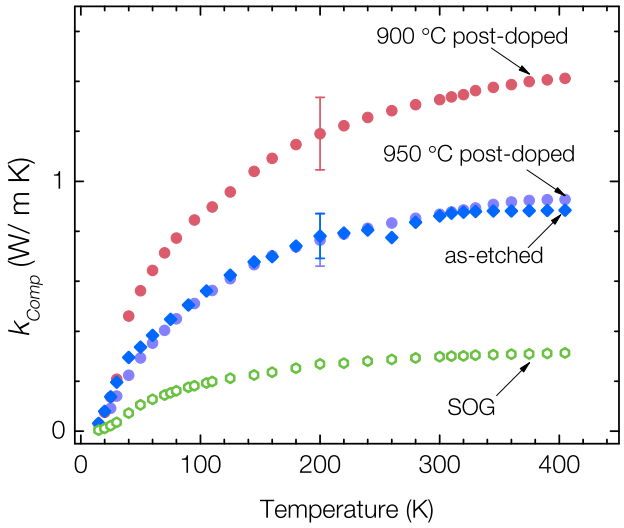

Figure 5.2: Thermal conductivity of nanowire and SOG composite, the NW sampless are as-etched porous nanowire, 900 °C and 950 °C post-doped porous nanowire.

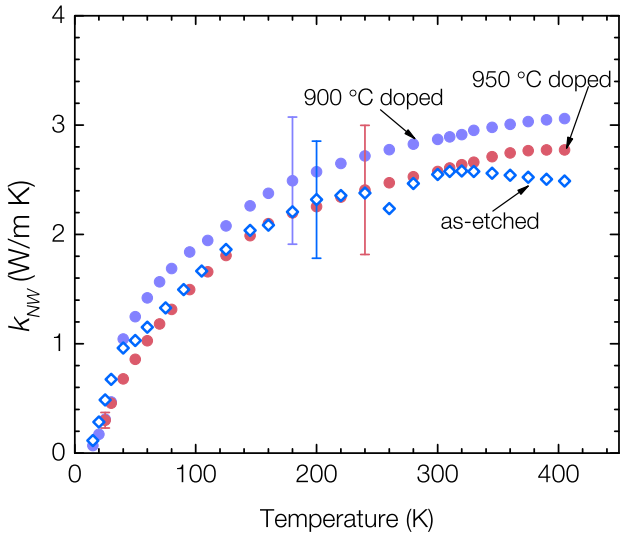

Figure 5.3: Thermal conductivity of as-etched porous nanowire, 900 °C and 950 °C post-doped porous nanowire.

5.2 Thermal conductivity modeling theory

5.2.1 Lattice thermal conductivity from kinetic theory

By kinetic theory lattice thermal conductivity is expressed as

$$k_L = \frac{1}{3}\sum_{i=1}^{3}\int_0^{q_c} \tau_i(q){v_i}^2(q)\frac{\partial f}{\partial T}\hbar\omega_i(q)D_i(q)\,dq \tag{5.1}$$

where f is the Bose-Einstein distribution for phonon $f = \frac{1}{\exp\left(\frac{\hbar\omega}{k_BT}\right)-1}$, q_c is the cut-off wave vector. The sum is over three acoustic phonon branches which are two transverse branches and one longitudinal branch, and optical branches do not contribute to thermal transport. By taking the derivative of Bose-Einstein distribution, we write the equation above as

$$k_L = \frac{1}{3}\sum_{i=1}^{3}\int_0^{q_c} \tau_i(q){v_i}^2(q)\frac{\exp\left(\frac{\hbar\omega_i}{k_BT}\right)}{\left[\exp\left(\frac{\hbar\omega_i}{k_BT}\right)-1\right]^2}\frac{(\hbar\omega_i)^2}{k_BT^2}\frac{q_i^2}{2\pi^2}\,dq \tag{5.2}$$

In stead of doing calculation by summing over all three acoustic branches, a simpler treatment is lumping them into a single but triply degenerate branch

[166]. From this single acoustic branch we can extract an effective sound velocity v_s. v_s should be determined through a proper average such that the thermal conductivity $k(T)$ modeling should be exact at low temperature limit when phonon MFP is only limited by frequency-independent boundary scattering[166]. This leads to in Eq. 5.3 [166]

$$\frac{1}{{v_s}^2} = \frac{1}{3}\left(\frac{1}{v_{sL}} + \frac{2}{{v_{sT}}^2}\right) \tag{5.3}$$

where in Si, v_{sL} is 8973 m/s and v_{sT} is 5398 m/s and as a result $v_s = 6084$ m/s [167, 168, 166].

With averaged v_s the lattice thermal conductivity can be simplified as

$$k_L = \int_0^{q_c} \tau {v_s}^2 \frac{\exp\left(\frac{\hbar\omega}{k_B T}\right)}{\left[\exp\left(\frac{\hbar\omega}{k_B T}\right) - 1\right]^2} \frac{(\hbar\omega)^2}{k_B T^2} \frac{q^2}{2\pi^2}\, dq \tag{5.4}$$

Phonon acoustic branches had a variety of approximation, the most widely used dispersion was the Debye liner model $\omega = v_s q$. Debye cut-off frequency $\omega_D = 8.6 \times 10^{13}$ rad/s has been used as cut-off frequency traditionally [169, 170], other values like $\omega_D = 6.93 \times 10^{13}$ rad/s was also adopted [171]. Mingo [170] suggested that theoretical calculation using a lower cut-off frequency $\omega_c = 4.2 \times 10^{13}$ rad/s agreed well with experimental silicon nanowire thermal conductivity. Ma et al. used $\omega_c = 4.3 \times 10^{13}$ rad/s when explaining thermal conductivity of inverse opal [43]. Other approximated dispersions were also used, such as sine-type Born-von Karman dispersion $\omega = \omega_0 \sin\left(\frac{\pi q}{2 q_0}\right)$ [166, 171], fourth order polynomial [172]. Mingo used complete phonon dispersion relations which did not require any externally imposed frequency cut-off to predictively calculate lattice thermal conductivity of silicon nanowire [170].

The original model for scattering time was developed by Callaway [169] and Holland [173]. The scattering rate can be written as $\tau^{-1} = \sum_{i=1}^{n} {\tau_i}^{-1}$ by Matthiessen's rule. Impurity scattering is always modeled as $\tau_{imp}^{-1} = A\omega^4$,; anharmonic scattering is modeled as $\tau_U^{-1} = B\omega^2 T e^{-C/T}$. A, B, C are all numerical constants and we will discuss this shortly. Phonon crystal boundary scattering is $\tau_b^{-1} = v/(FL)$ where F is a geometric parameter represents

a correction due to the finite length to thickness ratio and sample surface roughness, for example, to fit the bulk low-doped silicon thermal conductivity $F = 0.6$ for dimension $L = 7$ mm. In highly doped silicon, correct modeling of phonon-electron scattering is crucial [174, 21].

Impurity scattering can come from isotope, impurity or defects, the overall effects would be $A = \sum_j A_j$. In the case of isotope and impurity dopants, an analytical expression considering the mass difference is [174]

$$A_{\delta M} = \frac{nV_2}{4\pi v_s^2}\left(1 - \frac{M_0}{M}\right)^2 \tag{5.5}$$

where n is the volumetric concentration of point imperfections, M and V are mass and crystal volume of host atom, i.e. Si in our case, M_0 is the mass of imperfection. For intrinsic silicon, $A = 1.32 \times 10^{-45}$ s^3 due to isotope scattering is obtained [173, 174, 170]. A more general form of mass difference induced constant in the case of multiple point imperfections is [21]

$$A_{\delta M} = \frac{nV^2}{4\pi {v_s}^3}\sum_i f_i\left(1 - \frac{M_i}{M}\right)^2 \tag{5.6}$$

where f_i is the percentage of imperfection type i whose mass is M_i. In the case of highly doped silicon more effects contribute to constant A. Lattice distortion due to imperfection also changes the relaxation time and the corresponding scattering constant is

$$A_{\delta R} = \frac{2nV^2}{\pi v s_3} Q_0^2 \gamma \left(\frac{\delta R}{R}\right)^2 \tag{5.7}$$

where γ is Grüneisen constant and parameter Q_0 describes how the nearest and further-out linkage combine in scattering matrix [174]. Asheghi et al. obtained $A_{\delta R}$ to be 2.66×10^{-45} s^3 for a phosphorous doping of 1.7×10^{20} cm^{-3} [174]. Besides $A_{\delta M}$ and $A_{\delta R}$, unintentional impurity (such as oxygen atom contamination) induced scattering constant A_x may contribute more in the case of highly doped silicon. Asheghi et al. discovered that $A_x = 11.75 \times 10^{-45}$ s^3 was required in order to explain some of their data [174].

As to anharmonic scattering, both normal and Umklapp process should be included. Mingo [170] pointed out that at higher frequencies Umklapp scattering dominates over normal process, and in the case of system with small dimension, boundary scattering dominates at lower frequencies. B and C can be adjusted in order to reproduce the bulk thermal conductivity data and various values were adopted in literature [170, 171, 21].

Phonon-electron scattering modeling is challenging and complicated. Asheghi et al. [174] employed deformation potential and shear deformation potential for phonon scattering with free electrons [175, 167, 176] and bound electrons/holes [177, 178, 179] respectively. Phonon-free electron/hole scattering rate was modeled as $\tau_e^{-1} \propto (E_D^2 T/v^2)$ for wavevector $q < 2K_F$ where k_F was minimum allowable wavevector of electrons to interact with phonons, while for $q > 2K_F$, $\tau_e^{-1} \propto (E_D^2 T/q^5)$. Deformation potential has to be obtained for different doping level. To account for all the doping range, Ma et al. [21] evaluated transition rate due to phonon electron scattering first and later summed all the rates over spins, valleys and all final electronic states.

In our data analysis, phonon-electron scattering is calculated by $\tau_{elec}^{-1} = v_s \Lambda^{-1}$ where the phonon-electron scattering mean free path is

$$\Lambda^{-1}{}_{ph-elec} = \frac{\hbar\omega}{k_B T} \frac{1}{2 l_{ae}} f_0(\frac{q}{2}) \tag{5.8}$$

$$l_{ae} = \frac{\pi \hbar^4 \rho v^2}{{m_e}^2 \Xi^2 k_B T}$$

$$f_0(\frac{q}{2}) = \frac{1}{1 + \exp\left(\frac{\hbar^2 q^2}{8 m_e k_B T} - \frac{E_F - Ec}{k_B T}\right)}$$

where Ξ is the deformation potential. To calculate the reduced Fermi energy $\eta = (E_F - E_C)/k_B T$ (for hole $\eta = (E_V - E_F)/k_B T$), we start with the carrier concentration calculation in conduction band (or valence band). Use electron as an example, electron concentration is calculated as in Eq. 5.9

$$n = \int_{E_C}^{\infty} D(E) f_0(E)\, dE = \int_{E_C}^{\infty} \frac{D(E)\, dE}{1 + \exp\left(\frac{E - E_F}{k_B T}\right)} \tag{5.9}$$

where E_C is the energy of conduction band, $f_0(E)$ is Fermi-Dirac distribution, $D(E)$ is the density of states. For a three dimensional system with parabolic conduction band, we calculate the carrier concentration to be

$$n = 2\left(\frac{2\pi m_e^* k_B T}{h^2}\right)^{3/2} \frac{2}{\sqrt{\pi}} \int_0^\infty \frac{x^{1/2}}{1+\exp(x-\eta)}\, dx \tag{5.10}$$

where m_e^* is the density of states effective mass of electrons. And we can define the density of states of electrons in conduction band as

$$N_C = 2\left(\frac{2\pi {m_e}^* k_B T}{h^2}\right)^{3/2} \tag{5.11}$$

and we see that $F_{1/2}(\eta) = \int_0^\infty \frac{x^{1/2}}{1+\exp(x-\eta)}\, dx$ is Fermi-Dirac integral of order 1/2. We can define it in another way as

$$\mathscr{F}_{1/2}(\eta) = \frac{2}{\sqrt{\pi}} \int_0^\infty \frac{x^{1/2}}{1+\exp(x-\eta)}\, dx \tag{5.12}$$

More generally, $\mathscr{F}_j(\eta) = F_j(\eta)/\Gamma(j+1)$. Fermi integral can only be numerically calculated and Ref. [180] provides a good reference. The the electron concentration is then $n = N_C \mathscr{F}_{1/2}(\eta)$. If we know the doping concentration as N_D, then the carrier concentration can be calculated using Eq. 5.13

$$n = N_D \left(1 - \frac{1}{1 + \frac{1}{g_D}\exp\left[(E_D - E_F)/k_B T\right]}\right) \tag{5.13}$$

where E_D is the ionization energy for donor atoms, the factor $g_D = 2$ stands for the ground state degeneracy of donor impurity level. For holes, the ionized acceptors is calculated as in Eq. 5.14

$$p = N_A \left(1 - \frac{1}{1 + \frac{1}{g_A}\exp\left[(E_F - E_A)/k_B T\right]}\right) \tag{5.14}$$

where E_A is the ionization energy for acceptor atoms, the factor $g_A = 4$ stands for the ground state degeneracy of acceptor impurity level which comes from that the doubly degenerate acceptor level can accept one hole of either spin [181]. For degenerately doped silicon, we can simply use $n = N_D$ or $p = N_A$. By equating Eq. 5.13 or Eq. 5.14 (p-type) and Eq. 5.10 we can solve for the

reduced Fermi energy η. We can also use an approximate expressions, for example Eq. 5.15 proposed by Joyce and Dixon [182].

$$\eta \cong \ln \frac{n}{N_C} + \frac{1}{\sqrt{8}} \frac{n}{N_C} - \left(\frac{3}{16} - \frac{\sqrt{3}}{9} \right) \left(\frac{n}{N_C} \right)^2 + \cdots \tag{5.15}$$

However this approximation is not accurate for $\eta > 2$. For calculation of holes, we just replace the density of states effective mass of electrons with that of holes. In silicon, for electrons $m_e^* = 1.08 m_e$ and for holes ${m_h}^* = 0.81 m_e$.

5.2.2 Electron contribution to thermal conductivity

Heat can also carried by electrons diffusion and Wiedemann-Franz law describes the electron contribution k_e to be

$$k_e = \sigma L T \tag{5.16}$$

where σ is electrical conductivity, L is Lorenz number and T is temperature. An empirical value of Lorenz number is normally used in the case of metal, where $L = \frac{\pi^2}{3}(k_B/e)^2 = 2.44 \times 10^{-8}$ W Ω K^{-2}. For bulk silicon, lattice thermal conductivity dominates. However in the case of porous nanowire, since the thermal conductivity value is quite low as shown in Fig. 5.3, k_e may contribute a large portion especially in the post-doped nanowires. We should carefully examine the value of Lorentz number. Pichanusakorn and Bandaru [157] provided an accurate expression for L, shown in Eq. 5.17.

$$L = \left(\frac{k_B}{e} \right)^2 \left[\frac{\left(r + \frac{D}{2} + \frac{3}{2} \right) F_{r+D/2+1/2}(\eta)}{\left(r + \frac{D}{2} - \frac{1}{2} \right) F_{r+D/2-3/2}(\eta)} - \left(\frac{\left(r + \frac{D}{2} + \frac{1}{2} \right) F_{r+D/2-1/2}(\eta)}{\left(r + \frac{D}{2} - \frac{1}{2} \right) F_{r+D/2-3/2}(\eta)} \right)^2 \right] \tag{5.17}$$

where r is the scattering constant as defined in Section 4.3.2, again we should be noted that scattering energy dependent parameter r defined here has a 1/2 difference with the definition by Pichanusakorn and Bandaru [157]. D is dimensionality factor, η is the reduced Fermi energy and $F_j(\eta) = \int_0^\infty \frac{x^j}{\exp(x-\eta)+1} dx$ is the jth order Fermi integral. We see from Fig. 5.4 that for $\eta > 10$, $L \cong 2.44 \times 10^{-18}$ W Ω K^{-2}. At higher temperature (small η),

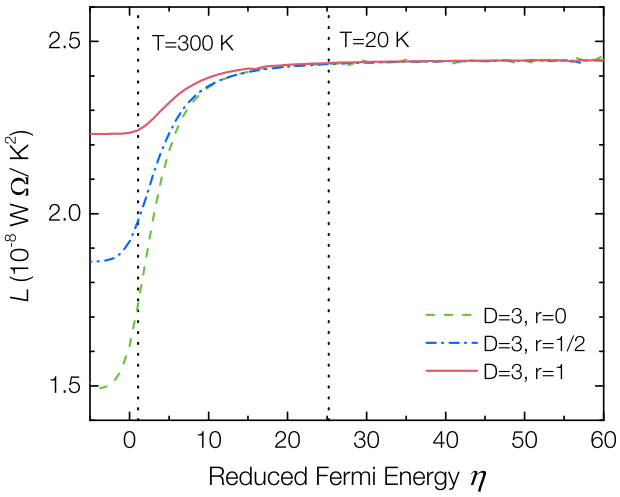

Figure 5.4: Lorenz number as a function of reduced Fermi energy. For carrier concentration 3×10^{19} cm^{-3}, $\eta \approx 1$ at 300 K and $\eta \approx 25$ at 20 K. Figure was regenerated followed Ref. [157].

L is smaller than the empirical value, and the difference for large scattering constant is small. As a result, for our post-doped nanowires where the carrier concentration is more than 3×10^{19} cm^{-3} (which means larger η at a certain temperature) and large scattering constant, it would be reasonable to use empirical Lorentz number across the measurement temperature range to estimate k_e.

The electrical conductivity as a function of temperature can also be modeled. However the process is complicated and may not agree with the experimental data. Here we simply fitted experimental value to extract σ-T relations [183].

5.2.3 Porosity effect

Porous structure is a two-phase system. The simplest form is that two materials form parallel or series transport network. For materials with thermal conductivity k_1 and k_2 (volume fraction ϕ), the effective thermal conductivities are:

$$\textit{parallell} \qquad k_{eff} = (1-\phi)k_1 + \phi k_2 \tag{5.18}$$

$$\textit{series} \qquad k_{eff} = \left(\frac{1-\phi}{k_1} + \frac{\phi}{k_2}\right)^{-1} \tag{5.19}$$

Our SOG/nanoiwire is a parallel thermal transport network. For a porous system, the second phase is usually air or vacuum, a simple treatment would be the effective medium theory (EMT) originally proposed by Maxwell [184]. In this model, the temperature field perturbation due to many small inclusions was treated to be the same as one big inclusion. The shape of the void is usually sphere and the effective medium thermal conductivity is then

$$k_{eff} = \frac{1-\phi}{1+\phi/2} k_S \tag{5.20}$$

where k_S is thermal conductivity of the solid part, this is known as Maxwell-Eucken limit [185]. For solid with cylindrical inclusions the Eucken limit is $k_{eff} = k_S(1-\phi)/(1+\frac{2}{3}\phi)$ [186]. And for 2D system with infinitely long cylindrical voids the effective thermal conductivity is $k_{eff} = k_S(1-\phi)/(1+\phi)$. There are many complicated forms of effective medium theory and they were summarized and reviewed in [187, 188]. Recent approaches in understanding the thermal transport process in a porous medium were through computer simulation. A pore network was first generated, for example, random fractal square pore network [67], layers of different porosity [189], then simulated heat flux transported from one side to the other side. The heat flux can be modeled either with traditional Fourier equation or by solving Boltzmann transport equation [67]. Meanwhile the solid thermal conductivity can be modified by kinetic theory with estimated phonon MFP [67, 190].

In general, effective medium theory provides a good estimate for small porosity or when the contrast between two materials is small. However, the prediction for a system with large porosity and/or big contrast between materials is not reliable. Besides in the actual porous system such as porous silicon or silicon nanowire, there are different morphologies with randomly distributed pore of different sizes, irregular shapes and surfaces, which imposes great challenge to the effective medium theory.

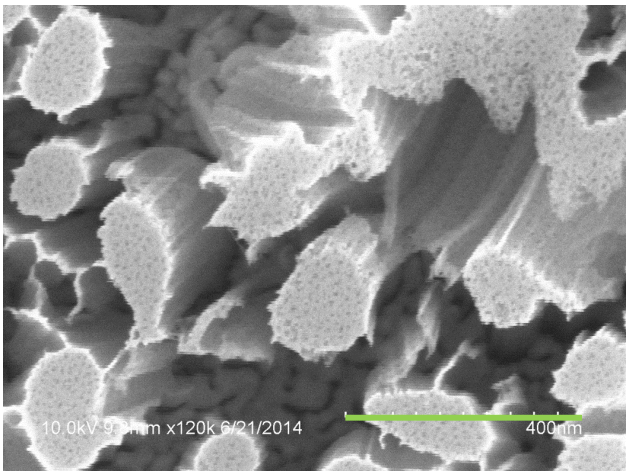

Figure 5.5: High resolution SEM image of porous nanowire top view. The scale bar is 400 nm.

One critical information lacking in our porous nanowire is the actual porosity. The porosity of porous nanowires can be characterized by Brunauer-Emmett-Teller (BET) gas (nitrogen) adsorption method as described in [81]. In this method, approximately 15∼20 mg material is required in order to minimize the mass determination error. In Hochbaum's measurement they used half a four inch wafer to generate about 40 µm long nanowire with area coverage about 40%. Since the pore formation varies with etching, we need to use porous nanowire with similar length for BET measurement. For porous nanowire etched from highly doped p-type Si (< 5 mΩ·cm) the measured pore volume was 0.88 cm^3/g, using the density of silicon, we calculated the porosity of their sample to be ∼67%. However in our nanowire fabrication procedure, the area coverage was normally between 25% to 35% with wire length about 1 µm, as a result at least 20 four-inch wafers are required. We may get a sense of the pore size and coverage from a high resolution SEM of wire top view, as illustrated in Fig. 5.5. From the SEM, the pore dimension and the edge-to-edge dimension should be around 10 nm. We could not give an number of porosity based on cross section analysis however it should be much smaller than 67%.

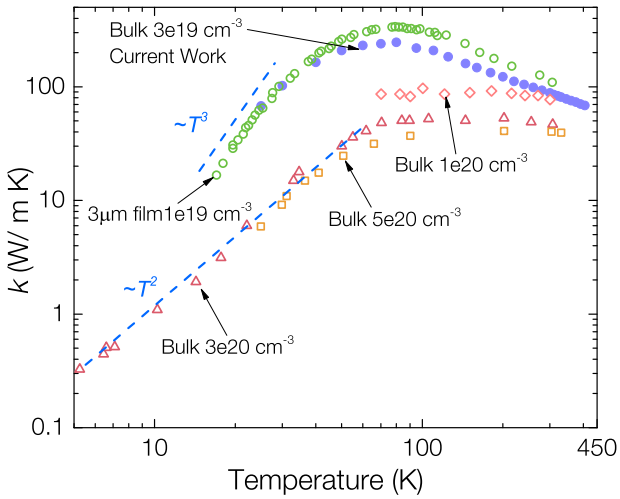

Figure 5.6: Thermal conductivity of highly boron doped p-type silicon. We measured 3×10^{19} cm^{-3} doped silicon and thermal conductivity values from literature are also shown here as comparison [174].

5.3 Theoretical interpretation of porous silicon nanowire thermal conductivity

5.3.1 Substrate thermal conductivity

From our measurement we also extracted the properties of substrate. Here we present the thermal conductivity data of p-type silicon with Boron doping concentration of 3×10^{19} cm^{-3} in Fig. 5.6, as a comparison, we also plot the thermal conductivity data of boron highly doped p-type Si at different level doping level [174]. We see from the figure that thermal conductivity decreases as doping concentration grows, besides the temperature at which thermal conductivity peaks also become higher. Good agreement with literature value validates our measurement.

We now try to explain our substrate thermal conductivity in which lattice contribution dominates. The fitting result using a simple Debye linear dispersion is shown in Fig. 5.7. Phonon-electron scattering was modeled using the approach we discussed above. The fitting parameters we obtain are $A = 3 \times 10^{-45}$ s^3, $B = 2.2 \times 10^{-19}$ s/K, $C = 110$ K and $\Xi = 2$ eV. As we discussed before in 3ω method, resistance temperature calibration is flat below 30 K and dR/dT changes rapidly in that region. The calculated temperature

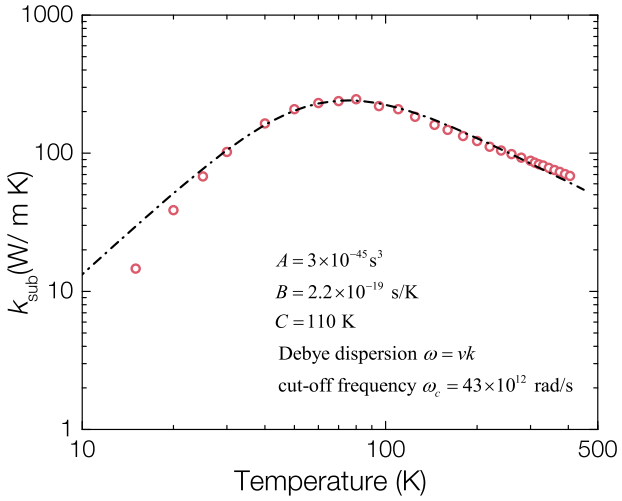

Figure 5.7: Thermal conductivity fitting of 3×10^{19} cm^{-3} boron doped p-type silicon with listed parameters. We use linear Debye dispersion with cut-off angular frequency $\omega_c = 4.3 \times 10^{13}$ rad/s.

increase would be overestimated and thus result in a lower thermal conductivity. This explains why the fitting curve in low temperatures is higher than the experimental curve in Fig. 5.7. We include thermal conductivity below 30 K as a reference although they are not very reliable due to limitations of 3ω method. The accuracy of fitting also depends on precise determination of carrier concentration. We can only estimate the doping concentration from SIMS characterization and its error affects the phonon electron scattering modeling.

5.3.2 Porous NW thermal conductivity modeling

In porous nanowire, in addition to the scattering we mentioned above, the major challenge is how to model the phonon scattering with nano-crystalline or pores. The simplest treatment is considering it as boundary scattering $\tau_{pore}^{-1} \propto v_s/d_g$, where d_g is size related to porous structure and independent of phonon frequency, this is referred to as *gray* assumption [171]. For example, Hopkins [172] used distance between pores as critical dimension when interpreting thermal conductivity data of Song et al's porous Si film [38] and their Si phononic crystal [186]. A more general approach is to model nanocrystalline scattering as frequency dependent $\tau_{pore}^{-1} \propto v_s\omega^n/d_g$ with n ranges from

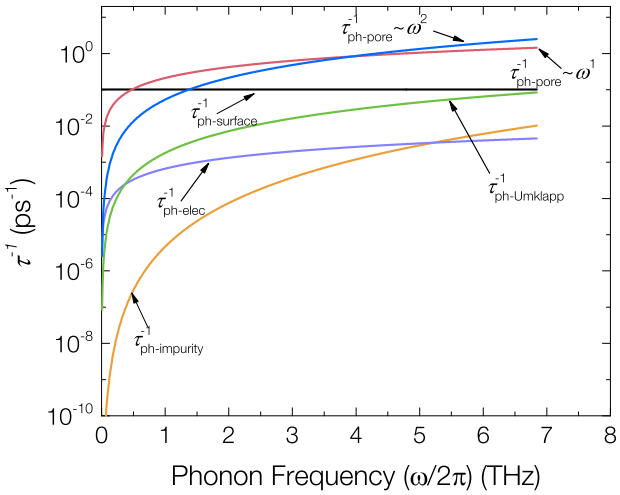

Figure 5.8: Comparison of scattering rates at room temperature.

$0 \sim 2$. [191]. Wang et al. [171] adopted this and modeled grain boundary scattering as

$$\tau_{pore} = \frac{v_s}{\alpha d}\frac{\omega}{\beta\omega_c} \tag{5.21}$$

where α is the geometry factor that considers the transmission through grain boundary, β is dispersion dependent constant. Wang et al. further pointed out that β should be fixed because gray scattering rate was a limit of Eq. 5.21 when strong boundary scattering happened at $T >> T_{Debye}$ [171]. $\beta = 2/3$ for Debye dispersion and $\beta \sim 0.71$ for Born-von Karman dispersion. Fang et al. applied the same treatment when analyzing the thermal conductivity of of ordered mesoporous nanocrystalline silicon thin film and obtained good fit across the measurement temperature range [42]. We now fit the measured effective thermal conductivity with both $\tau^{-1}_{pore} \propto \omega^0$ and $\tau^{-1}_{pore} \propto \omega^1$ first.

We also plot different scattering rate at 300 K in Fig. 5.8, it is clear that phonon nanocrystalline scattering dominates.

As we discussed previously, here we just treat the porosity effect by a scaling factor, thus our fitting of effective thermal conductivity is valid without losing physical meaning. Besides, we also set critical nanocrystalline dimension as a fitting parameter. Since BvK and Debye dispersion gave very close fitting for bulk data, we will only use Debye dispersion with cut-off angular frequency $\omega_c = 4.3 \times 10^{13}$ rad/s. We already know that σ is very small for

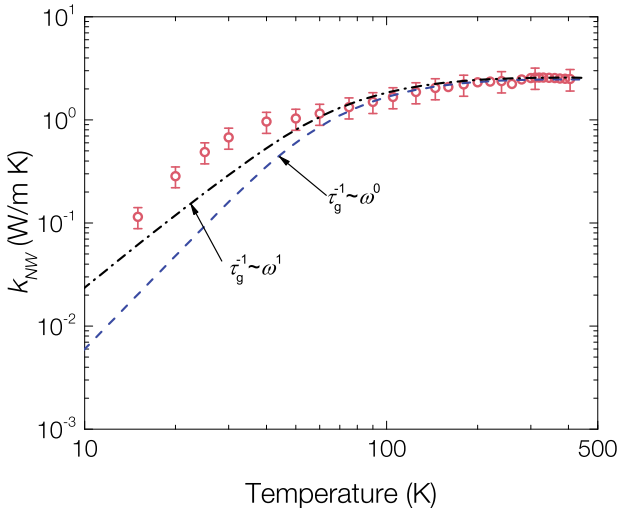

Figure 5.9: Thermal conductivity fitting of as-etched porous NW by assuming phonon nanocrystalline scattering rate is proportional to ω^0 and ω^1.

as-etched nanowire and hence electron thermal conductivity k_e is negligible. We see from Fig. 5.9 that both ω^0 and ω^1 assumption cannot capture the low temperature dependence.

We now assume the phonon nanocrystalline scattering rate is proportional to ω^2 and repeating the fitting process. The fitting result of as-etched porous nanowire is shown in Fig. 5.10. Within the error range, we obtain good match in the whole temperature range.

For post-doped nanowires thermal conductivity, we have to consider the electron contribution k_e. However, except carrier concentration extracted Seebeck coefficient analysis we do not know the exact electrical conductivity. Carrier transport in porous silicon nanowire is a complex and not fully understood process. In order to model the mobility, except the well studied electron scattering process such as scattering with impurity and phonons, we also have to include the surface state trapping and disordered structure effect. Here we discuss two extremes. The lower limit of k_e can be estimated from the upper limit of the post doped nanowire which was extracted from the two-point probe electrical measurement. We have discuss this in Section 4.1.1. For 950 °C post-doped nanowire, the upper limit of electrical resistiv-

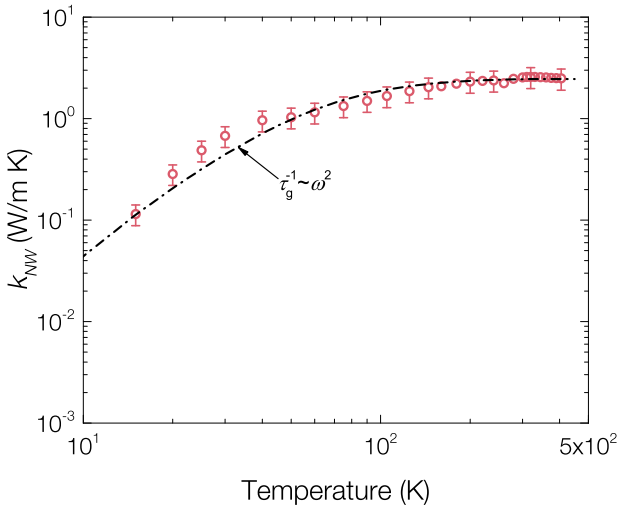

Figure 5.10: Thermal conductivity fitting of as-etched porous nanowire by assuming phonon nanocrystalline scattering rate is proportional to ω^2.

ity is on the order of $10 \sim 10^2$ Ω·cm, i.e. the conductivity is on the order of $10^{-1} \sim 10^{-2}$ Ω^{-1}·cm^{-1}. By WiedemannCFranz law, k_e cannot be larger than 7.32×10^{-5} W/(m·K) at 300 K and 4.88×10^{-6} W/(m·K) at 20 K. This means that k_e can also be neglected in the lower limit. When assuming the carrier mobility is the same as bulk value, we obtain the upper limit of k_e. We obtain $\sigma(T)$ simply from fitting literature value at similar doping level [183]. We first try to fit the effective thermal conductivity of post-doped nanowire with only lattice contribution as shown in Fig. 5.11. Upper limit of k_e is also included.

Compared with k_e, at low temperature k_{ph} dominates, however we see that high temperature, only k_{ph} cannot explain the increasing trend. It is a clear evidence that k_e contributes more to the post-doped thermal conductivity. Intriguingly, this may indicate that the resistivity of our post doped nanowire is much lower than value extracted from the two-point probe measurement. If we add the upper limit k_e and redo the fitting, we can match the high temperature part as shown in Fig. 5.12.

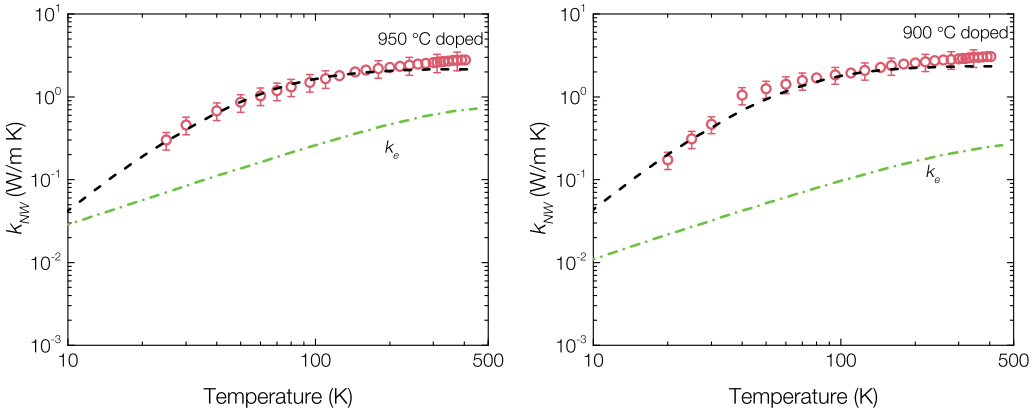

Figure 5.11: Lattice thermal conductivity fitting of porous nanowire post doped at 950 and 900 °C respectively. Phonon pore scattering rate is proportional to ω^2. k_e is the upper limit of electron thermal conductivity.

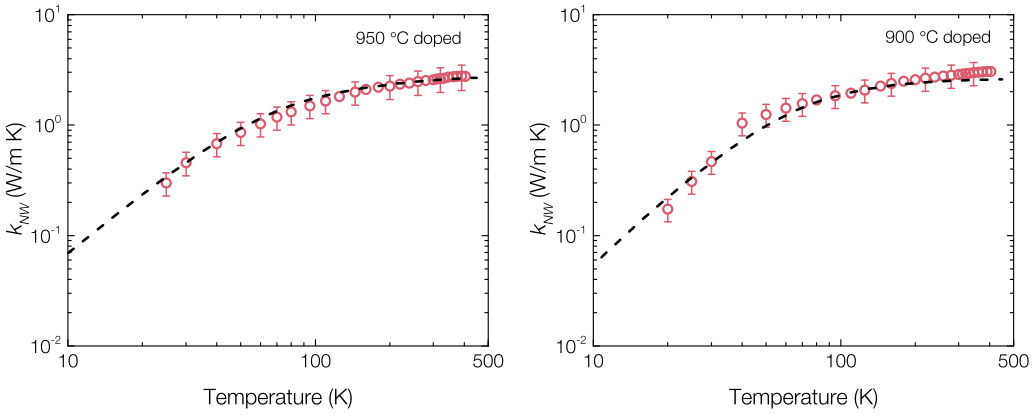

Figure 5.12: Thermal conductivity fitting of porous nanowire post doped at 950 and 900 °C respectively, we have included the upper limit k_e. Phonon pore scattering rate is proportional to ω^2.

5.4 Discussion

It would be worthwhile to estimate lower limit of thermal conductivity of the disordered crystalline silicon by a amorphous limit model proposed by Cahill et al. [192] and compare that with our experimental data. This model assumed that the heat transport in crystals was a random walk of the thermal energy only between neighboring atoms vibrating randomly and the resulting thermal conductivity is

$$k_{min} = \left(\frac{\pi}{6}\right)^{1/3} k_B n^{2/3} \sum_i v_i \left(\frac{T}{\theta_i}\right)^2 \int_0^{\theta_i/T} \frac{x^3 e^x}{(e^x - 1)^2}\, dx \qquad (5.22)$$

The sum is over the three acoustic modes with speed of sound v_i, and $\Theta_i = v_i(\hbar/k_B)(6\pi^2 n)^{1/3}$ is the cut-off frequency for each polarization expressed in degree K where n is the atom number density. We calculate the minimum thermal conductivity of disordered silicon and compare with as-etched porous nanowire shown in Fig. 5.13. Our measured thermal conductivity of porous silicon nanowire is above the lower limit. At low temperature, this lower limit model model has T^2 dependence but predicts thermal conductivity values much lower than our experimental data. In order to fit our data with this model, we either have to increase the speed of sound or atomic density which can not be valid for porous structure.

How to model phonon pore multiple scattering is a challenging problem. We see that scattering rate with ω^2 dependence explained our data very well. However we are still working on the formulation which will appear in our following publication. Here we will briefly review the related work on wave multiple scattering that has been studied in decades. In an early study of radiation scattering by Pekeris [193], each scattering was treated as a perturbation and the intensity after multiple scattering was calculated to be $E_{scatt} \propto q^4 f(q)$, where q is the wave vector, q^4 represents the Rayleigh scattering and $f(q)$ introduces additional ω dependence.

In following studies, to simplify the problem, the actual scattering system (nanowire in our case) was divided into many *thin* slices and later integral over them [194, 195]. Wave scattering in such a thin slice is illustrated in

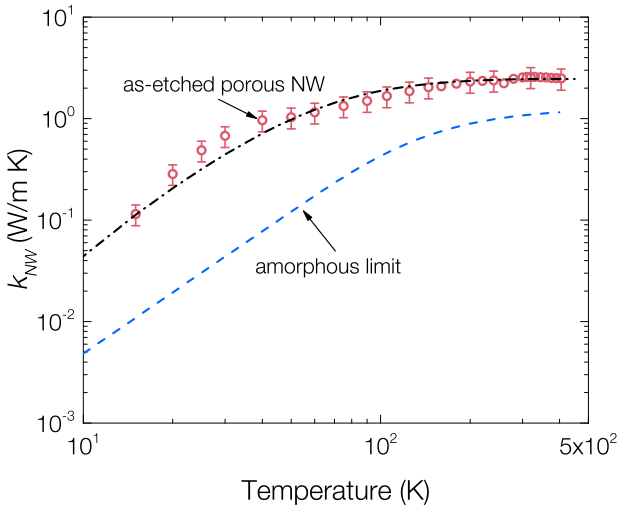

Figure 5.13: Thermal conductivity predicted by Cahill's lower limit of disordered crystal [192]. We also show the thermal conductivity of as-etched porous wire.

Fig. 5.14.

Following Fejer's derivation [194], loss of power density from the un-scattered wave by scattering in a slice of thickness dz can be written as

$$dQ = -QAdz \tag{5.23}$$

where A is total power removed from an incident beam with unit power when scattering with unit thickness slice. We further define $B = Az$ as "effective depth of scattering", then Eq. 5.23 can be written as

$$\frac{dQ}{dB} = -Q \tag{5.24}$$

After one scattering the total power density is Q_1, the loss of power can be written as

$$dQ_1 = -Q_1 Adz + QAdz \tag{5.25}$$

where $-Q_1 Adz$ is the loss term and $QAdz$ is the gain from the scattering from previous un-scattered wave. Again we can re-write the equation as Eq. 5.24 to be

$$\frac{dQ_1}{dB} = -Q_1 + Q \tag{5.26}$$

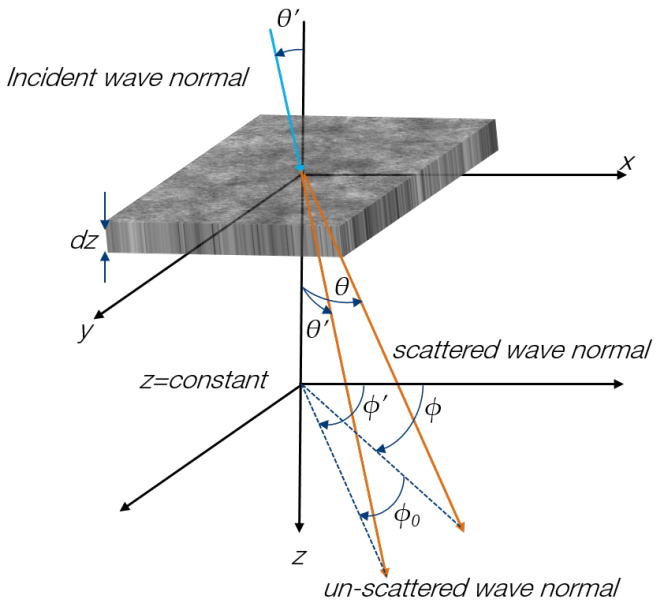

Figure 5.14: Geometry of wave scattering in a slice of material. Figure is regenerated after Ref. [195].

Similary, power density Q_n for n times scattering wave is

$$\frac{dQ_n}{dB} = -Q_n + Q_{n-1} \tag{5.27}$$

Knopoff et al. worked out the solution [196] that the leading term is $\tau^{-1} \propto \omega^2$ for short wavelengths approximation and the next term varies as ω^0.

CHAPTER 6

CONCLUSION AND FUTURE WORK

In this dissertation, we have investigated the thermoelectric properties of porous silicon nanowire which was fabricated from degenerately doped p-type silicon by a electroless etching method namely MacEtch (metal assisted chemical etch). We mainly focused on improving its electrical performance by post-doping while preserving its ultra low thermal conductivity and high Seebeck coefficient. Using a frequency domain measurement technique, we simultaneously characterized thermal conductivity and Seebeck coefficient of porous silicon nanowire arrays. At the same time, we have applied various methods including I-V test and Raman spectroscopy to explore the electrical transport properties at different doping conditions. Electrical and thermal transport in such a highly disordered system is a complex process and yet not well understood. We interpreted the measured data based on charge carrier and phonon transport theory and hope to gain insight into the transport phenomena in porous nanostructure. In this chapter, we will not only summarize our key observations and conclusions but also briefly discuss the future directions for potential application.

MacEtch method has the advantage that nanowire can be fast and massively fabricated. In order to fabricate an etching template, we performed rapid thermal annealing a thin silver film and produced isolated silver particles which were later served as a lift-off mask for gold. Though this procedure does not require sophisticated steps and delicate operation, the major drawback comes from the fact that dewetting is a random process. Uniform and complete lift-off of gold film is key to the success of nanowire fabrication, this requires accurate control of silver particle size as well as gold film thickness and grain size. Moreover the varied working condition of metal evaporation equipment we were using imposed more challenges. Although we may empir-

ically estimate from color change, except checking with SEM we still lack a reliable and fast method to evaluate the dewetting and lift-off process. As a result, we need to carefully calibrate the fabrication recipe through extensively fabrication trials and SEM characterization. Also the irregular *celery* like cross section due to the randomness of gold etching mask introduces more error into properties characterization especially single wire measurement.

In porous nanowire fabrication specifically, we can roughly control the porosity and pore size by changing the HF to H_2O_2 ratio [85], and we can also control the etching rate by temperature. By transmission electron microscope (TEM) we are able to verify the porous structure and nanowire remains crystalline. However TEM image is a projection of crystal planes, we could not precisely determine the pore/nanocrystalline size and porosity. High resolution SEM image of wire top view provides us some intuitive understanding of the pore morphology. We also estimated the crystalline size by analyzing the Raman spectrum using a phonon confinement model, however several assumptions have to be made. BET method is the only known way for porosity determination of nanowires, however it requires more than 15 mg samples. An accurate porosity value would be beneficial for understanding the transport process.

To enhance the electrical conductivity of porous silicon nanowire, we conducted post-doping. Post doping temperature set the achievable carrier concentration via boron solubility and time determines the uniformity of doping profile. We characterized the doping concentration by secondary ion mass spectroscopy (SIMS). Surprisingly, the post-doped nanowire has larger doping concentration than the boron solubility at corresponding doping temperature. This was also observed elsewhere and interpreted by formation of boron silicon cluster [154]. We chose a doping temperature from $800 \sim 950$ °C at which boron solubility exceeds the substrate doping concentration. By two-point probe I-V measurement on the nanowire array, we discovered that sample post doped at 900 °C and 950 °C showed increased conductivity. The increment for 900 °C is at least one order and three orders for 950 °C doped sample. One apparent reason for the enhancement of electrical conductivity is increased doping atoms. However this is not the only reason. The carrier

mobility also seems increased after post doping. It is possible that the post doping procedure reduces the activation energy, or weaken the trapping effect due to surface states. Possible geometrical change may also improve the electrical conductivity. The actual mechanism remains unknown and needs deeply investigation.

In this work, we also applied Raman spectroscopy and developed the method of extracting carrier concentration and size information. Raman spectroscopy is a fast and non-destructive method, however the spectrum is affected by different effects such as temperature, impurity, size, strain and etc. By careful choice of incident laser power we can minimize the heating effect. We mainly attribute the Raman spectrum broadening and peak shift to a combination of size induced phonon confinement and free carrier effect. The key assumption in our Raman analysis is that different effects are independent. As a result, we directly fit the spectrum with phonon confinement model and extract natural width Γ_0 and size of nano crystalline. This Γ_0 should be purely due to free carrier based on our assumption. We currently only compare this spectrum width with literature data on bulk doped silicon. The most precise procedure however should be comparison with calibrated bulk silicon spectrum data of the same Raman system. We found good agreement in carrier concentration estimation between the Raman spectrum approach and fitting of Seebeck coefficient by Mott formula. As to the nanocrystalline size determination, the phonon confinement model has its limitation mainly comes from the phonon confinement constant β which greatly affects the spectrum shape. Various values of β have been reported in literature and there is no clear physical meaning of this parameter. As a result, the extracted size information may only serve as a reference. We applied the most commonly used value $\beta = 2\sqrt{2}\pi$ in current work.

The simultaneous measurement of thermal conductivity and Seebeck coefficient of nanowire array is developed from the 3ω technique. Compared with traditional DC measurement, open circuit Seebeck voltage and temperature increase have distinct frequency response and thus we are able to exclude the side contribution, such as contact. We also briefly discussed the limitation of this technique due to finite heater dimension and thermal wave

penetration depth. When measuring highly resistive material such as our as-etched nanowire, Seebeck voltage $V_{2\omega}$ has large phase shift compared with the temperature increase $\Delta T_{2\omega}$ and can result in big error. In such a system, it would be beneficial to use shorter wire/thinner film. Consistent heater resistance temperature calibration is a crucial step for minimizing the measurement error. We calibrated the heater resistance during the measurement and thus this real-time calibration better represent the temperature response.

Our measured Seebeck coefficient of porous wire show distinct diffusion contribution. In nanowire system, phonon drag contribution to Seebeck coefficient S_{ph} is quenched [20]. We interpreted the data by both Mott formula and diffusion component S_d calculation. We assumed energy dependent scattering as $\Lambda \propto E^r$ which can also be used for mobility calculation. As-etched nanowire has similar Seebeck coefficient as the bulk substrate. By analyzing S and σ at the same time, we extracted $r = 2.7$ for carrier concentration $n = 1.3 \times 10^{19}$ cm^{-3}. The high scattering energy parameter may indicate the enhanced scattering in as-etched porous wire. Seebeck coefficient of 950 °C doped porous wire has metallic behaviour due to its high carrier concentration and we extract it to be 1.6×10^{20} cm^{-3} and this agrees very well with our Raman spectrum analysis. We obtained $r = 0$ and this reveals that the dominant electron scattering mechanism in 950 °C is via acoustic deformation potential. For porous nanowire post doped at 900 °C, it has metallic behaviour above 50 K. By fitting the metallic region we estimated the carrier concentration to be 4.5×10^{19} cm^{-3} which is also in good agreement with Raman analysis. A value of $r = 0.7$ showed that electrons are scattered more strongly than in the wire post-doped at 950 °C. The low temperature data still requires more investigation and it may still include phonon drag contribution.

In order to understand the ultra low thermal conductivity in porous silicon nanowire, we mainly focused on modeling of phonon nanocrystalline scattering. At low temperature, $k \propto T^{1.8}$ may suggest $\tau^{-1} \propto \omega^2$ for phonon pore multiple scattering. Although thermal conductivity temperature trend is similar to the amorphous limit model prediction, we were unable to explain the values based on physical assumptions using this model. Previous work

on wave multiple scattering also showed ω^2 frequency dependence and we are still working on the formulation in porous nanowire. Moreover, thermal conductivity fitting of post-doped nanowire may suggest much large electrical conductivity.

Throughout our characterization, we demonstrated the potential of using porous silicon nanowire for thermoelectric application. However to make a device for practical power generation, we have to solve the many engineering challenges such as heat exchanger design, nanowire assembling. One aspect that is related to current research is to improve the metal/nanowire tip contact. With good electrical contact we can greatly reduce the power loss. One possible direction is applying an additional tip doping step as described in Ref. [29]. The tip doping requires an additional SOG fill step which requires accurate control of exposed tip length. Another possible direction is to optimize the contact annealing recipe, we should be aware of the silicide formation speed if higher temperature is used. The study on post-doping is also relevant for other applications of porous silicon structures.

APPENDIX A

DEPOSITION AND ETCHING RATE

Accurate control of dielectric film deposition and etching is key to the success of fabrication. We have used PlasmaLab PECVD and Trion Minilock-Orion PECVD System for oxide deposition and STS Mixed-Frequency Nitride PECVD System for nitride deposition. We should always have a dummy during deposition which will be later used to measure the film thickness. The Deposition recipes we were using are:

- PlasmaLab: 6.7% power, 1000 mTorr throttle pressure, 18.6% gas flow
- Trion Minilock-Orion: low-dep recipe
- STS: (mixed frequency) 650 mTorr throttle pressure, platen temperature 300 °C, shower head temperature 240 °C; N_2, SiH_4 and NH_3 flow rate 1960 sccm, 40 sccm and 35 sccm repectively; power is 20 W.

In Seebeck measurement platform fabrication, we used dry etching by PlasmaTherm Freon RIE in Frederick Seitz Material Research Laboratory (MRL). The etching recipe was: 30 sccm CF_4 flow rate, 35 mTorr throtle pressure and 100 W etching power. The calibrated etching rate was shown in Table. A.2

In single wire electrical measurement, we mainly applied wet etching. The etching rates by 10:1 BOE under room temperature were also calibrated, as

Table A.1: PECVD SiO_2 and SiN_x film deposition rate.

Material	**Deposition Rate nm/min**
SiO_2 (PlasmaLab)	∼11.6
SiO_2 (Trion)	36∼37
SiN_x (STS, MF)	12.2∼12.7

Table A.2: Dry etching rate by CF_4.

Etched Material	**Etch Rate nm/min**
SiO_2	∼21
SOG (cured at 350 °C)	∼55
SiN_x (MF)	∼60

Table A.3: Wet etching rate by 10:1 BOE at room termperature.

Etched Material	**Etch Rate nm/min**
SiO_2 (PlasmaLab)	∼92
SiO_2 (Trion)	∼78
SiN_x (MF)	∼23

shown in Table. A.3

The rate listed above can be used as a reference but certain tolerance should be considered. Since working condition of the equipment varies, it is highly suggested to recalibrate the rate.

APPENDIX B

SOG ELLIPSOMETRY

The SOG used in our experiment was Filmtronics® 500F, spin coating recipe were described in Section 3.2.3 and resulting film thickness on silicon wafer was about 1167 nm. Ellipsometry measurement was conducted on a Woollam VASE® Ellipsometer. We also measure the thickness by viewing the cross section SEM and found good agreement. SOG was cured at 350 °C in N_2 atmosphere. We found that ellipsometry measurement of SOG thickness was insensitive to the extinction coefficient κ, and hence we can set it to zero. The refractive index of SOG for wavelength between 300 nm and 800 nm was shown in Fig. B.1

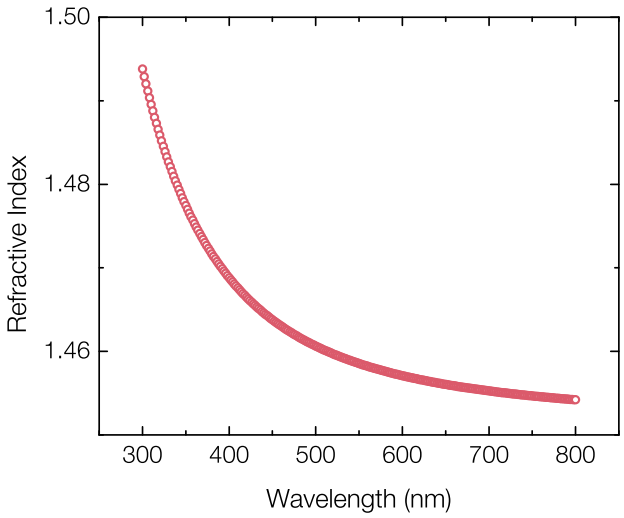

Figure B.1: Refractive index of SOG at different wavelength.

REFERENCES

[1] Lawrence Livermore National Laboratory, "US energy flow chart." [Online]. Available: https://flowcharts.llnl.gov/

[2] C. B. Vining, "An inconvenient truth about thermoelectrics," *Nature Materials*, vol. 8, no. 2, pp. 83–85, 2009. [Online]. Available: http://dx.doi.org/10.1038/nmat2361

[3] J. P. Heremans, M. S. Dresselhaus, L. E. Bell, and D. T. Morelli, "When thermoelectrics reached the nanoscale," *Nature Nanotechnology*, vol. 8, no. 7, pp. 471–473, 2013. [Online]. Available: http://dx.doi.org/10.1038/nnano.2013.129

[4] G. J. Snyder and T. S. Ursell, "Thermoelectric efficiency and compatibility," *Physical Review Letters*, vol. 91, no. 14, p. 148301, 2003. [Online]. Available: http://dx.doi.org/10.1103/PhysRevLett.91.148301

[5] G. Chen, *Nanoscale Energy Transport and Conversion : A Parallel Treatment of Electrons, Molecules, Phonons, and Photons*. Oxford University Press, USA, 2005.

[6] G. J. Snyder and E. S. Toberer, "Complex thermoelectric materials," *Nature Materials*, vol. 7, no. 2, pp. 105–114, 2008. [Online]. Available: http://dx.doi.org/10.1038/nmat2090

[7] L. D. Hicks and M. S. Dresselhaus, "Thermoelectric figure of merit of a one-dimensional conductor," *Physical Review B*, vol. 47, no. 24, pp. 16 631–16 634, 1993. [Online]. Available: http://link.aps.org/doi/10.1103/PhysRevB.47.16631

[8] L. D. Hicks and M. S. Dresselhaus, "Effect of quantum-well structures on the thermoelectric figure of merit," *Physical Review B*, vol. 47, no. 19, pp. 12 727–12 731, 1993. [Online]. Available: http://link.aps.org/doi/10.1103/PhysRevB.47.12727

[9] J. P. Heremans, C. M. Thrush, D. T. Morelli, and M.-C. Wu, "Thermoelectric power of bismuth nanocomposites," *Physical Review*

Letters, vol. 88, no. 21, p. 216801, 2002. [Online]. Available: http://dx.doi.org/10.1103/PhysRevLett.88.216801

[10] R. Venkatasubramanian, E. Siivola, T. Colpitts, and B. O'Quinn, "Thin-film thermoelectric devices with high room-temperature figures of merit," *Nature*, vol. 413, no. 6856, pp. 597–602, 2001. [Online]. Available: http://dx.doi.org/10.1038/35098012

[11] T. C. Harman, P. J. Taylor, M. P. Walsh, and B. E. LaForge, "Quantum dot superlattice thermoelectric materials and devices," *Science*, vol. 297, no. 5590, pp. 2229–2232, 2002. [Online]. Available: http://www.sciencemag.org/content/297/5590/2229

[12] M. S. Dresselhaus, G. Chen, M. Y. Tang, R. G. Yang, H. Lee, D. Z. Wang, Z. F. Ren, J. P. Fleurial, and P. Gogna, "New directions for low-dimensional thermoelectric materials," *Advanced Materials*, vol. 19, no. 8, pp. 1043–1053, 2007. [Online]. Available: http://dx.doi.org/10.1002/adma.200600527

[13] A. J. Minnich, M. S. Dresselhaus, Z. F. Ren, and G. Chen, "Bulk nanostructured thermoelectric materials: current research and future prospects," *Energy & Environmental Science*, vol. 2, no. 5, pp. 466–479, 2009. [Online]. Available: http://dx.doi.org/10.1039/B822664B

[14] C. J. Vineis, A. Shakouri, A. Majumdar, and M. G. Kanatzidis, "Nanostructured thermoelectrics: Big efficiency gains from small features," *Advanced Materials*, vol. 22, no. 36, pp. 3970–3980, 2010. [Online]. Available: http://dx.doi.org/10.1002/adma.201000839

[15] K. Nielsch, J. Bachmann, J. Kimling, and H. Böttner, "Thermoelectric nanostructures: From physical model systems towards nanograined composites," *Advanced Energy Materials*, vol. 1, no. 5, pp. 713–731, 2011. [Online]. Available: http://dx.doi.org/10.1002/aenm.201100207

[16] A. Shakouri, "Recent developments in semiconductor thermoelectric physics and materials," *Annual Review of Materials Research*, vol. 41, no. 1, pp. 399–431, 2011. [Online]. Available: http://www.annualreviews.org/doi/abs/10.1146/annurev-matsci-062910-100445

[17] K. Esfarjani, G. Chen, and H. T. Stokes, "Heat transport in silicon from first-principles calculations," *Physical Review B*, vol. 84, no. 8, p. 085204, 2011. [Online]. Available: http://dx.doi.org/10.1103/PhysRevB.84.085204

[18] A. J. Minnich, J. A. Johnson, A. J. Schmidt, K. Esfarjani, M. S. Dresselhaus, K. A. Nelson, and G. Chen, "Thermal conductivity spectroscopy technique to measure phonon mean free paths," *Physical Review Letters*, vol. 107, no. 9, p. 095901, 2011, pRL. [Online]. Available: http://dx.doi.org/10.1103/PhysRevLett.107.095901

[19] K. T. Regner, D. P. Sellan, Z. Su, C. H. Amon, A. J. H. McGaughey, and J. A. Malen, "Broadband phonon mean free path contributions to thermal conductivity measured using frequency domain thermoreflectance," *Nature Communication*, vol. 4, p. 1640, 2013. [Online]. Available: http://www.nature.com/ncomms/journal/v4/n3/full/ncomms2630.html

[20] J. S. Sadhu, "Effect of phonon transport on the seebeck coefficient and thermal conductivity of silicon nanowire arrays," PhD Dissertation, 2013.

[21] J. Ma and S. Sinha, "Thermoelectric properties of highly doped n-type polysilicon inverse opals," *Journal of Applied Physics*, vol. 112, no. 7, p. 073719, 2012. [Online]. Available: http://dx.doi.org/10.1063/1.4758382

[22] H. B. G. Casimir, "Note on the conduction of heat in crystals," *Physica*, vol. 5, no. 6, pp. 495–500, 1938. [Online]. Available: http://www.sciencedirect.com/science/article/pii/S0031891438801622

[23] A. I. Boukai, Y. Bunimovich, J. Tahir-Kheli, J.-K. Yu, W. A. Goddard Iii, and J. R. Heath, "Silicon nanowires as efficient thermoelectric materials," *Nature*, vol. 451, no. 7175, pp. 168–171, 2008. [Online]. Available: http://dx.doi.org/10.1038/nature06458

[24] A. I. Hochbaum, R. Chen, R. D. Delgado, W. Liang, E. C. Garnett, M. Najarian, A. Majumdar, and P. Yang, "Enhanced thermoelectric performance of rough silicon nanowires," *Nature*, vol. 451, no. 7175, pp. 163–167, 2008. [Online]. Available: http://dx.doi.org/10.1038/nature06381

[25] D. Li, Y. Wu, P. Kim, L. Shi, P. Yang, and A. Majumdar, "Thermal conductivity of individual silicon nanowires," *Applied Physics Letters*, vol. 83, no. 14, pp. 2934–2936, 2003. [Online]. Available: http://scitation.aip.org/content/aip/journal/apl/83/14/10.1063/1.1616981

[26] R. Chen, A. I. Hochbaum, P. Murphy, J. Moore, P. Yang, and A. Majumdar, "Thermal conductance of thin silicon nanowires," *Physical Review Letters*, vol. 101, no. 10, p. 105501, 2008. [Online]. Available: http://link.aps.org/doi/10.1103/PhysRevLett.101.105501

[27] M. G. Ghossoub, K. V. Valavala, M. Seong, B. Azeredo, K. Hsu, J. S. Sadhu, P. K. Singh, and S. Sinha, "Spectral phonon scattering from sub-10 nm surface roughness wavelengths in metal-assisted chemically etched Si nanowires," *Nano Letters*, vol. 13, no. 4, pp. 1564–1571, 2013. [Online]. Available: http://dx.doi.org/10.1021/nl3047392

[28] J.-K. Yu, S. Mitrovic, D. Tham, J. Varghese, and J. R. Heath, "Reduction of thermal conductivity in phononic nanomesh

structures," *Nature Nanotechnology*, vol. 5, no. 10, pp. 718–721, 2010. [Online]. Available: http://www.nature.com/nnano/journal/v5/n10/full/nnano.2010.149.html

[29] S. S. Jyothi, T. Hongxiang, S. Timothy, K. Junhwan, A. Bruno, F. Placid, and S. Sanjiv, "Controllable doping and wrap-around contacts to electrolessly etched silicon nanowire arrays," *Nanotechnology*, vol. 25, no. 37, p. 375701, 2014. [Online]. Available: http://stacks.iop.org/0957-4484/25/i=37/a=375701

[30] J. d. Boor, D. S. Kim, X. Ao, D. Hagen, A. Cojocaru, H. Föll, and V. Schmidt, "Temperature and structure size dependence of the thermal conductivity of porous silicon," *EPL (Europhysics Letters)*, vol. 96, no. 1, p. 16001, 2011. [Online]. Available: http://stacks.iop.org/0295-5075/96/i=1/a=16001

[31] A. G. Cullis and L. T. Canham, "Visible light emission due to quantum size effects in highly porous crystalline silicon," *Nature*, vol. 353, no. 6342, pp. 335–338, 1991. [Online]. Available: http://dx.doi.org/10.1038/353335a0

[32] A. G. Cullis, L. T. Canham, and P. D. J. Calcott, "The structural and luminescence properties of porous silicon," *Journal of Applied Physics*, vol. 82, no. 3, pp. 909–965, 1997. [Online]. Available: http://dx.doi.org/10.1063/1.366536

[33] O. Bisi, S. Ossicini, and L. Pavesi, "Porous silicon: a quantum sponge structure for silicon based optoelectronics," *Surface Science Reports*, vol. 38, no. 13, pp. 1–126, 2000. [Online]. Available: http://www.sciencedirect.com/science/article/pii/S0167572999000126

[34] R. G. Mathur, R. M. Mehra, and P. C. Mathur, "Thermoelectric power in porous silicon," *Journal of Applied Physics*, vol. 83, no. 11, pp. 5855–5857, 2000. [Online]. Available: http://dx.doi.org/10.1063/1.367444

[35] A. Yamamoto, H. Takazawa, and T. Ohta, "Thermoelectric transport properties of porous silicon nanostructure," in *Thermoelectrics, 1999. Eighteenth International Conference on*, pp. 428–431.

[36] J.-H. Lee, G. A. Galli, and J. C. Grossman, "Nanoporous Si as an efficient thermoelectric material," *Nano Letters*, vol. 8, no. 11, pp. 3750–3754, 2008. [Online]. Available: http://dx.doi.org/10.1021/nl802045f

[37] J. Tang, H.-T. Wang, D. H. Lee, M. Fardy, Z. Huo, T. P. Russell, and P. Yang, "Holey silicon as an efficient thermoelectric material," *Nano Letters*, vol. 10, no. 10, pp. 4279–4283, 2010. [Online]. Available: http://dx.doi.org/10.1021/nl102931z

[38] D. Song and G. Chen, "Thermal conductivity of periodic microporous silicon films," *Applied Physics Letters*, vol. 84, no. 5, pp. 687–689, 2004. [Online]. Available: http://scitation.aip.org/content/aip/journal/apl/84/5/10.1063/1.1642753

[39] L. Shi, D. Li, C. Yu, W. Jang, D. Kim, Z. Yao, P. Kim, and A. Majumdar, "Measuring thermal and thermoelectric properties of one-dimensional nanostructures using a microfabricated device," *Journal of Heat Transfer*, vol. 125, no. 5, pp. 881–888, 2003, 10.1115/1.1597619.

[40] P. E. Hopkins, C. M. Reinke, M. F. Su, R. H. Olsson, E. A. Shaner, Z. C. Leseman, J. R. Serrano, L. M. Phinney, and I. El-Kady, "Reduction in the thermal conductivity of single crystalline silicon by phononic crystal patterning," *Nano Letters*, vol. 11, no. 1, pp. 107–112, 2010. [Online]. Available: http://dx.doi.org/10.1021/nl102918q

[41] A. M. Marconnet, T. Kodama, M. Asheghi, and K. E. Goodson, "Phonon conduction in periodically porous silicon nanobridges," *Nanoscale and Microscale Thermophysical Engineering*, vol. 16, no. 4, pp. 199–219, 2012. [Online]. Available: http://dx.doi.org/10.1080/15567265.2012.732195

[42] J. Fang, C. B. Kang, Y. Huang, S. H. Tolbert, and L. Pilon, "Thermal conductivity of ordered mesoporous nanocrystalline silicon thin films made from magnesium reduction of polymer-templated silica," *The Journal of Physical Chemistry C*, vol. 116, no. 23, pp. 12 926–12 933, 2012. [Online]. Available: http://dx.doi.org/10.1021/jp302531d

[43] J. Ma, B. R. Parajuli, M. G. Ghossoub, A. Mihi, J. Sadhu, P. V. Braun, and S. Sinha, "Coherent phonon-grain boundary scattering in silicon inverse opals," 2013. [Online]. Available: http://dx.doi.org/10.1021/nl304190s

[44] J.-H. Lee, J. C. Grossman, J. Reed, and G. Galli, "Lattice thermal conductivity of nanoporous Si: Molecular dynamics study," *Applied Physics Letters*, vol. 91, no. 22, p. 223110, 2007. [Online]. Available: http://scitation.aip.org/content/aip/journal/apl/91/22/10.1063/1.2817739

[45] L. Yang, N. Yang, and B. Li, "Extreme low thermal conductivity in nanoscale 3D Si phononic crystal with spherical pores," *Nano Letters*, vol. 14, no. 4, pp. 1734–1738, 2014. [Online]. Available: http://pubs.acs.org/doi/abs/10.1021/nl403750s

[46] A. Jain, Y.-J. Yu, and A. J. H. McGaughey, "Phonon transport in periodic silicon nanoporous films with feature sizes greater than 100 nm," *Physical Review B*, vol. 87, no. 19, p. 195301, 2013. [Online]. Available: http://link.aps.org/doi/10.1103/PhysRevB.87.195301

[47] N. K. Ravichandran and A. J. Minnich, "Coherent and incoherent thermal transport in nanomeshes," *Physical Review B*, vol. 89, no. 20, p. 205432, 2014. [Online]. Available: http://link.aps.org/doi/10.1103/PhysRevB.89.205432

[48] X. Li and P. W. Bohn, "Metal-assisted chemical etching in hf/h2o2 produces porous silicon," *Applied Physics Letters*, vol. 77, no. 16, pp. 2572–2574, 2000. [Online]. Available: http://scitation.aip.org/content/aip/journal/apl/77/16/10.1063/1.1319191

[49] L. Canham, *Properties of Porous Silicon*. INSPEC, The Institution of Electrical Engineers, London, UK, 1997.

[50] J. Rouquerol, D. Avnir, C. W. Fairbridge, D. H. Everett, J. M. Haynes, N. Pernicone, J. D. F. Ramsay, K. S. W. Sing, and K. K. Unger, "Recommendations for the characterization of porous solids (technical report)," Tech. Rep. 8, 1994.

[51] V. Lysenko, S. Périchon, B. Remaki, and D. Barbier, "Thermal isolation in microsystems with porous silicon," *Sensors and Actuators A: Physical*, vol. 99, no. 12, pp. 13–24, 2002. [Online]. Available: http://www.sciencedirect.com/science/article/pii/S0924424701008810

[52] W. Lang, A. Drost, P. Steiner, and H. Sandmaier, "The thermal conductivity of porous silicon," *MRS Online Proceedings Library*, vol. 358, pp. null–null, 1994. [Online]. Available: http://dx.doi.org/10.1557/PROC-358-561

[53] G. Gesele, J. Linsmeier, V. Drach, J. Fricke, and R. Arens-Fischer, "Temperature-dependent thermal conductivity of porous silicon," *Journal of Physics D: Applied Physics*, vol. 30, no. 21, p. 2911, 1997. [Online]. Available: http://stacks.iop.org/0022-3727/30/i=21/a=001

[54] G. Benedetto, L. Boarino, and R. Spagnolo, "Evaluation of thermal conductivity of porous silicon layers by a photoacoustic method," *Applied Physics A*, vol. 64, no. 2, pp. 155–159, 1997. [Online]. Available: http://dx.doi.org/10.1007/s003390050457

[55] U. Bernini, P. Maddalena, E. Massera, and A. Ramaglia, "Thermal characterization of porous silicon via thermal wave interferometry," *Optics Communications*, vol. 168, no. 14, pp. 305–314, 1999. [Online]. Available: http://www.sciencedirect.com/science/article/pii/S0030401899003193

[56] V. Lysenko, S. Périchon, B. Remaki, D. Barbier, and B. Champagnon, "Thermal conductivity of thick meso-porous silicon layers by micro-Raman scattering," *Journal of Applied Physics*, vol. 86, no. 12, pp. 6841–6846, 1999. [Online]. Available: http://dx.doi.org/10.1063/1.371760

[57] V. Lysenko and S. Volz, "Porous silicon thermal conductivity by scanning probe microscopy," *physica status solidi (a)*, vol. 182, no. 2, pp. R6–R7, 2000.

[58] S. Périchon, V. Lysenko, P. Roussel, B. Remaki, B. Champagnon, D. Barbier, and P. Pinard, "Technology and micro-Raman characterization of thick meso-porous silicon layers for thermal effect microsystems," *Sensors and Actuators A: Physical*, vol. 85, no. 13, pp. 335–339, 2000. [Online]. Available: http://www.sciencedirect.com/science/article/pii/S0924424700003277

[59] U. Bernini, S. Lettieri, P. Maddalena, R. Vitiello, and G. D. Francia, "Evaluation of the thermal conductivity of porous silicon layers by an optical pump-probe method," *Journal of Physics: Condensed Matter*, vol. 13, no. 5, p. 1141, 2001. [Online]. Available: http://stacks.iop.org/0953-8984/13/i=5/a=327

[60] Q. Shen and T. Toyoda, "Dependence of thermal conductivity of porous silicon on porosity characterized by photoacoustic technique," *Review of Scientific Instruments*, vol. 74, no. 1, pp. 601–603, 2003. [Online]. Available: http://scitation.aip.org/content/aip/journal/rsi/74/1/10.1063/1.1515897

[61] S. Lettieri, U. Bernini, E. Massera, and P. Maddalena, "Optical investigations on thermal conductivity in n- and p-type porous silicon," *physica status solidi (c)*, vol. 2, no. 9, pp. 3414–3418, 2005. [Online]. Available: http://dx.doi.org/10.1002/pssc.200461194

[62] A. Wolf and R. Brendel, "Thermal conductivity of sintered porous silicon films," *Thin Solid Films*, vol. 513, no. 12, pp. 385–390, 2006. [Online]. Available: http://www.sciencedirect.com/science/article/pii/S0040609006002094

[63] S. Gomès, L. David, V. Lysenko, A. Descamps, T. Nychyporuk, and M. Raynaud, "Application of scanning thermal microscopy for thermal conductivity measurements on meso-porous silicon thin films," *Journal of Physics D: Applied Physics*, vol. 40, no. 21, p. 6677, 2007. [Online]. Available: http://stacks.iop.org/0022-3727/40/i=21/a=029

[64] R. Srinivasan, M. Jayachandran, and K. Ramachandran, "Photoacoustic studies on optical and thermal properties of p-type and n-type nanostructured porous silicon for (100) and (111) orientations," *Crystal Research and Technology*, vol. 42, no. 3, pp. 266–274, 2007. [Online]. Available: http://dx.doi.org/10.1002/crat.200610811

[65] J. Weisse, A. Marconnet, D. Kim, P. Rao, M. Panzer, K. Goodson, and X. Zheng, "Thermal conductivity in porous silicon nanowire arrays,"

Nanoscale Research Letters, vol. 7, no. 1, p. 554, 2012. [Online]. Available: http://www.nanoscalereslett.com/content/7/1/554

[66] K. Valalaki and A. G. Nassiopoulou, "Low thermal conductivity porous si at cryogenic temperatures for cooling applications," *Journal of Physics D: Applied Physics*, vol. 46, no. 29, p. 295101, 2013. [Online]. Available: http://stacks.iop.org/0022-3727/46/i=29/a=295101

[67] J. D. Chung and M. Kaviany, "Effects of phonon pore scattering and pore randomness on effective conductivity of porous silicon," *International Journal of Heat and Mass Transfer*, vol. 43, no. 4, pp. 521–538, 2000. [Online]. Available: http://www.sciencedirect.com/science/article/pii/S0017931099001659

[68] J. Randrianalisoa and D. Baillis, "Monte carlo simulation of cross-plane thermal conductivity of nanostructured porous silicon films," *Journal of Applied Physics*, vol. 103, no. 5, p. 053502, 2008. [Online]. Available: http://dx.doi.org/10.1063/1.2841697

[69] J. Randrianalisoa and D. Baillis, "Combined analytical and phonon-tracking approaches to model thermal conductivity of etched and annealed nanoporous silicon," *Advanced Engineering Materials*, vol. 11, no. 10, pp. 852–861, 2009. [Online]. Available: http://dx.doi.org/10.1002/adem.200900136

[70] G. Polisski, G. Dollinger, A. Bergmaier, D. Kovalev, H. Heckler, and F. Koch, "Acceptor depletion in p-type porous silicon," *physica status solidi (a)*, vol. 168, no. 1, pp. R1–R2, 1998.

[71] M. Ben-Chorin, F. Möller, F. Koch, W. Schirmacher, and M. Eberhard, "Hopping transport on a fractal: AC conductivity of porous silicon," *Physical Review B*, vol. 51, no. 4, pp. 2199–2213, 1995. [Online]. Available: http://dx.doi.org/10.1103/PhysRevB.51.2199

[72] Y. Lubianiker and I. Balberg, "Two Meyer-Neldel rules in porous silicon," *Physical Review Letters*, vol. 78, no. 12, pp. 2433–2436, 1997. [Online]. Available: http://dx.doi.org/10.1103/PhysRevLett.78.2433

[73] L. Pavesi, R. Chierchia, P. Bellutti, A. Lui, F. Fuso, M. Labardi, L. Pardi, F. Sbrana, M. Allegrini, S. Trusso, C. Vasi, P. J. Ventura, L. C. Costa, M. C. Carmo, and O. Bisi, "Light emitting porous silicon diode based on a silicon/porous silicon heterojunction," *Journal of Applied Physics*, vol. 86, no. 11, pp. 6474–6482, 1999. [Online]. Available: http://dx.doi.org/10.1063/1.371711

[74] G. Di Francia, V. La Ferrara, P. Maddalena, D. Ninno, L. P. Odierna, and V. Cataudella, "AC conductivity of porous silicon: A fractal and surface transport mechanism?" *Il Nuovo Cimento D*, vol. 18, no. 10, pp. 1187–1196, 1996.

[75] R. Schwarz, F. Wang, M. Ben-Chorin, S. Grebner, A. Nikolov, and F. Koch, "Photocarrier grating technique in mesoporous silicon," *Thin Solid Films*, vol. 255, no. 12, pp. 23–26, 1995.

[76] E. A. Lebedev, E. A. Smorgonskaya, and G. Polisski, "Drift mobility of excess carriers in porous silicon," *Physical Review B*, vol. 57, no. 23, pp. 14 607–14 610, 1998. [Online]. Available: http://dx.doi.org/10.1103/PhysRevB.57.14607

[77] P. N. Rao, E. A. Schiff, L. Tsybeskov, and P. Fauchet, "Photocarrier drift-mobility measurements and electron localization in nanoporous silicon," *Chemical Physics*, vol. 284, no. 12, pp. 129–138, 2002. [Online]. Available: http://www.sciencedirect.com/science/article/pii/S030101040200544X

[78] Z. Huang, N. Geyer, P. Werner, J. de Boor, and U. Gsele, "Metal-assisted chemical etching of silicon: A review," *Advanced Materials*, vol. 23, no. 2, pp. 285–308, 2011. [Online]. Available: http://dx.doi.org/10.1002/adma.201001784

[79] S. Cruz, A. Hnig-dOrville, and J. Mller, "Fabrication and optimization of porous silicon substrates for diffusion membrane applications," *Journal of The Electrochemical Society*, vol. 152, no. 6, pp. C418–C424, 2005. [Online]. Available: http://jes.ecsdl.org/content/152/6/C418.abstract

[80] M. Schade, N. Geyer, B. Fuhrmann, F. Heyroth, and H. S. Leipner, "High-resolution analytical electron microscopy of catalytically etched silicon nanowires," *Applied Physics A*, vol. 95, no. 2, pp. 325–327, 2009. [Online]. Available: http://dx.doi.org/10.1007/s00339-009-5101-x

[81] A. I. Hochbaum, D. Gargas, Y. J. Hwang, and P. Yang, "Single crystalline mesoporous silicon nanowires," *Nano Letters*, vol. 9, no. 10, pp. 3550–3554, 2009. [Online]. Available: http://dx.doi.org/10.1021/nl9017594http://pubs.acs.org/doi/pdfplus/10.1021/nl9017594

[82] K. Peng, M. Zhang, A. Lu, N.-B. Wong, R. Zhang, and S.-T. Lee, "Ordered silicon nanowire arrays via nanosphere lithography and metal-induced etching," *Applied Physics Letters*, vol. 90, no. 16, p. 163123, 2007. [Online]. Available: http://scitation.aip.org/content/aip/journal/apl/90/16/10.1063/1.2724897

[83] Z. Huang, H. Fang, and J. Zhu, "Fabrication of silicon nanowire arrays with controlled diameter, length, and density," *Advanced Materials*, vol. 19, no. 5, pp. 744–748, 2007. [Online]. Available: http://dx.doi.org/10.1002/adma.200600892

[84] B. P. Azeredo, J. Sadhu, J. Ma, K. Jacobs, J. Kim, K. Lee, J. H. Eraker, X. Li, S. Sinha, N. Fang, P. Ferreira, and K. Hsu,

"Silicon nanowires with controlled sidewall profile and roughness fabricated by thin-film dewetting and metal-assisted chemical etching," *Nanotechnology*, vol. 24, no. 22, p. 225305, 2013. [Online]. Available: http://stacks.iop.org/0957-4484/24/i=22/a=225305

[85] K. Balasundaram, J. S. Sadhu, J. C. Shin, B. Azeredo, D. Chanda, M. Malik, K. Hsu, J. A. Rogers, P. Ferreira, S. Sinha, and X. Li, "Porosity control in metal-assisted chemical etching of degenerately doped silicon nanowires," *Nanotechnology*, vol. 23, no. 30, p. 305304, 2012. [Online]. Available: http://stacks.iop.org/0957-4484/23/i=30/a=305304

[86] K. E. Moselund, H. Ghoneim, H. Schmid, M. T. Bjrk, E. Lrtscher, S. Karg, G. Signorello, D. Webb, M. Tschudy, R. Beyeler, and H. Riel, "Solid-state diffusion as an efficient doping method for silicon nanowires and nanowire field effect transistors," *Nanotechnology*, vol. 21, no. 43, p. 435202, 2010. [Online]. Available: http://dx.doi.org/10.1088/0957-4484/21/43/435202

[87] W. Chen, V. G. Dubrovskii, X. Liu, T. Xu, R. Lardé, J. Philippe Nys, B. Grandidier, D. Stiévenard, G. Patriarche, and P. Pareige, "Boron distribution in the core of Si nanowire grown by chemical vapor deposition," *Journal of Applied Physics*, vol. 111, no. 9, p. 094909, 2012. [Online]. Available: http://dx.doi.org/10.1063/1.4714364

[88] F. A. TRUMBORE, "Solid solubilities of impurity elements in germanium and silicon," *Bell System Technical Journal*, 1960.

[89] G. L. Vick and K. M. Whittle, "Solid solubility and diffusion coefficients of boron in silicon," *Journal of The Electrochemical Society*, vol. 116, no. 8, pp. 1142–1144, 1969. [Online]. Available: http://jes.ecsdl.org/content/116/8/1142.abstract

[90] H. Carslaw and J. Jaeger, *Conduction of heat in solids*, 2nd ed., ser. Oxford Science Publications. Oxford: Clarendon Press, 1959.

[91] D. G. Cahill, "Thermal conductivity measurement from 30 to 750 K: the 3ω method," *Review of Scientific Instruments*, vol. 61, no. 2, pp. 802–808, 1990. [Online]. Available: http://link.aip.org/link/?RSI/61/802/1

[92] B. Yang, J. L. Liu, K. L. Wang, and G. Chen, "Simultaneous measurements of seebeck coefficient and thermal conductivity across superlattice," *Applied Physics Letters*, vol. 80, no. 10, p. 1758, 2002. [Online]. Available: http://dx.doi.org/10.1063/1.1458693

[93] R. M. Costescu, A. J. Bullen, G. Matamis, K. E. O'Hara, and D. G. Cahill, "Thermal conductivity and sound velocities of hydrogen-silsesquioxane low-k dielectrics," *Physical Review B*,

vol. 65, no. 9, p. 094205, 2002. [Online]. Available: http://link.aps.org/doi/10.1103/PhysRevB.65.094205

[94] B. Curtin, E. Fang, and J. Bowers, "Highly ordered vertical silicon nanowire array composite thin films for thermoelectric devices," *Journal of Electronic Materials*, vol. 41, no. 5, pp. 887–894, 2012. [Online]. Available: http://dx.doi.org/10.1007/s11664-012-1904-1

[95] J. P. Feser, J. S. Sadhu, B. P. Azeredo, K. H. Hsu, J. Ma, J. Kim, M. Seong, N. X. Fang, X. Li, P. M. Ferreira, S. Sinha, and D. G. Cahill, "Thermal conductivity of silicon nanowire arrays with controlled roughness," *Journal of Applied Physics*, vol. 112, no. 11, p. 114306, 2012. [Online]. Available: http://dx.doi.org/10.1063/1.4767456

[96] H. Tian, M. G. Ghossoub, O. T. Baris, J. Ma, M. Tirumala, and S. Sinha, "Volumetric heat capacity enhancement in thin films of amorphous fluorocarbon polymers," *Journal of Heat Transfer*, vol. 134, no. 8, pp. 081 601–081 601, 2012, 10.1115/1.4006205. [Online]. Available: http://dx.doi.org/10.1115/1.4006205

[97] J. P. Feser, "Scalable routes to efficient thermoelectric materials," Ph.D. dissertation, 2010.

[98] M. G. Ghossoub, J.-H. Lee, O. T. Baris, D. G. Cahill, and S. Sinha, "Percolation of thermal conductivity in amorphous fluorocarbons," *Physical Review B*, vol. 82, no. 19, p. 195441, 2010. [Online]. Available: http://link.aps.org/doi/10.1103/PhysRevB.82.195441

[99] N. S. Dellas, C. J. Schuh, and S. E. Mohney, "Silicide formation in contacts to Si nanowires," *Journal of Materials Science*, vol. 47, no. 17, pp. 6189–6205, 2012. [Online]. Available: http://dx.doi.org/10.1007/s10853-012-6549-1

[100] J. Foggiato, W. S. Yoo, M. Ouaknine, T. Murakami, and T. Fukada, "Optimizing the formation of nickel silicide," *Materials Science and Engineering B*, vol. 114-115, pp. 56–60, 2004. [Online]. Available: http://dx.doi.org/10.1016/j.mseb.2004.07.033

[101] Y.-C. Lin, Y. Chen, D. Xu, and Y. Huang, "Growth of nickel silicides in Si and Si/SiO_x core/shell nanowires," *Nano Letters*, vol. 10, no. 11, pp. 4721–4726, 2010. [Online]. Available: http://dx.doi.org/10.1021/nl103156q

[102] R. M. Ranade, S. S. Ang, and W. D. Brown, "Reactive ion etching of thin gold films," *Journal of The Electrochemical Society*, vol. 140, no. 12, pp. 3676–3678, 1993. [Online]. Available: http://jes.ecsdl.org/content/140/12/3676.abstract

[103] F. Fracassi, R. d'Agostino, and A. Cacucci, "Dry etching of palladium thin films in fluorine containing plasmas: Xray photoelectron spectroscopy investigation," *Journal of Vacuum Science & Technology A*, vol. 13, no. 1, pp. 63–66, 1995. [Online]. Available: http://dx.doi.org/10.1116/1.579444

[104] H. H. Berger, "Models for contacts to planar devices," *Solid-State Electronics*, vol. 15, no. 2, pp. 145–158, 1972. [Online]. Available: http://www.sciencedirect.com/science/article/pii/0038110172900482

[105] E. G. Woelk, H. Krautle, and H. Beneking, "Measurement of low resistive ohmic contacts on semiconductors," *Electron Devices, IEEE Transactions on*, vol. 33, no. 1, pp. 19–22, 1986.

[106] V. Schmidt, J. V. Wittemann, and U. Gösele, "Growth, thermodynamics, and electrical properties of silicon nanowires," *Chemical Reviews*, vol. 110, no. 1, pp. 361–388, 2010. [Online]. Available: http://dx.doi.org/10.1021/cr900141g

[107] M. T. Bjork, H. Schmid, J. Knoch, H. Riel, and W. Riess, "Donor deactivation in silicon nanostructures," *Nature Nanotechnology*, vol. 4, no. 2, pp. 103–107, 2009. [Online]. Available: http://dx.doi.org/10.1038/nnano.2008.400

[108] H. Schmid, M. T. Björk, J. Knoch, S. Karg, H. Riel, and W. Riess, "Doping limits of grown in situ doped silicon nanowires using phosphine," *Nano Letters*, vol. 9, no. 1, pp. 173–177, 2008. [Online]. Available: http://dx.doi.org/10.1021/nl802739v

[109] V. Schmidt, S. Senz, and U. Gösele, "Influence of the Si/SiO_2 interface on the charge carrier density of Si nanowires," *Applied Physics A*, vol. 86, no. 2, pp. 187–191, 2007. [Online]. Available: http://dx.doi.org/10.1007/s00339-006-3746-2

[110] F. Cerdeira and M. Cardona, "Effect of carrier concentration on the Raman frequencies of Si and Ge," *Physical Review B*, vol. 5, no. 4, pp. 1440–1454, 1972. [Online]. Available: http://link.aps.org/doi/10.1103/PhysRevB.5.1440

[111] F. Cerdeira, T. A. Fjeldly, and M. Cardona, "Effect of free carriers on zone-center vibrational modes in heavily doped p-type Si. II. optical modes," *Physical Review B*, vol. 8, no. 10, pp. 4734–4745, 1973. [Online]. Available: http://link.aps.org/doi/10.1103/PhysRevB.8.4734

[112] F. Cerdeira, T. A. Fjeldly, and M. Cardona, "Interaction between electronic and vibronic Raman scattering in heavily doped silicon," *Solid State Communications*, vol. 13, no. 3, pp. 325–328, 1973. [Online]. Available: http://www.sciencedirect.com/science/article/pii/0038109873906029

[113] F. Cerdeira, T. A. Fjeldly, and M. Cardona, "Raman study of the interaction between localized vibrations and electronic excitations in boron-doped silicon," *Physical Review B*, vol. 9, no. 10, pp. 4344–4350, 1974. [Online]. Available: http://link.aps.org/doi/10.1103/PhysRevB.9.4344

[114] R. Beserman and T. Bernstein, "Raman scattering measurement of the free carrier concentration and of the impurity location in boron implanted silicon," *Journal of Applied. Physics*, vol. 48, no. 4, pp. 1548–1550, 1977. [Online]. Available: http://dx.doi.org/10.1063/1.323876

[115] M. Chandrasekhar, J. B. Renucci, and M. Cardona, "Effects of interband excitations on Raman phonons in heavily doped n-silicon," *Physical Review B*, vol. 17, no. 4, pp. 1623–1633, 1978. [Online]. Available: http://link.aps.org/doi/10.1103/PhysRevB.17.1623

[116] M. Chandrasekhar, H. R. Chandrasekhar, M. Grimsditch, and M. Cardona, "Study of the localized vibrations of boron in heavily doped Si," *Physical Review B*, vol. 22, no. 10, pp. 4825–4833, 1980. [Online]. Available: http://link.aps.org/doi/10.1103/PhysRevB.22.4825

[117] U. Fano, "Effects of configuration interaction on intensities and phase shifts," *Physical Review*, vol. 124, no. 6, pp. 1866–1878, 1961. [Online]. Available: http://link.aps.org/doi/10.1103/PhysRev.124.1866

[118] M. Becker, U. Gösele, A. Hofmann, and S. Christiansen, "Highly p-doped regions in silicon solar cells quantitatively analyzed by small angle beveling and micro-Raman spectroscopy," *Journal of Applied Physics*, vol. 106, no. 7, p. 074515, 2009. [Online]. Available: http://dx.doi.org/10.1063/1.3236571

[119] T. Kunz, M. T. Hessmann, S. Seren, B. Meidel, B. Terheiden, and C. J. Brabec, "Dopant mapping in highly p-doped silicon by micro-Raman spectroscopy at various injection levels," *Journal of Applied Physics*, vol. 113, no. 2, p. 023514, 2013. [Online]. Available: http://dx.doi.org/10.1063/1.4773110

[120] B. G. Burke, J. Chan, K. A. Williams, Z. Wu, A. A. Puretzky, and D. B. Geohegan, "Raman study of Fano interference in p-type doped silicon," *Journal of Raman Spectroscopy*, vol. 41, no. 12, pp. 1759–1764, 2010. [Online]. Available: http://dx.doi.org/10.1002/jrs.2614

[121] T. Kawashima, G. Imamura, T. Saitoh, K. Komori, M. Fujii, and S. Hayashi, "Raman scattering studies of electrically active impurities in in situ B-doped silicon nanowires: Effects of annealing and oxidation," *The Journal of Physical Chemistry C*,

vol. 111, no. 42, pp. 15 160–15 165, 2007. [Online]. Available: http://dx.doi.org/10.1021/jp074495r

[122] G. Imamura, T. Kawashima, M. Fujii, C. Nishimura, T. Saitoh, and S. Hayashi, "Distribution of active impurities in single silicon nanowires," *Nano Letters*, vol. 8, no. 9, pp. 2620–2624, 2008. [Online]. Available: http://dx.doi.org/10.1021/nl080265s

[123] G. S. Doerk, G. Lestari, F. Liu, C. Carraro, and R. Maboudian, "Ex situ vapor phase boron doping of silicon nanowires using BBr_3," *Nanoscale*, vol. 2, no. 7, pp. 1165–1170, 2010. [Online]. Available: http://dx.doi.org/10.1039/C0NR00127A

[124] S. R. Goodes, T. E. Jenkins, M. I. J. Beale, J. D. Benjamin, and C. Pickering, "The characterisation of porous silicon by Raman spectroscopy," *Semiconductor Science and Technology*, vol. 3, no. 5, p. 483, 1988. [Online]. Available: http://stacks.iop.org/0268-1242/3/i=5/a=011

[125] H. Münder, C. Andrzejak, M. G. Berger, U. Klemradt, H. Lüth, R. Herino, and M. Ligeon, "A detailed Raman study of porous silicon," *Thin Solid Films*, vol. 221, no. 12, pp. 27–33, 1992. [Online]. Available: http://www.sciencedirect.com/science/article/pii/0040609092907919

[126] Z. Sui, P. P. Leong, I. P. Herman, G. S. Higashi, and H. Temkin, "Raman analysis of light-emitting porous silicon," *Appllied Physics Letters*, vol. 60, no. 17, pp. 2086–2088, 1992. [Online]. Available: http://scitation.aip.org/content/aip/journal/apl/60/17/10.1063/1.107097

[127] S.-L. Zhang, Y. Hou, K.-S. Ho, B. Qian, and S. Cai, "Raman investigation with excitation of various wavelength lasers on porous silicon," *Journal of Applied Physics*, vol. 72, no. 9, pp. 4469–4471, 1992. [Online]. Available: http://dx.doi.org/10.1063/1.352178

[128] M. Yang, D. Huang, P. Hao, F. Zhang, X. Hou, and X. Wang, "Study of the Raman peak shift and the linewidth of light-emitting porous silicon," *Journal of Applied Physics*, vol. 75, no. 1, pp. 651–653, 1994. [Online]. Available: http://dx.doi.org/10.1063/1.355808

[129] M. N. Islam and S. Kumar, "Influence of crystallite size distribution on the micro-Raman analysis of porous Si," *Applied Physics Letters*, vol. 78, no. 6, pp. 715–717, 2001. [Online]. Available: http://scitation.aip.org/content/aip/journal/apl/78/6/10.1063/1.1343494

[130] R. Prabakaran, R. Kesavamoorthy, and A. Singh, "Optical and microstructural investigations of porous silicon," *Bulletin of Materials Science*, vol. 28, no. 3, pp. 219–225, 2005. [Online]. Available: http://dx.doi.org/10.1007/BF02711251

[131] G. Irmer, "Raman scattering of nanoporous semiconductors," *Journal of Raman Spectroscopy*, vol. 38, no. 6, pp. 634–646, 2007. [Online]. Available: http://dx.doi.org/10.1002/jrs.1703

[132] D. Abidi, S. Romdhane, A. Brunet-Bruneau, and J.-L. Fave, "Microstructural characterization of porous silicon for use in optoelectronic devices," *The European Physical Journal - Applied Physics*, vol. 45, no. 01, 2009. [Online]. Available: http://dx.doi.org/10.1051/epjap:2008192

[133] D. Abidi, B. Jusserand, and J.-L. Fave, "Raman scattering studies of heavily doped microcrystalline porous silicon and porous silicon free-standing membranes," *Physical Review B*, vol. 82, no. 7, p. 075210, 2010. [Online]. Available: http://link.aps.org/doi/10.1103/PhysRevB.82.075210

[134] H. Richter, Z. P. Wang, and L. Ley, "The one phonon Raman spectrum in microcrystalline silicon," *Solid State Communications*, vol. 39, no. 5, pp. 625–629, 1981. [Online]. Available: http://www.sciencedirect.com/science/article/pii/0038109881903379

[135] I. H. Campbell and P. M. Fauchet, "The effects of microcrystal size and shape on the one phonon Raman spectra of crystalline semiconductors," *Solid State Communications*, vol. 58, no. 10, pp. 739–741, 1986. [Online]. Available: http://www.sciencedirect.com/science/article/pii/0038109886905132

[136] S. Bhattacharyya and S. Samui, "Phonon confinement in oxide-coated silicon nanowires," *Applied Physics Letters*, vol. 84, no. 9, pp. 1564–1566, 2004. [Online]. Available: http://scitation.aip.org/content/aip/journal/apl/84/9/10.1063/1.1651648

[137] K. W. Adu, H. R. Gutirrez, U. J. Kim, G. U. Sumanasekera, and P. C. Eklund, "Confined phonons in Si nanowires," *Nano Letters*, vol. 5, no. 3, pp. 409–414, 2005. [Online]. Available: http://dx.doi.org/10.1021/nl0486259http://pubs.acs.org/doi/pdfplus/10.1021/nl0486259

[138] K. W. Adu, H. R. Gutirrez, U. J. Kim, and P. C. Eklund, "Inhomogeneous laser heating and phonon confinement in silicon nanowires: A micro-Raman scattering study," *Physical Review B*, vol. 73, no. 15, p. 155333, 2006. [Online]. Available: http://link.aps.org/doi/10.1103/PhysRevB.73.155333

[139] S. Piscanec, M. Cantoro, A. C. Ferrari, J. A. Zapien, Y. Lifshitz, S. T. Lee, S. Hofmann, and J. Robertson, "Raman spectroscopy of silicon nanowires," *Physical Review B*, vol. 68, no. 24, p. 241312, 2003. [Online]. Available: http://link.aps.org/doi/10.1103/PhysRevB.68.241312

[140] R. Gupta, Q. Xiong, C. K. Adu, U. J. Kim, and P. C. Eklund, "Laser-induced Fano resonance scattering in silicon nanowires," *Nano Letters*, vol. 3, no. 5, pp. 627–631, 2003. [Online]. Available: http://dx.doi.org/10.1021/nl0341133

[141] G. S. Doerk, C. Carraro, and R. Maboudian, "Temperature dependence of Raman spectra for individual silicon nanowires," *Physical Review B*, vol. 80, no. 7, p. 073306, 2009. [Online]. Available: http://link.aps.org/doi/10.1103/PhysRevB.80.073306

[142] J. Anaya, A. Torres, V. Hortelano, J. Jimnez, A. C. Prieto, A. Rodríguez, T. Rodríguez, R. Rogel, and L. Pichon, "Raman spectrum of Si nanowires: temperature and phonon confinement effects," *Applied Physics A*, vol. 114, no. 4, pp. 1321–1331, 2014. [Online]. Available: http://dx.doi.org/10.1007/s00339-013-7966-y

[143] M. Ivanda and K. Furi, "Line focusing in micro-Raman spectroscopy," *Applied Optics*, vol. 31, no. 30, pp. 6371–6375, 1992. [Online]. Available: http://ao.osa.org/abstract.cfm?URI=ao-31-30-6371

[144] J. Menéndez and M. Cardona, "Temperature dependence of the first-order Raman scattering by phonons in Si, Ge, and α-Sn: Anharmonic effects," *Physical Review B*, vol. 29, no. 4, pp. 2051–2059, 1984. [Online]. Available: http://link.aps.org/doi/10.1103/PhysRevB.29.2051

[145] D. Posener, "The shape of spectral lines: Tables of the Voigt profile," *Australian Journal of Physics*, vol. 12, no. 2, pp. 184–196, 1959. [Online]. Available: http://www.publish.csiro.au/paper/PH590184

[146] S. Schippers, "Analytical expression for the convolution of a Fano line profile with a Gaussian," *International Review of Atomic and Molecular Physics*, p. 4, 2011.

[147] N. H. Nickel, P. Lengsfeld, and I. Sieber, "Raman spectroscopy of heavily doped polycrystalline silicon thin films," *Physical Review B*, vol. 61, no. 23, pp. 15 558–15 561, 2000. [Online]. Available: http://link.aps.org/doi/10.1103/PhysRevB.61.15558

[148] H. H. Burke and I. P. Herman, "Temperature dependence of Raman scattering in $Ge_{1-x}Si_x$ alloys," *Physical Review B*, vol. 48, no. 20, pp. 15 016–15 024, 1993. [Online]. Available: http://link.aps.org/doi/10.1103/PhysRevB.48.15016

[149] E. Anastassakis, A. Pinczuk, E. Burstein, F. H. Pollak, and M. Cardona, "Effect of static uniaxial stress on the Raman spectrum of silicon," *Solid State Communications*, vol. 88, no. 1112, pp. 1053–1058, 1993. [Online]. Available: http://www.sciencedirect.com/science/article/pii/003810989390294W

[150] W. Ingrid De, "Micro-Raman spectroscopy to study local mechanical stress in silicon integrated circuits," *Semiconductor Science and Technology*, vol. 11, no. 2, p. 139, 1996. [Online]. Available: http://stacks.iop.org/0268-1242/11/i=2/a=001

[151] R. Tubino, L. Piseri, and G. Zerbi, "Lattice dynamics and spectroscopic properties by a valence force potential of diamondlike crystals: C, Si, Ge, and Sn," *The Journal of Chemical Physics*, vol. 56, no. 3, pp. 1022–1039, 1972.

[152] G. Nilsson and G. Nelin, "Study of the homology between silicon and germanium by thermal-neutron spectrometry," *Physical Review B*, vol. 6, no. 10, pp. 3777–3786, 1972. [Online]. Available: http://link.aps.org/doi/10.1103/PhysRevB.6.3777

[153] R. Kumar and A. K. Shukla, "Quantum interference in the Raman scattering from the silicon nanostructures," *Physics Letters A*, vol. 373, no. 32, pp. 2882–2886, 2009. [Online]. Available: http://www.sciencedirect.com/science/article/pii/S0375960109006872

[154] S. Mirabella, D. De Salvador, E. Napolitani, E. Bruno, and F. Priolo, "Mechanisms of boron diffusion in silicon and germanium," *Journal of Applied Physics*, vol. 113, no. 3, p. 031101, 2013. [Online]. Available: http://dx.doi.org/10.1063/1.4763353

[155] Y. A. Pusep, A. D. Rodrigues, L. J. Borrero-Gonzlez, L. N. Acquaroli, R. Urteaga, R. D. Arce, R. R. Koropecki, M. Tirado, and D. Comedi, "Fano resonance in heavily doped porous silicon," *Journal of Raman Spectroscopy*, vol. 42, no. 6, pp. 1405–1407, 2011. [Online]. Available: http://dx.doi.org/10.1002/jrs.2870

[156] C. Herring, "Theory of the thermoelectric power of semiconductors," *Physical Review*, vol. 96, no. 5, pp. 1163–1187, 1954. [Online]. Available: http://link.aps.org/doi/10.1103/PhysRev.96.1163

[157] P. Pichanusakorn and P. Bandaru, "Nanostructured thermoelectrics," *Materials Science and Engineering: R: Reports*, vol. 67, no. 24, pp. 19–63, 2010.

[158] M. Cutler and N. F. Mott, "Observation of anderson localization in an electron gas," *Physical Review*, vol. 181, no. 3, pp. 1336–1340, 1969. [Online]. Available: http://dx.doi.org/10.1103/PhysRev.181.1336

[159] J. Heremans, "Low-dimensional thermoelectricity," *ACTA PHYSICA POLONICA SERIES A*, vol. 108, no. 4, p. 609, 2005.

[160] M. Cutler, J. F. Leavy, and R. L. Fitzpatrick, "Electronic transport in semimetallic cerium sulfide," *Physical Review*, vol.

133, no. 4A, pp. A1143–A1152, 1964. [Online]. Available: http://dx.doi.org/10.1103/PhysRev.133.A1143

[161] T. H. Geballe and G. W. Hull, "Seebeck effect in silicon," *Physical Review*, vol. 98, no. 4, p. 940, 1955. [Online]. Available: http://link.aps.org/doi/10.1103/PhysRev.98.940

[162] M. E. Brinson and W. Dunstant, "Thermal conductivity and thermoelectric power of heavily doped n-type silicon," *Journal of Physics C: Solid State Physics*, vol. 3, no. 3, p. 483, 1970. [Online]. Available: http://stacks.iop.org/0022-3719/3/i=3/a=001

[163] H. P. R. Frederikse, "Thermoelectric power of germanium below room temperature," *Physical Review*, vol. 92, no. 2, pp. 248–252, 1953. [Online]. Available: http://dx.doi.org/10.1103/PhysRev.92.248

[164] M. W. Wu, N. J. M. Horing, and H. L. Cui, "Phonon-drag effects on thermoelectric power," *Physical Review B*, vol. 54, pp. 5438–5443, Aug 1996. [Online]. Available: http://link.aps.org/doi/10.1103/PhysRevB.54.5438

[165] L. Weber and E. Gmelin, "Transport properties of silicon," *Applied Physics A: Materials Science & Processing*, vol. 53, no. 2, pp. 136–140, 1991. [Online]. Available: http://dx.doi.org/10.1007/BF00323873

[166] C. Dames and G. Chen, "Theoretical phonon thermal conductivity of Si/Ge superlattice nanowires," *Journal of Applied Physics*, vol. 95, no. 2, pp. 682–693, 2004. [Online]. Available: http://dx.doi.org/10.1063/1.1631734

[167] J. M. Ziman, "The effect of free electrons on lattice conduction," *Philosophical Magazine*, vol. 2, no. 14, pp. 292–292, 1957.

[168] C. J. Glassbrenner and G. A. Slack, "Thermal conductivity of silicon and germanium from 3 K to the melting point," *Physical Review*, vol. 134, no. 4A, pp. A1058–A1069, 1964. [Online]. Available: http://dx.doi.org/10.1103/PhysRev.134.A1058

[169] J. Callaway, "Model for lattice thermal conductivity at low temperatures," *Physical Review*, vol. 113, no. 4, pp. 1046–1051, 1959. [Online]. Available: http://link.aps.org/doi/10.1103/PhysRev.113.1046

[170] N. Mingo, "Calculation of Si nanowire thermal conductivity using complete phonon dispersion relations," *Physical Review B*, vol. 68, no. 11, p. 113308, 2003. [Online]. Available: http://link.aps.org/doi/10.1103/PhysRevB.68.113308

[171] Z. Wang, J. E. Alaniz, W. Jang, J. E. Garay, and C. Dames, "Thermal conductivity of nanocrystalline silicon: Importance of

grain size and frequency-dependent mean free paths," *Nano Letters*, vol. 11, no. 6, pp. 2206–2213, 2011. [Online]. Available: http://dx.doi.org/10.1021/nl1045395

[172] P. E. Hopkins, P. T. Rakich, R. H. Olsson, I. F. El-kady, and L. M. Phinney, "Origin of reduction in phonon thermal conductivity of microporous solids," *Applied Physics Letters*, vol. 95, no. 16, p. 161902, 2009. [Online]. Available: http://dx.doi.org/10.1063/1.3250166

[173] M. G. Holland, "Analysis of lattice thermal conductivity," *Physical Review*, vol. 132, no. 6, pp. 2461–2471, 1963. [Online]. Available: http://link.aps.org/doi/10.1103/PhysRev.132.2461

[174] M. Asheghi, K. Kurabayashi, R. Kasnavi, and K. E. Goodson, "Thermal conduction in doped single-crystal silicon films," *Journal of Applied Physics*, vol. 91, no. 8, pp. 5079–5088, 2002. [Online]. Available: http://dx.doi.org/10.1063/1.1458057

[175] J. M. Ziman, "XVII. the effect of free electrons on lattice conduction," *Philosophical Magazine*, vol. 1, no. 2, pp. 191–198, 1956.

[176] V. Kosarev, "Scattering of phonons by carriers in the field of charged impurities," *SOVIET PHYSICS JETP*, vol. 33, no. 4, 1971.

[177] R. W. Keyes, "Low-temperature thermal resistance of n-type germanium," *Physical Review*, vol. 122, no. 4, pp. 1171–1176, 1961. [Online]. Available: http://dx.doi.org/10.1103/PhysRev.122.1171

[178] D. Fortier and K. Suzuki, "Effect of P donors on thermal phonon scattering in Si," *J. Phys. France*, vol. 37, no. 2, pp. 143–147, 1976. [Online]. Available: http://dx.doi.org/10.1051/jphys:01976003702014300

[179] K. Suzuki and N. Mikoshiba, "Effects of uniaxial stress and magnetic field on the low-temperature thermal conductivity of p-type Ge and Si," *Journal of the Physical Society of Japan*, vol. 31, no. 1, pp. 44–53, 1971.

[180] R. Kim and M. Lundstrom, "Notes on Fermi-Dirac integrals (3rd edition)," *arXiv preprint arXiv:0811.0116*, 2008.

[181] S. L. Chuang, *Physics of Photonic Devices*. Wiley Publishing, 2009.

[182] W. B. Joyce and R. W. Dixon, "Analytic approximations for the Fermi energy of an ideal Fermi gas," *Applied Physics Letters*, vol. 31, no. 5, pp. 354–356, 1977. [Online]. Available: http://dx.doi.org/10.1063/1.89697

[183] P. W. Chapman, O. N. Tufte, J. D. Zook, and D. Long, "Electrical properties of heavily doped silicon," *Journal of Applied*

Physics, vol. 34, no. 11, pp. 3291–3295, 1963. [Online]. Available: http://dx.doi.org/10.1063/1.1729180

[184] J. C. Maxwell, *A Treatise on Electricity and Magnetism.* Oxford: Clarendon Press, 1873.

[185] A. Eucken, "Allgemeine gesetzmäßigkeiten für das wärmeleitvermögen verschiedener stoffarten und aggregatzustände," *Forschung auf dem Gebiet des Ingenieurwesens A*, vol. 11, no. 1, pp. 6–20, 1940.

[186] P. E. Hopkins, L. M. Phinney, P. T. Rakich, I. Olsson, R. H., and I. El-Kady, "Phonon considerations in the reduction of thermal conductivity in phononic crystals," *Applied Physics A*, vol. 103, no. 3, pp. 575–579, 2011.

[187] R. C. Progelhof, J. L. Throne, and R. R. Ruetsch, "Methods for predicting the thermal conductivity of composite systems: A review," *Polymer Engineering & Science*, vol. 16, no. 9, pp. 615–625, 1976.

[188] J. Wang, J. K. Carson, M. F. North, and D. J. Cleland, "A new approach to modelling the effective thermal conductivity of heterogeneous materials," *International Journal of Heat and Mass Transfer*, vol. 49, no. 1718, pp. 3075–3083, 2006.

[189] R. H. Tarkhanyan and D. G. Niarchos, "Reduction in lattice thermal conductivity of porous materials due to inhomogeneous porosity," *International Journal of Thermal Sciences*, vol. 67, pp. 107–112, 2013. [Online]. Available: http://www.sciencedirect.com/science/article/pii/S1290072912003389

[190] L.-C. Liu and M.-J. Huang, "Thermal conductivity modeling of micro- and nanoporous silicon," *International Journal of Thermal Sciences*, vol. 49, no. 9, pp. 1547–1554, 2010.

[191] P. G. Klemens, *Thermal Conductivity and Lattice Vibrational Modes.* Academic Press, 1958, vol. Volume 7, pp. 1–98.

[192] D. G. Cahill, S. K. Watson, and R. O. Pohl, "Lower limit to the thermal conductivity of disordered crystals," *Physical Review B*, vol. 46, no. 10, pp. 6131–6140, 1992. [Online]. Available: http://link.aps.org/doi/10.1103/PhysRevB.46.6131

[193] C. L. Pekeris, "Note on the scattering of radiation in an inhomogeneous medium," *Physical Review*, vol. 71, no. 4, pp. 268–269, 1947. [Online]. Available: http://dx.doi.org/10.1103/PhysRev.71.268

[194] J. A. Fejer, "The diffraction of waves in passing through an irregular refracting medium," *Proceedings of the Royal Society of London A: Mathematical, Physical and Engineering Sciences*, vol. 220, no. 1143, pp. 455–471, 1953.

[195] B. J. Uscinski, "The multiple scattering of waves in irregular media," *Philosophical Transactions of the Royal Society of London. Series A, Mathematical and Physical Sciences*, vol. 262, no. 1133, pp. 609–640, 1968.

[196] L. Knopoff and J. A. Hudson, "Frequency dependence of amplitudes of scattered elastic waves," *The Journal of the Acoustical Society of America*, vol. 42, no. 1, pp. 18–20, 1967.